

ISSN 1590-8844
Vol. 11 No 01
2010

International Journal of Mechanics and Control

Editor: **Andrea Manuello Bertetto**



LIBRERIA EDITRICE UNIVERSITARIA
LEVROTTO & BELLA
TORINO

Editorial Board of the
International Journal of Mechanics and Control

Published by Levrotto&Bella – Torino – Italy E.C.

Honorary editors

Guido Belforte

Kazy Yamafuji

Editor: Andrea Manuello Bertetto

General Secretariat: Elvio Bonisoli

Atlas Akhmetzyanov
*V.A.Trapeznikov Institute of Control Sciences
of Russian Academy of Sciences
Moscow – Russia*

Domenico Appendino
*Prima Industrie
Torino – Italy*

Kenji Araki
*Saitama University
Shimo Okubo, Urawa
Saitama – Japan*

Guido Belforte
*Technical University – Politecnico di Torino
Torino – Italy*

Bruno A. Boley
*Columbia University,
New York – USA*

Marco Ceccarelli
*LARM at DIMSAT
University of Cassino
Cassino – Italy*

Amalia Ercoli Finzi
*Technical University – Politecnico di Milano
Milano – Italy*

Carlo Ferraresi
*Technical University – Politecnico di Torino
Torino – Italy*

Anindya Ghoshal
*Arizona State University
Tempe – Arizona – USA*

Nunziatino Gualtieri
*Space System Group
Alenia Spazio
Torino – Italy*

Alexandre Ivanov
*Technical University – Politecnico di Torino
Torino – Italy*

Giovanni Jacazio
*Technical University – Politecnico di Torino
Torino – Italy*

Takashi Kawamura
*Shinshu University
Nagano – Japan*

Kin Huat Low
*School of Mechanical and Aerospace Engineering
Nanyang Technological University
Singapore*

Andrea Manuello Bertetto
*University of Cagliari
Cagliari – Italy*

Stamos Papastergiou
*Jet Joint Undertaking
Abingdon – United Kingdom*

Mihailo Ristic
*Imperial College
London – United Kingdom*

János Somló
*Technical University of Budapest
Budapest – Hungary*

Jozef Suchy
*Faculty of Natural Science
Banska Bystrica – Slovakia*

Federico Thomas
*Instituto de Robótica e Informática Industrial
(CSIC-UPC)
Barcelona – Espana*

Lubomir Uher
*Institute of Control Theory and Robotics
Bratislava – Slovakia*

Furio Vatta
*Technical University – Politecnico di Torino
Torino – Italy*

Vladimir Viktorov
*Technical University – Politecnico di Torino
Torino – Italy*

Kazy Yamafuji
*University of Electro-Communications
Tokyo – Japan*

*Official Torino Italy Court Registration
n.5390, 5th May 2000*

*Deposito presso il Tribunale di Torino
numero 5390 del 5 maggio 2000*

Direttore responsabile:

Andrea Manuello Bertetto

International Journal of Mechanics and Control

Editor: Andrea Manuello Bertetto

***Honorary editors: Guido Belforte
Kazy Yamafuji***

General Secretariat: Elvio Bonisoli

The Journal is addressed to scientists and engineers who work in the fields of mechanics (mechanics, machines, systems, control, structures). It is edited in Turin (Northern Italy) by Levrotto&Bella Co., with an international board of editors. It will have not advertising.

Turin has a great and long tradition in mechanics and automation of mechanical systems. The journal would will to satisfy the needs of young research workers of having their work published on a qualified paper in a short time, and of the public need to read the results of researches as fast as possible.

Interested parties will be University Departments, Private or Public Research Centres, Innovative Industries.

Aims and scope

The *International Journal of Mechanics and Control* publishes as rapidly as possible manuscripts of high standards. It aims at providing a fast means of exchange of ideas among workers in Mechanics, at offering an effective method of bringing new results quickly to the public and at establishing an informal vehicle for the discussion of ideas that may still in the formative stages.

Language: English

International Journal of Mechanics and Control will publish both scientific and applied contributions. The scope of the journal includes theoretical and computational methods, their applications and experimental procedures used to validate the theoretical foundations. The research reported in the journal will address the issues of new formulations, solution, algorithms, computational efficiency, analytical and computational kinematics synthesis, system dynamics, structures, flexibility effects, control, optimisation, real-time simulation, reliability and durability. Fields such as vehicle dynamics, aerospace technology, robotics and mechatronics, machine dynamics, crashworthiness, biomechanics, computer graphics, or system identification are also covered by the journal.

Please address contributions to

Prof. Guido Belforte
Prof. Andrea Manuello Bertetto
PhD Eng. Elvio Bonisoli

*Dept. of Mechanics
Technical University - Politecnico di Torino
C.so Duca degli Abruzzi, 24.
10129 - Torino - Italy - E.C.*

www.jomac.it
e_mail: jomac@polito.it

Subscription information

Subscription order must be sent to the publisher:

*Libreria Editrice Universitaria
Levrotto&Bella
2/E via Pigafetta – 10129 Torino – Italy*

www.levrotto-bella.net
e_mail: info@levrotto-bella.net
tel. +39.011.5097367
+39.011.5083690
fax +39.011.504025

Preface for the special issue of the JoMaC dedicated to the 18th edition of the Workshop on Robotics in Alpe-Adria-Danube Region, RAAD 2009

Following the tradition of previous RAAD scientific events, the 18th edition of the RAAD'09 workshop gathered researchers of the robotics community from countries of the Alpe-Adria-Danube region, in a collegial and creative environment. Coherently with its tradition, RAAD'09 covered all the major areas of robotics research and applications, from fundamental to applied research, implementing of robotized solutions in industry and services, development of new design solutions and prototypes for mechatronics, and integration of cooperating robots in distributed, multi-agent process control architectures.

The workshop made possible a panel of significant scientific and technical discussions pointing at the most recent developments in the field of robotics, renewed professional contacts and strengthened the participants' technical expertise. Social and cultural events were also planned to facilitate exchanges of ideas, opinions and experience between the attendees.

The 18th edition of the RAAD workshop was organized by the Centre of Research and Training in Robotics and Computer Integrated Manufacturing – CIMR of the University Politehnica of Bucharest in partnership with the University "Transilvania" in Braşov during May 25-27, 2009 in the AULA Conference Centre. The event was sponsored by IFToMM, the Romanian Society of Robotics, and the National Authority of Scientific Research. Well-known national IT, automation and manufacturing companies acted as workshop sponsors: IBM Romania, East Electric (representing Adept Technology and Bosch-Rexroth), ABB Romania, SMC Romania, FESTO Romania, KUKA Romania, ROBCON, ASTI and iRobot Romania.

During the three days of technical sessions, the AULA Conference Centre in Brasov also hosted the Exhibition: "Innovation in Robotics, Control and Software Technologies for Enterprise and Open Education", where companies present their products and applications in robotics, automation and manufacturing, and software technologies for the manufacturing, service and education industries. The round table "Co@OpERA" – An European Collaborative Platform for Open Education in Robotics and its Applications in Manufacturing and Services was planned to foster cooperation between industry and academia in robotics in the international frame of the RAAD Scientific Organization.

The Technical Program Committee has defined an outstanding program in quality and diversity. A number of 96 papers have been finally selected from 115 received, after a careful revision process involving 32 reviewers. The papers, involving authors from 14 countries have been presented in four plenary sessions and eighteen technical sessions. The session topics reflected the trends in analysis, modelling, design and integration of robot systems in various fields of activity and applications: manufacturing, services, health care, surgery and human rehabilitation, education and collaborative projects, space investigation, tele-operation and web-based control, grasping, guidance vision, automated visual inspection and data fusion.

Heading 170 km north from Bucharest along the Prahova Valley, the city of Brasov is located at the feet of the Bucegi and Postăvaru mountains, close to Poiana Brasov – a famous winter sports station, Bran – hosting the Dracula castle, and Râşnov – dominated by its fortified settlement on the hill. Once an important medieval trading centre, Brasov is the third-largest city in Romania. Braşov's best sights can be found in the centre of the city. Piata Sfatului, a large cobblestone square at the heart of the old Germanic town, is still surrounded in places by the original fortress walls; its buildings recalling the region's German heritage. Built in the 15th century, the Black Church in Brasov is a Gothic masterpiece where organ concerts are daily performed.

We believe that RAAD'09, hosted by Brasov, represented an important moment for the activity of our RAAD Organization in sustaining innovative R&D projects of the robotics science and technology.



Theodor Borangiu, Coordinator of RAAD International Scientific Committee

A handwritten signature in black ink, appearing to read 'Borangiu'.

COMPARATIVE ANALYSIS OF ISOTROPY INDICES IN RR AND RRP ARMS

Nicola Pio Belfiore Matteo Verotti Luciano Consorti

Department of Mechanics and Aeronautics, *Sapienza* University of Rome, Italy

ABSTRACT

In this paper isotropy and manipulability in RR dyads and RRP arms are analyzed and the solutions are obtained in algebraic symbolic forms. Such analysis is performed by means of two different methods: the classical approach based on the condition number and the Lie product. Although both the methods are known since decades, an accurate comparison of the two approaches has never been presented in literature. In particular, the geometrical interpretation of the Lie Product allows to appreciate some interesting differences between the two methods.

Keywords: Isotropy, Manipulability, SCARA, Condition Number, Lie Product.

1 INTRODUCTION

Manipulability and isotropy indices have been widely studied in robotics.

Earl attempts to find a performance kinematic index were the concepts of *service angle* [1] and of *conditioning* [2]. Then, the concepts of *manipulability* and *dextrous workspace* were introduced by [3-5]. However, the determinant of the manipulator Jacobian, used by [6], and the determinant of the product of the latter by its transpose did not give an absolute value to quantify the invertibility of the Jacobian itself, as pointed out by [7]. Thus the concept of *condition number* of the Jacobian was used by [8] and then by [9] and [10].

In linear algebra the condition number of a square matrix, associated with a linear system of equations, is a measure of the relative roundoff error amplification of the computed results with respect to the relative roundoff error of the data [7]. In [11] the kinematic performance is related to the minimum singular value of the Jacobian, as a measure of the distance to singularities. Further, based on the condition number of the Jacobian, the *kinematic conditioning index* could be defined as in [10]. Other formulations and various aspects of open chain manipulability have been also investigated by [12-15]. Nearly all of the previous contributions are based on parameterizations of the forward kinematics in local coordinates.

In [16] and [17] some manipulability measures have been formulated under a general mathematical framework, by using the coordinate free methods of Riemann's geometry.

Moreover, a great number of cost functions (to characterize the kinematic performances of the manipulator) have been presented in literature. In [18] a cost function to describe kinematic isotropy, manipulability and accuracy has been proposed. In order to remove the configuration dependence from these measures, a new global isotropy index, introduced in [19-20], could compare worst-case values of the workspace as a whole.

Quite recently, an approach based on the Lie Product has been introduced in order to get more information about the workspace. This new approach gave some promising results. However, it has been difficult, until now, to understand the differences between the method based on the Lie Product and the classical method based on the condition number of the Jacobian matrix.

In this paper, the two above mentioned methods are applied to the simple cases of RR dyad and RRP arm. Analytical closed form solutions are obtained for both the methods and a reasoned comparison of the results is presented.

2 THE APPROACH BASED ON THE LIE PRODUCT

The idea of using the Lie product in order to detect isotropy is not new. Basically, it consists in detecting the isotropy conditions by using a static condition, namely, that *isotropy is reached when the applied force (or generalized force wrench vector) is parallel to the consequent displacement (or generalized displacement twist vector)*. By applying the *GSLT (General System Logical Theory)* and the Lie product to the compliance matrix it is possible to estimate how far or near to the isotropy condition a given pose is.

Contact author: Nicola Pio Belfiore,
belfiore@dma.ing.uniroma1.it
Dept. Mechanics and Aeronautics, via Eudossiana, 18,
00184 Rome, Italy

2.1 THEORETICAL BACKGROUND

As described in [21] and [22], the *GSLT* is based on the *ELS(n) Elementary Logical System* at the *n* level. At the level 0, the *ELS(0)* is represented by a generic operator *OP* which transforms an input set X_1 into an output set Y_1 , according to the following scheme:

$$X_1 \rightarrow \boxed{OP} \rightarrow Y_1 \quad (1)$$

At the level 1, the *ELS(1)* concerns a generic operator E_1 that is applied on the element X_1 and transforms it into an element X_2 that belongs to the same space. Both X_1 and X_2 can be transformed by the operator *OP* into their corresponding elements Y_1 and Y_2 , as in the following scheme;

$$\begin{array}{ccc} X_1 & \rightarrow & \boxed{OP} & \rightarrow & Y_1 \\ | & & & & | \\ E_1 & & & & E_2 \\ \downarrow & & & & \downarrow \\ X_2 & \rightarrow & \boxed{OP} & \rightarrow & Y_2 \end{array} \quad (2)$$

which represents the relation between the set of transformations between two different spaces. The *ELS(1)* consists in the study of transformations of transformations. For this purpose, the difference space *DS* is introduced as

$$DS = (OP E_1 - E_1 OP) X_1 = [OP, E_1] X_1, \quad (3)$$

where $[OP, E_1]$ is the Lie product of the operators E_1 and *OP*. Such product, which can be also expressed as

$$LP(X_1) = Y_2 - E_1(Y_1), \quad (4)$$

represents the difference between Y_2 and the value that is obtained by applying the operator E_1 to Y_1 (in place of E_2).

2.2 REVIEW OF THE MAIN CONCEPTS IN ROBOT STATICS

Any possible external load $\{F_s\}$, defined as in (57) (see Appendix), which is applied to the end effector, can be reduced to a force $\{f\}$ (applied to the origin of the end effector reference frame) and a torque $\{c\}$ (parallel to the vector force).

The application of a load $\{F_s\}$ to the end effector has the effect of moving it, according to the law (see also (56))

$$\{s\} = [C] \{F_s\} \quad (5)$$

where the compliance matrix $[C]$ appears.

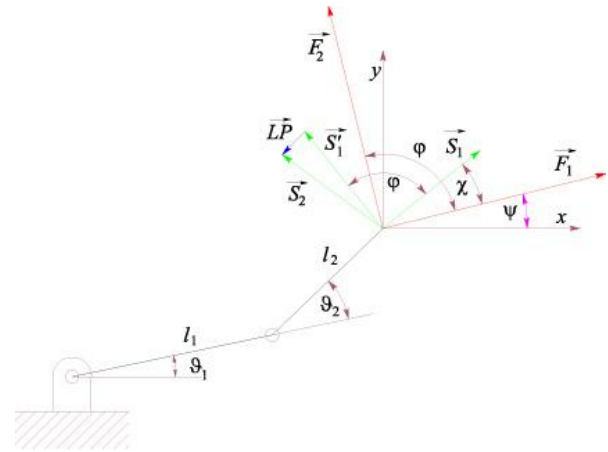


Figure 1 Representation of the Lie Product as a displacement vector in the plane.

2.3 THE APPLICATION OF THE LIE PRODUCT TO ISOTROPY CHARACTERIZATION

By applying the *ELS(0)* of the *GSLT*, the relation (5) can be represented by using the terminology adopted in (1). Hence, matrix $[C]$ plays the role of the operator that transforms the input value F_{s1} into the output $s1$:

$$F_{s1} \rightarrow \boxed{[C]} \rightarrow s1. \quad (6)$$

Skipping to the higher level *ELS(1)*, relation (2) can be invoked, where a new operator transforms F_{s1} into another element F_{s2} of the same space (in our case, the space of generalized forces):

$$\begin{array}{ccc} F_{s1} & \rightarrow & \boxed{[C]} & \rightarrow & s1 \\ | & & & & | \\ R & & & & E2 \\ \downarrow & & & & \downarrow \\ F_{s2} & \rightarrow & \boxed{[C]} & \rightarrow & s2 \end{array} \quad (7)$$

where the adopted operator is a rotation matrix $[R]$. The application of the rotated force $\{F_{s2}\}$ to the system causes a new displacement $\{s2\}$, the Lie product being, from (4),

$$\{LP\} = \{s2\} - [R]\{s1\}. \quad (8)$$

According to the scheme (7), we obtain

$$\{LP\} = ([C][R] - [R][C]) \{F_{s1}\}. \quad (9)$$

Considering the simple RR manipulator, a geometrical interpretation of the LP is given in Figure 1. The force \vec{F}_1 , applied to the tip of the second link, moves the tip along the direction of \vec{S}_1 . If force \vec{F}_1 is rotated by a given angle, say

$\varphi = \frac{\pi}{2}$, a new force \vec{F}_2 is obtained, which moves the arm tip along the direction \vec{S}_2 . If vector \vec{S}_2 is rotated by the same angle φ , the new displacement vector \vec{S}'_1 is obtained and the Lie Product is represented by that difference vector $\vec{S}_2 - \vec{S}'_1$.

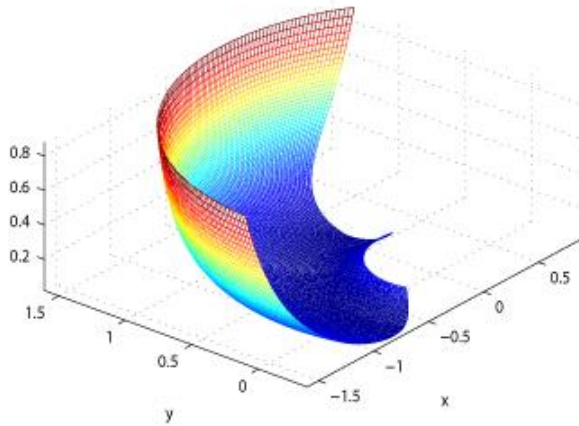


Figure 2 Isotropy index (scaled) in different configurations of the workspace for the case $l_2 = \frac{\sqrt{2}}{2}$.

3 CLOSED FORM SOLUTIONS OF THE RR DYAD KINEMATIC ANALYSIS

3.1 THE CLASSICAL METHOD BASED ON THE EIGENVALUES

By imposing that the applied force $\{F\}$ be parallel to the consequent displacement s , a classical eigenvalue problem appears as

$$([C] - \lambda[I])\{F\} = \{0\} \quad (10)$$

In the simple case of an RR dyad, by using the simplified notation

$$\begin{cases} \sin \alpha_i = s_i ; & \sin(\alpha_i + \alpha_j) = s_{ij} \\ \cos \alpha_i = c_i ; & \cos(\alpha_i + \alpha_j) = c_{ij} \end{cases}$$

the Jacobian matrix can be expressed as

$$[J] = \begin{bmatrix} -l_1 s_1 - l_2 s_{12} & -l_2 s_{12} \\ l_1 c_1 + l_2 c_{12} & l_2 c_{12} \end{bmatrix} \quad (11)$$

Assuming the stiffness matrix in the joint space as the generic matrix

$$[K_Q] = \begin{bmatrix} k_1 & 0 \\ 0 & k_2 \end{bmatrix} \quad (12)$$

equation (69) allows to express easily the compliance matrix $[C]$.

Assuming, without loss of generality

$$\vartheta_1 = 0 \quad (13)$$

and the following conditions

$$l_1 = 1, \quad (14)$$

$$k_1 = k_2 = 1, \quad (15)$$

the isotropy index, evaluated as in (79), is equal to

$$I_{iso} = \frac{1 + 2l_2^2 + 2l_2 c_2 + \sqrt{a}}{1 + 2l_2^2 + 2l_2 c_2 - \sqrt{a}} \quad (16)$$

where

$$a = 8l_2^2 c_2^2 + 1 + 4l_2 c_2 + 8l_2^3 c_2 + 4l_2^4 \quad (17)$$

In case of isotropic configuration, the eigenvalues of $[C]$ are the same, and the index reaches the minimum unit value. The equation

$$I_{iso} - 1 = 0 \quad (18)$$

can be solved with respect to $\cos \vartheta_2$ and the solutions

$$\cos \vartheta_2 = \frac{-2l_2^2 - 1 - i(1 - 2l_2^2)}{4l_2} \quad (19)$$

$$\cos \vartheta_2 = \frac{-2l_2^2 - 1 + i(1 - 2l_2^2)}{4l_2} \quad (20)$$

are obtained. By imposing that the solutions must be real, the condition

$$\frac{l_2^2}{2} - \frac{1}{4} = 0 \quad (21)$$

generates the solutions

$$l_2 = \frac{\sqrt{2}}{2}, \quad (22)$$

$$l_2 = -\frac{\sqrt{2}}{2}. \quad (23)$$

Taking the positive one, given the (19) or the (20), the angle ϑ_2 can be evaluated, since

$$\cos \vartheta_2 = -\frac{\sqrt{2}}{2}. \quad (24)$$

Figure 2 depicts the isotropy index values in dependence on the manipulator configurations, for the case $l_2 = \frac{\sqrt{2}}{2}$.

Figure 3 shows the same dependence upon the three cases cases $l_2 = \frac{\sqrt{2}}{2}$, $l_2 = 0.35$, $l_2 = 0.25$. It is evident that for the second and third cases, the isotropy index never reaches the optimum unit value.

For the case $l_2 = \frac{\sqrt{2}}{2}$, Figure 4 shows the manipulator in four different configurations, together with the corresponding manipulability ellipses. One of them becomes a simple circle when $\theta_2 = \frac{3\pi}{4}$, namely, in the isotropic condition. For the case $l_2 = \frac{1}{2}$ there are no isotropic configurations (see for example Figure 5).

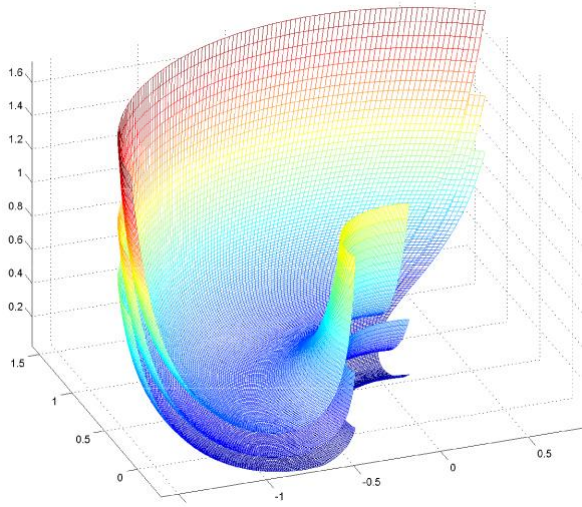


Figure 3 Isotropy index (scaled) in different configurations of the workspace for the cases: $l_2 = \frac{\sqrt{2}}{2}$, $l_2 = 0.35$, $l_3 = 0.25$.

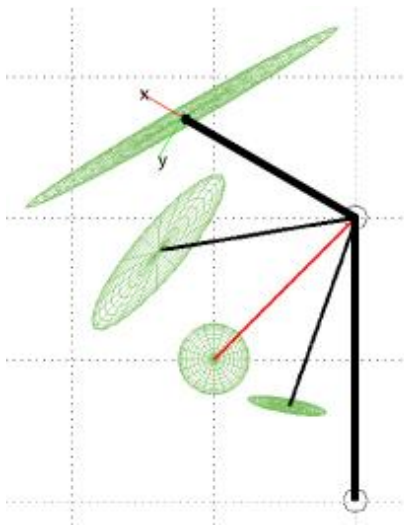


Figure 4 Force manipulability ellipses in four different configurations (the red one is isotropic).

3.2 THE APPLICATION OF THE LIE PRODUCT

The Lie product depends on the selected operator. In the present case, the rotation matrix [R] and the applied force {F} have to be defined.

In the planar case, the rotation only depends on one single angle φ , and so the rotation operator is:

$$[R] = \begin{bmatrix} \cos \varphi & -\sin \varphi \\ \sin \varphi & \cos \varphi \end{bmatrix} \quad (25)$$

while the force is assumed, with no matter about generality, as a unit vector force with a tilt angle ξ with respect to the x axis

$$\{F_s\} = \begin{Bmatrix} \cos \xi \\ \sin \xi \end{Bmatrix} \quad (26)$$

Assuming

$$a = \frac{k_2 l_1 (l_1 s_1 c_1 + l_2 a_1) + l_2^2 s_{12} c_{12} k_{12}}{k_1 k_2}$$

$$b = \frac{k_2 l_1^2 (2c_1^2 - 1) + l_2^2 k_{12} (2c_{12}^2 - 1) + 2k_2 l_1 l_2 b_1}{k_1 k_2}$$

$$a_1 = s_1 c_{12} + s_{12} c_1$$

$$b_1 = c_1 c_{12} - s_1 s_{12}$$

$$k_{12} = k_1 + k_2$$

the difference matrix has the simple form

$$[D] = [C][R] - [R][C] = \begin{bmatrix} -2as_\varphi & bs_\varphi \\ bs_\varphi & 2as_\varphi \end{bmatrix} \quad (27)$$

Since a null value of the Lie Product implies that the force vector and its corresponding displacement vector must form always the same angle (χ in Figure 1), the null value is the only one possible ($\chi = 0$). Otherwise, there would never be any isotropic direction, which is generally false from the above mentioned eigenvalue problem.

However this also implies that when the Lie Product is null, then the forces are always parallel to their corresponding displacements, that is, the configuration is isotropic.

Hence, the condition

$$\{LP\} = [D]\{F_s\} = ([C][R] - [R][C])\{F_s\} = 0 \quad (28)$$

with $\{F_s\} \neq 0$, leads to the conditions:

$$a = 0 \quad (29)$$

$$b = 0 \quad (30)$$

With no loss of generality, assuming $\vartheta_1 = 0$, we obtain

$$k_2 l_1 + l_2 c_2 (k_1 + k_2) = 0 \quad (31)$$

$$k_2 l_1^2 + l_2^2 (k_1 + k_2) (2c_2^2 - 1) + 2k_2 l_1 l_2 b_1 = 0 \quad (32)$$

Form the conditions

$$k_1 = k_2$$

$$l_1 = 1$$

the solution

$$\cos \vartheta_2 = -\frac{\sqrt{2}}{2}$$

$$l_2 = \frac{\sqrt{2}}{2}$$

can be easily found (see Appendix 7.2).

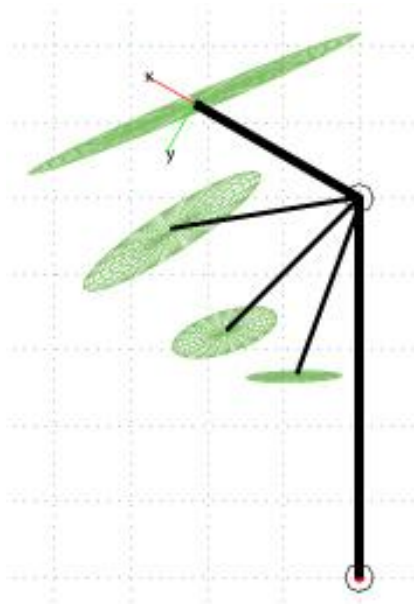


Figure 5 Force manipulability ellipses in four different configurations.

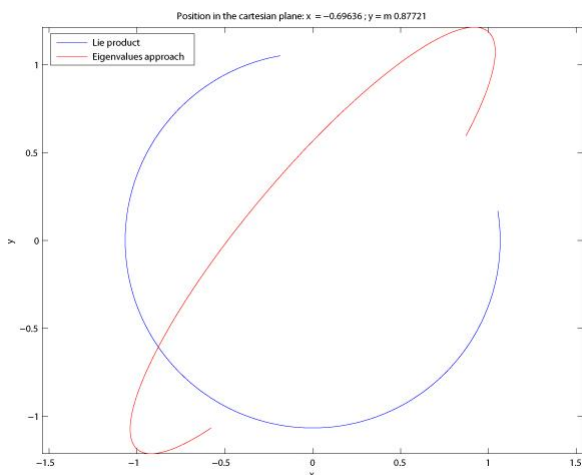


Figure 6 Polar representation of the Lie Product and the vector displacement for a range equal to 270°.

(33) 3.3 FURTHER RESULTS FOR THE RR DYAD

(34)

From (27) it is evident that the term $\sin \varphi$ appears as a factor in any element of the difference matrix. This means that when a null angle is used as operator, no effect on the relations between forces and displacements can be appreciated by using the $ELS(I)$. The maximum effect can be studied when the rotation operator is constantly equal to $\frac{\pi}{2}$.

(35)

(36)

Another interesting result consists in the fact that *the module of the Lie Product vector is a constant in RR dyads*. In fact, while the elements of \overline{LP} depend on the angle ψ by which the force is positioned, its module (under the assumed conditions)

$$\sqrt{1 + 8l_2^2 c_2^2 + 4l_2^4 + 4l_2 c_2 + 8l_2^3 c_2} \quad (37)$$

presents no such a dependency. This feature is evident in Figure 6, where the circular curve represents the arrow end of the Lie Product vector applied in the origin, while the other is the manipulability ellipse obtained by the eigenvalues approach, for an angle of revolution of the initial force equal to $\frac{3\pi}{4}$.

Figures 7, 8, and 9 offer a comparison of the polar representations of the Lie Product, the displacements, and the manipulability ellipse.

Finally, the geometrical interpretation reported in Figure 1 is numerically exemplified in Figure 10. Figure 11 reports, for the same case, more positions of the initial force.

4 ANALYSIS OF THE RRP MANIPULATOR

4.1 THE CLASSICAL EIGENVALUE METHOD

For an RRP arm, the Jacobian matrix is generally equal to

$$[J] = \begin{bmatrix} -l_1 s_1 - l_2 s_{12} & -l_2 s_{12} & 0 \\ l_1 c_1 + l_2 c_{12} & l_2 c_{12} & 0 \\ 0 & 0 & -1 \end{bmatrix} \quad (38)$$

Hence, from the joint stiffness matrix

$$[K_Q] = \begin{bmatrix} k_1 & 0 & 0 \\ 0 & k_2 & 0 \\ 0 & 0 & k_3 \end{bmatrix} \quad (39)$$

equation (69) allows the determination of the compliance matrix $[C]$.

Since

$$\vartheta_1 = 0 \quad (40)$$

$$l_1 = 1 \quad (41)$$

$$k_1 = k_2 = k, \quad (42)$$

the eigenvalues of $[C]$ are

$$\lambda_1 = \frac{1}{k_3} \quad (43)$$

$$\lambda_2 = \frac{a+b}{c} \quad (44)$$

$$\lambda_3 = \frac{a-b}{c} \quad (45)$$

where

$$a = k(2l_2c_2 + 2l_2^2 + 1)$$

$$b = k\sqrt{4l_2^2(1 + l_2^2 + c_2^2 + 2l_2c_2 - s_2^2) + 1 + 4l_2c_2}$$

$$c = 2k^2$$

Using the isotropic condition

$$\lambda_1 = \lambda_2 = \lambda_3 \quad (46)$$

the second relation

$$\lambda_2 = \lambda_3 \quad (47)$$

can be solved and real solutions can be found, provided that the relations (22) and (24), or the (35) and (36), are satisfied. In this case:

$$\lambda_2 = \lambda_3 = \frac{1}{2k} \quad (48)$$

Since

$$\lambda_1 = \lambda_3 \quad (49)$$

and l_1 has a unit value, we obtain that *the linear stiffness must be numerically equal to the double of the two torsional stiffness's*

$$k_3 = 2k \quad (50)$$

Some examples of force manipulability ellipsoids are reported in the Figures 12, 13, 14, and 15. The latter two refer to the case of isotropy.

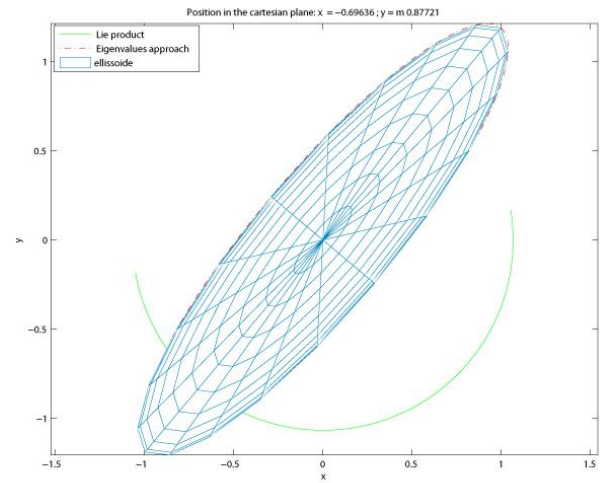


Figure 7 Polar representations of the LP, the displacements, and the force manipulability ellipsoide.

4.2 THE APPLICATION OF THE LIE PRODUCT

The application of the Lie Product leads to results that are similar to the bi-dimensional case. However, the property that *the module of the Lie product is constant* (see Figure 16) is lost. Generally, the Lie Product vector will no more describe the force manipulability ellipsoid.

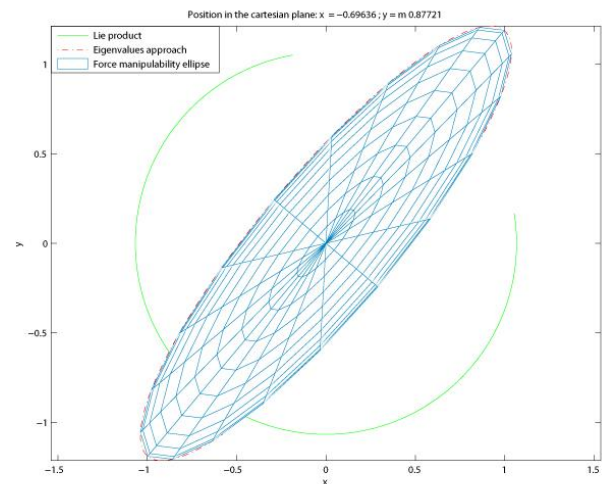


Figure 8 Polar representations of the LP, the displacements, and the force manipulability ellipsoide.

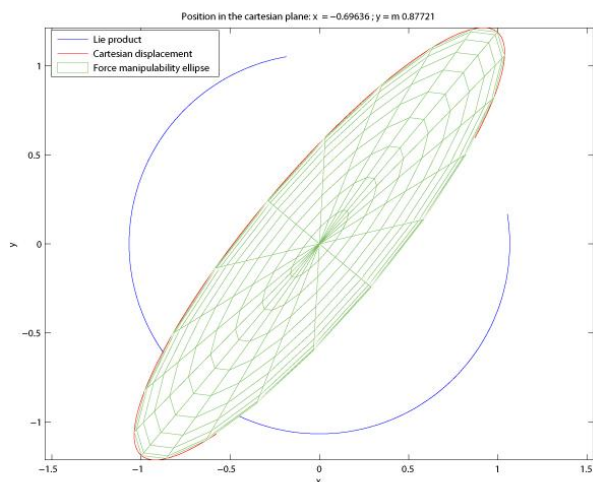


Figure 9 Polar representations of the LP, the displacements, and the force manipulability ellipse.

5 CONCLUSIONS

In this paper some differences between the method based on the eigenvalue problem and the one based on the Lie Product have been analyzed. In the planar case of a simple RR dyad, the two methods give results that are practically coincident, and show the same aptitude to measure isotropy. Their geometrical interpretation, however, is quite different. In a slightly more difficult case, such as the RRP arm, the two methods differ more. In particular, the force manipulability ellipsoid is conceptually different from the one that is obtained from the polar representation of the surface that represents the Lie Product.

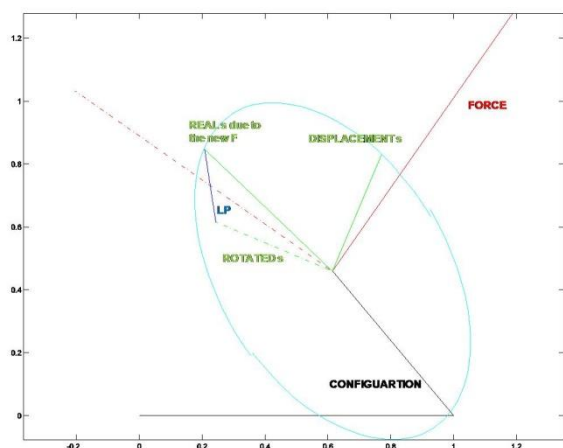


Figure 10 Force (red), displacement (green) and LP (blue) at the configuration represented (black) when the angle force is equal to 55° (solid) and 145° (dashed).

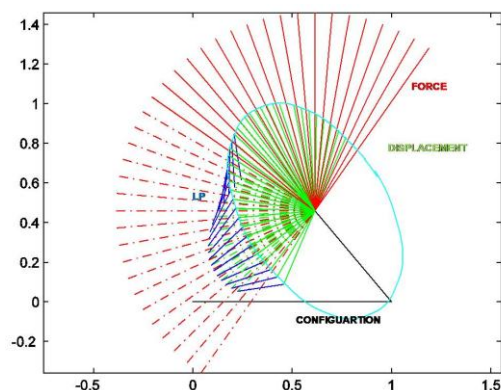


Figure 11 As in Figure 10, with the initial force angle variable from 55° to 145° (solid), together with the cases of the forces rotated by 90° (dashed).

6 REFERENCES

- [1] Vinogradov I. B., Kobrinski A. E., Stepanenko Y. E. And Tives L. T., Details of Kinematics of Manipulators with the Method of Volumes. *Mekhanika Mashin*, pages 5–16, 1971.
- [2] Yang D. C. And Lai Z. C., On the Conditioning of Robotic Manipulators - Service Angle. *ASME J. Mechanisms, Transmissions, And Auto. In Design*, 107:262–270, 1985.
- [3] Kumar, A. and Waldron K. J., The Workspaces of a Mechanical Manipulator, *ASME, Design Engineering Technical Conference*, Beverly Hills (U.S.A.), 1980.
- [4] Yoshikawa T., Analysis and Control of Robot Manipulators with Redundancy. *Robotics Research: The First International Symposium*, pages 735–747, 1984.
- [5] Yoshikawa T., Manipulability of Robotic Mechanisms. *The International Journal of Robotics Research*, 4(2):3, 1985.
- [6] Paul R.P. and Stevenson C.N., Kinematics of Robot Wrists. *The International Journal of Robotics Research*, 2(1):31, 1983.
- [7] Forsythe G.E. and Moler C.B., *Computer Solution of Linear Algebraic Systems*. Prentice-Hall Englewood Cliffs, NJ, 1967.
- [8] Salisbury J.K. and Craig J.J., Articulated Hands: Force Control and Kinematic Issues. *The International Journal of Robotics Research*, 1(1):4, 1982.
- [9] Angeles J. and Rojas A., Manipulator Inverse Kinematics via Condition Number Minimization and Continuation. *International Journal of Robotics and Automation*, 2(2):61, 1987.
- [10] Angeles J. and Lopez-Cajun C.S., Kinematic Isotropy and the Conditioning Index of Serial Robotic Manipulators. *The International Journal of Robotics Research*, 11(6):560, 1992.

- [11] Klein C.A. and Blaho B.E., Dexterity Measures for the Design and Control of Kinematically Redundant Manipulators. *The International Journal of Robotics Research*, 6(2):72, 1987.
- [12] Gosselin C., Dexterity Indices For Planar and Spatial Robotic Manipulators. *Proceedings of the IEEE International Conference on Robotics and Automation*, pp. 650–655, 1990.
- [13] Gosselin C. and Angeles J., A Global Performance Index for the Kinematic Optimization of Robotic Manipulators. *Journal of Mechanical Design*(1990), 113(3):220–226, 1991.
- [14] Klein C.A. and Miklos T.A., Spatial Robotic Isotropy. *The International Journal of Robotics Research*, 10(4):426, 1991.
- [15] Angeles J., The Design of Isotropic Manipulator Architectures in the Presence of Redundancies. *The International Journal of Robotics Research*, 11(3):196, 1992.
- [16] Park F.C. and Brockett R.W., Kinematic Dexterity of Robotic Mechanisms. *The International Journal of Robotics Research*, 13(1):1, 1994.
- [17] Park F.C., Optimal Robot Design and Differential Geometry. *Journal of Mechanical Design*, 117:87, 1995.
- [18] Kim, J. O. and Khosla, P. K., Dexterity Measures for Design and Control of Manipulators, *Proceedings of IEEE International Workshop Intelligent Robot Systems*, Osaka, Japan, pp. 758–763, November, 1991.
- [19] Stocco L., Salcudean S.E. and Sassani F., Mechanism design for global isotropy with applications to haptic interfaces. *Proc. ASME Winter Annual Meeting*, pp. 115–122, 1997.
- [20] Stocco L., Salcudean S.E. and Sassani F., Fast Constrained Global Minimax Optimization of Robot Parameters. *Robotica*, 16(06):595–605, 2001.
- [21] Resconi G. and Jessel R.G.M., A General System Logical Theory. *International Journal of General Systems*, 12:159–182, 1986.
- [22] Belfiore N.P., Faglia R. and Resconi G., Revisiting some Static and Kinematic Features of a SCARA robot by means of GSLT and the Lie Product. *3rd Nat. Conf. on Applied Mechanisms and Robotics*, Cincinnati (USA), November 1993.
- [23] Corke P.I., A robotics toolbox for MATLAB. *Robotics & Automation Magazine*, IEEE, 3(1):24–32, 1996.

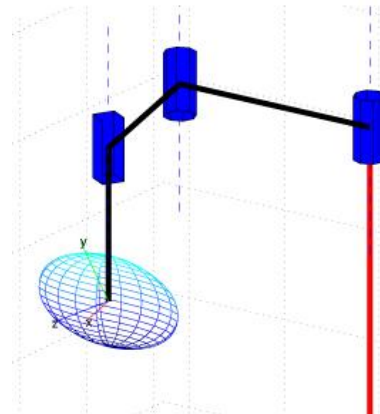


Figure 12 Force manipulability ellipsoid (see also [23]) for the case: $k_1 = 1.1$, $k_2 = 1.3$, $k_3 = 1.2$, $l_2 = 0.9$, $\vartheta_2 = \frac{2\pi}{3}$.

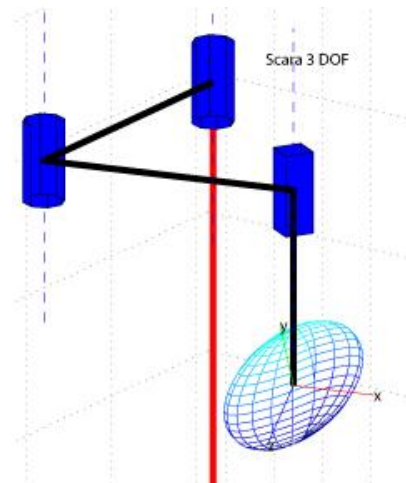


Figure 13 As in Figure 12, with a different view.

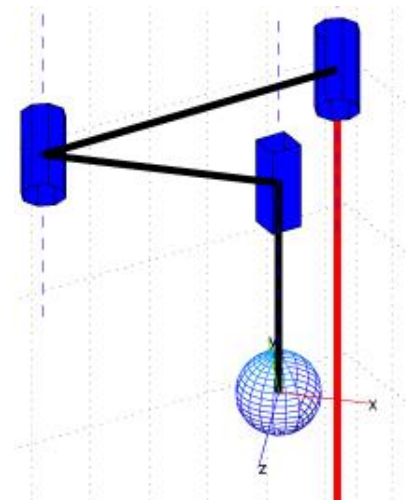


Figure 14 Force manipulability ellipsoid for the case: $k_1 = k_2 = \frac{k_3}{2} = 1$, $l_2 = \frac{\sqrt{2}}{2}$, $\vartheta_2 = \frac{3\pi}{4}$.

7 APPENDIX

7.1 EXTENDED NOMENCLATURE

7.1.1 Kinetostatics (Nomenclature and definitions)

Number of joints in a serial manipulator: n .

The reference system in the joint space:

$$\{\Omega_{(o,q_1,q_2,\dots,q_n)}\} \quad (51)$$

The coordinate vector in the joint space:

$$\{q\} = \{q_1, q_2, \dots, q_n\}^T \quad (52)$$

The velocity vector in the joint space:

$$\{\dot{q}\} = \{\dot{q}_1, \dot{q}_2, \dots, \dot{q}_n\}^T \quad (53)$$

Fixed reference frame: $\{\Sigma_{(O,x,y,z)}\}$.

Reference frame mounted on the end effector: $\{\Xi_{(O',x',y',z')}\}$.

Generalized position of the mobile reference frame:

$$\{s\} = \begin{Bmatrix} p \\ \vartheta \end{Bmatrix} = \{x, y, z, \vartheta_x, \vartheta_y, \vartheta_z\}^T \quad (54)$$

Generalized velocity vector of a point of $\{\Xi_{(O,x,y,z)}\}$ with respect to $\{\Sigma_{(O,x,y,z)}\}$:

$$\{\dot{s}\} = \begin{Bmatrix} v \\ \omega \end{Bmatrix} \quad (55)$$

Geometric Jacobian: $[J]$.

Velocity in the cartesian space:

$$\{\dot{s}\} = [J]\{\dot{q}\} \quad (56)$$

The generalized force $\{F\}$, composed of a force $\{f\}$ and a torque $\{c\}$ is defined in $\{\Sigma_{(O,x,y,z)}\}$ as

$$\{F\}_{(\Sigma)} = \{F_s\} = \begin{Bmatrix} f \\ c \end{Bmatrix} = \{f_x, f_y, f_z, c_x, c_y, c_z\}^T \quad (57)$$

or in $\{\Omega_{(O,q_1,q_2,\dots,q_n)}\}$, as

$$\{F\}_{(\Omega)} = \{F_q\} = \{f_1, f_2, \dots, f_n\}^T \quad (58)$$

Joint stiffness matrix: $[K_Q]$.

Joint reaction vector (under static balance):

$$\{R\}_{(\Omega)} = \{R_q\} = -\{F_q\} = -\{f_1, f_2, \dots, f_n\}^T \quad (59)$$

with

$$\{R_q\} = [K_Q]\{q\} \quad (60)$$

7.1.2 Application of the Principle of the Virtual Works

Variations of the positions in the cartesian space:

$$\{ds\} = [J]\{dq\} \quad (61)$$

Variations of the positions in the joint space: $\{dq\}$

Elementary works exerted by the external force:

$$dL_s = \{F_s\}^T [J]\{dq\} \quad (62)$$

Elementary works exerted by the joint force:

$$dL_q = \{R_q\}^T \{dq\} \quad (63)$$

Joint reaction vector (the virtual and the elementary displacements are supposed to be coincident):

$$\{R_q\} = [J]^T \{F_s\}. \quad (64)$$

Since

$$\{R_q\}^T \{\delta q\} = \{F_s\}^T [J]\{\delta q\} \quad (65)$$

7.1.3 Manipulator Stiffness and Compliance matrices

The application of the generalized force $\{F_s\}$ changes the position in the joint space, as

$$\{q\} = [K_Q]^{-1} \{R_q\}. \quad (66)$$

Therefore,

$$\{s\} = [J][K_Q]^{-1} \{R_q\} \quad (67)$$

and

$$\{s\} = [J][K_Q]^{-1} [J]^T \{F_s\} = [C]\{F_s\} \quad (68)$$

where

$$[C] = [J][K_Q]^{-1} [J]^T \quad (69)$$

is the compliance matrix. Analogously, it is possible to obtain the stiffness matrix

$$[K] = [J]^{-T} [K_Q] [J]^{-1}. \quad (70)$$

7.1.4 Manipulability ellipsoid (Definitions)

Let

$$|R_q|^2 = \{R_q\}^T \{R_q\} = k_f^2 > 0 \quad (71)$$

a condition on the module of a generalized force exerted at the joint space. From (64), the relation

$$\{F_s\}^T [J] [J]^T \{F_s\} = k_f^2 \tag{72}$$

introduces in the space of feasible cartesian wrenches the force ellipsoid. It can be proved that its axes are proportional to the eigenvalues of the matrix $[J] [J]^T$ and are oriented along its eigenvectors.

Analogously, assuming that

$$|\dot{q}|^2 = \{\dot{q}\}^T \{\dot{q}\} = k_v^2 > 0 \tag{73}$$

from the (56), the relation

$$\{s\}^T [J]^{-T} [J]^{-1} \{s\} = \{s\}^T ([J] [J]^T)^{-1} \{s\} = k_v^2 \tag{74}$$

introduces in the space of the cartesian velocities the manipulability ellipsoid (in velocity). The eigenvalues of the matrix $([J] [J]^T)^{-1}$ are equal to the inverse of those of the $[J] [J]^T$, while the eigenvectors are coincident. The direct result is that those configuration for which the manipulator is able to achieve the highest velocities are, indeed, also those for which the forces are the weakest (and vice versa).

7.1.5 Condition number (Definitions)

Whether

$$k_1 = k_2 = \dots = k_n = k \tag{75}$$

the joint stiffness matrix becomes diagonal

$$[K_Q] = k[I] \tag{76}$$

and from (68) we obtain

$$\{s\} = [J] (k[I])^{-1} [J]^T \{F_s\} \tag{77}$$

and so

$$\{s\} = \frac{1}{k} [J] [J]^T \{F_s\} \tag{78}$$

The condition number is so defined as the ratio of the maximum by the minimum eigenvalue

$$I_{iso} = \frac{(\lambda [C])_{max}}{(\lambda [C])_{min}} \tag{79}$$

7.1 Determination of \mathcal{G}_2 and l_2 .

From (31),

$$\cos \vartheta_2 = -\frac{k_2 l_1}{k_1 + k_2 l_2},$$

which can be introduced in (32) to obtain

$$\left(\frac{l_2}{l_1}\right)^2 = \frac{k_2}{k_1 + k_2}.$$

Since $k_1 = k_2$, substituting

$$\frac{l_2}{l_1} = \pm \frac{\sqrt{2}}{2}$$

in the expression of $\cos \vartheta$ we obtain

$$\cos \vartheta_2 = -\frac{\sqrt{2}}{2}.$$

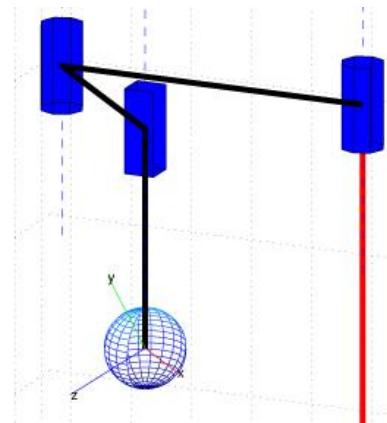


Figure 15 As in Figure 14, with a different view.

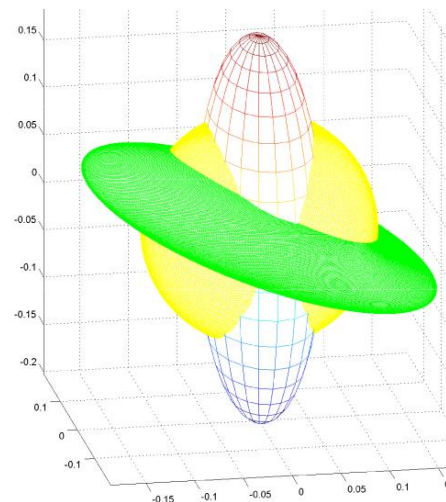


Figure 16 Polar representation of the force (yellow sphere), the manipulability ellipsoid (green mesh), and the Lie Product (blue surface).

THE OPEN-CONTROL CONCEPT FOR HOLONIC MANUFACTURING

Silviu Raileanu * Thierry Berger ** Yves Sallez **
Theodor Borangiu * Damien Trentesaux **

* University Politehnica of Bucharest, Romania

** LAMIH-CNRS, University of Lille Nord of France, Valenciennes, France

ABSTRACT

Nowadays, the advances in information technology and electronics made possible attaching devices with decisional and communicational capabilities to almost all of the entities present in a Flexible Manufacturing System. This allows the passage from the classic centralized control approach to a fully decentralized approach where each entity has its own objectives, making it very hard for the system as a whole to achieve a global objective like minimizing the production time (makespan). In this context the paper proposes a new control concept in which commands from a superior level are not sent in a rigid manner but rather as recommendations. Open-control, along with the holonic manufacturing concept tries to offer the tools needed to face the rising complexity of Flexible Manufacturing Systems.

Keywords: Open-control, holonic manufacturing systems, Contract Net Protocol

1 INTRODUCTION

To be competitive, manufacturing should adapt to changing conditions imposed by the market. The greater variety of products, the possible large fluctuations in demand, the shorter lifecycle of products expressed by a higher dynamics of new products, and the increased customer expectations in terms of quality and delivery time are challenges that manufacturing companies have to deal with to remain competitive. Besides these market-based challenges, manufacturing firms also need to be constantly flexible, adapt to newly developed processes and technologies and to rapidly changing environmental protection regulations, support innovation and continuous development processes [10]. Although the optimization of the production process remains a key aspect in the domain of fabrication systems, adaptive production gains more and more field [14]. Flexible manufacturing systems should be able to quickly adapt to new situations like machine breakdown, machine recovery due to physical failure or stock depletion and also face rush orders [1].

In recent decades, scientific developments in the field of production have defined new architectures including the heterarchical/non-hierarchical architectures that play a prominent role in FMS. This paper is an extension of the work in [12], describing an instantiation of the open-control paradigm, the societal implicit open-control, using the holonic manufacturing concept. This paradigm is an extension of the previous work in the domain of heterarchical control [15] and includes the concept of implicit control in addition to the traditional explicit control. The structure of the paper is: introduction of the open-control paradigm, its description and motivation in section 2, a detailed description of the static model of the fabrication system using the holonic concepts is presented in section 3; Section 4 gives the physical infrastructure, the experiments done and their results. The paper ends with the conclusions and perspectives resulted from the current work.

2 MOTIVATION

Traditional approach is mainly associated to the initial CIM (Computer Integrated Manufacturing) concept and usually leads to centralized or hierarchical control structures. Due to the complexity of manufacturing problems, the usual practice has been to split the overall problem into hierarchically-dependent functions that operate within decreasing time-ranges, such as planning, scheduling and

Contact author: Silviu Raileanu¹

¹ E-mail: silviu@cimr.pub.ro.

control and monitoring. This traditional approach is known to provide near optimal solutions, but only when hard assumptions are met, for example, no external (e.g., rush orders) or internal (e.g., machine breakdowns) perturbations, well-known demands, and/or supplier reliability. Since reality is rarely so deterministic, this approach rapidly becomes inefficient when the system must deal with stochastic behaviour.

The above observations have led researchers to define a second approach to designing control architectures. These control architectures, also called emergent or self-organized, can be categorized in four types [3]: *bionic & bio-inspired*, as proposed by Okino [11] and Dorigo & Stützle [5]; *multi-agent*, as proposed by Maione & Naso [9]; *holonic*, as proposed by Van Brussel [17]; and *heterarchical*, as proposed by Trentesaux [16]. An analysis of the state-of-the-art has been recently published by Trentesaux [15]. His main conclusion is that the expected advantages of such architectures are related to agility: on short term, such architectures are reactive and on long term, they are able to adapt to their environment. However, these last control architectures suffer from the lack of long-term optimality, even when the environment remains deterministic, which can be called “myopic” behaviour. This is the main reason why such control architectures are not really used by industrialists at the moment.

The paper presents an extended model for the global control paradigm, in which traditional control is augmented by a new type of control: “implicit”. In this paradigm, entities can be strictly controlled hierarchically and, at the same time, they can be influenced heterarchically by their environment and/or by other entities. This paradigm would make it possible to design control systems that are both agile and globally optimized, thus reducing the myopic behaviour of self-organized architectures and increasing the agility of traditional architectures. Combining the two types of control in the same architecture causes new challenges since the two types of control must now be managed and integrated within the larger control paradigm.

The work in this paper focuses on the type of control in which an entity tries to achieve its own goals with respect to the global system objectives by the means of a dialogue with the other entities; the entities can be resources or active products, both equipped with decisional and communicational capacities. An *active product* is an entity that is able to inform, communicate, decide and act in order to reach its goals in solving resource allocation and routing problems. (For more details on the typology and advantages of active products see [19]).

The control principle briefly described above will be further called in this paper *open-control*, according to [13], because of the capacity of subordinate levels to receive orders from upper control levels through direct orders (explicit control) and recommendations (implicit control), in which case they exhibit local decisional capabilities to follow their own objectives enabling thus the easy addition and removal of entities.

Based upon the relations between different control levels, Figure 1 shows the two kinds of control: the explicit control, in which the entities from lower levels are subordinated directly to entities on a higher level through an obligatory control relation (e.g., master-slave) and the implicit control, in which the entities at lower levels are influenced by an intermediary optimization mechanism but not necessarily controlled.

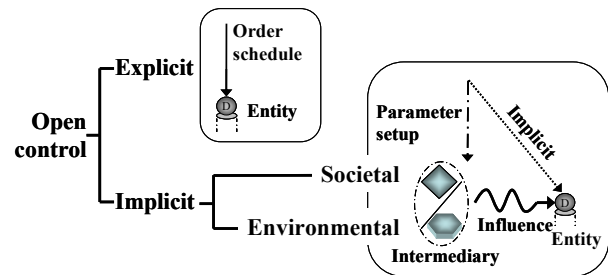


Figure 1 Control typologies present in the open-control concept

Implicit control involves influencing entity behaviour by setting up the parameters of the optimization mechanisms. This type of control works in two stages. First, through explicit control, the superior level directly affects an intermediate entity that plays a role in a societal or environmental optimization mechanism. The affected part of the intermediary entity can be either the decisional mechanism (represented by the diamond in Figure 1) which generates a societal type of control, or it can be a directly the environment which memorizes information (represented by the hexagon in Figure 1). Then, an information exchange (peer-to-peer dialogue or a diffusion process) influences the behaviour of the other entities on the same level.

Taking into account the way the upper control level influences the lower levels, implicit control is of two types:

- I. **Implicit control via a Societal Optimization Mechanism (SOM).** In this case the upper level either fine-tunes the partial view of a collective property inside an entity, modifying its behaviour and then this entity influences the others through dialogue, or the upper level changes the dynamics of the dialogue in the SOM by modifying the dialogue parameters inside the entity. The key element of implicit control using a societal SOM is the dialogue between entities which leads to the two characteristics of holonic manufacturing systems: autonomy and cooperation [8]. This is why this concept offers good means of implementation for semi-heterarchical control systems which under normal conditions work good with a hierarchical structure but when perturbations take place each entity uses its own decisional capacities to continue production (Ex.: staff holon proposed in PROSA, [17]).

Implicit control via an Environmental Optimization Mechanism (EOM). This type of control is performed using last minute information from the environment [2]. This environment is characterized by a memorization mechanism, which stores data or physical characteristics, and an optimization mechanism that acts upon the memorized information.

3 HOLONIC MODEL OF THE FABRICATION SYSTEM

Based on the PROSA reference model [17] and the production domains presented in [10] the following base elements were identified in a fabrication system: resources, products (blueprints) and orders in execution represented by the physical products which are currently fabricated. Because the entities in the fabrication system are almost all equipped with decisional capabilities we decided to structure the system according to the holonic principles and implement an implicit societal open-control which will confer both the adaptive and optimality characteristics in its operation. The following elements, presented in Figure 2, have resulted after applying the holonic scheme to the flexible manufacturing system: resource holons (RH), product holons, order holons (OH) and expertise holons (staff holon according to PROSA).

The **order holon**, the first key point of the fabrication system, represents the client's order in real-time and is composed of the following informational and physical parts: an augmentation module which enriches the holon with decisional (information processing), communicational (information transport) and memorization (information storage) capabilities, the pallet which associates with the

fabricated product along the production phase providing it transportation services and the passive product which is fabricated/assembled on the pallet. The structure of an order holon emphasizes the recursive propriety of a holon which can be composed of other holons. In this case the order holon contains two resource holons, a pallet used for transportation with an augmentation module used to process information, and a product holon representing the blueprint containing the operations needed for execution.

Depending on the way the order holon connects to the informational network (RFID, WiFi, Bluetooth, IrDA, etc) and the computational capacities of the local augmentation module the OH intelligence can be divided as follows (Figure 2):

1. At distance, on a distant machine: in this case between the main control system and the physical part (the pallet) exists a synchronization so that the control system is always aware of the current state of the product. Usually this synchronization is done using RFID. In this case the intelligence of an OH is delimited by line 1 in Figure 3;
2. Locally: the main control system is located directly on the physical part. In this case the OH is delimited by line 2 in Figure 3;
3. Hybrid: the main control system runs on a distant dedicated machine and its role is to take high level decisions (ex.: processing resource allocation). Besides this high level control system there is a local control system dedicated to handling alarms, monitoring product status and taking local decisions like routing towards a goal established by the main control system. In this case the intelligence of an OH is delimited by line 3 in Figure 3.

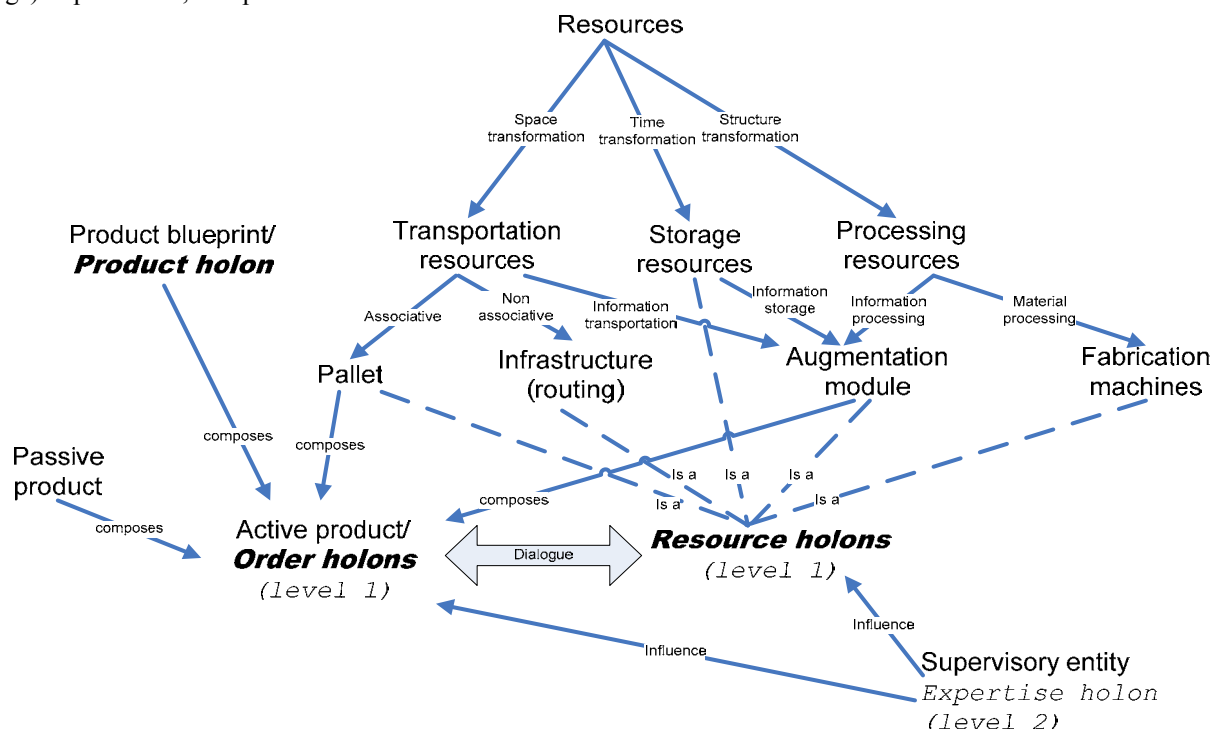


Figure 2 System components (static model)

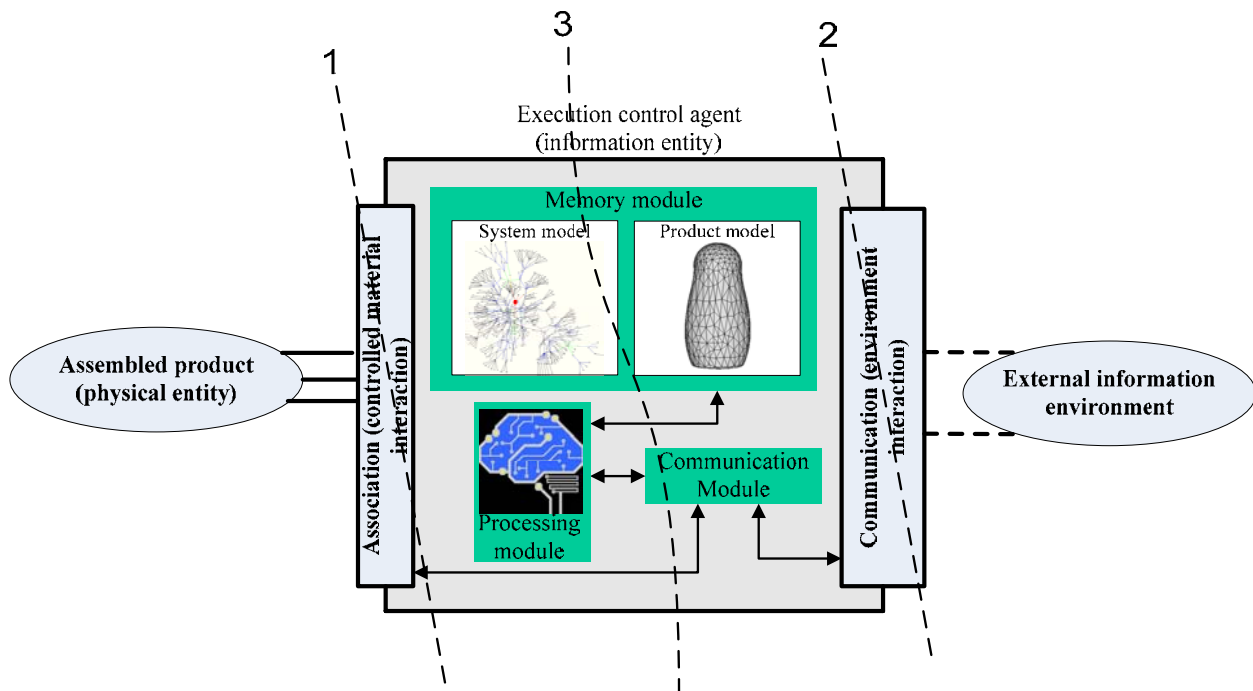


Figure 3 Location of an OH intelligence

The second key point of a fabrication system, the **resource holon**, is composed of an informational part responsible for decision making, control and communication and a physical part responsible with the physical processing (e.g.: mounting a piece on the product, image recording, etc). Depending on the type of operation performed by the resource the system is composed of the following basic types of resources: of processing type offering structural transformation services, of transportation type composed of motion infrastructure (ex.: conveyor belt or conveyor segment) and mobile entities (ex.: mobile shuttle/pallet) which together offer spatial displacement services and storage type offering time locating services. Moreover, each resource can be further classified, according to the entity upon the function is exercised, into information processing (as is the case of the augmentation module) and material processing (as is the case of an industrial robot working upon a product).

For the logical part of the system to be in conformity with the societal open-control concept proposed, the entities of the system are distributed on a 2 layer architecture, a low decisional level and a high decisional level. Usually a factory is composed of three levels [13]: strategic problem solving at the top (level 3), tactical problem solving in the middle (level 2) and operational problem solving at the bottom (level 1), our architecture taking into account level 1 and 2.

The low decisional level (level 1) is composed of autonomous entities, OHs and RHs, which communicate in order to optimize their production schemes. The high decisional level (level 2) is useful at providing general guidance, through the influence of the OM existing at level

1 (Ex.: explicitly modifying the local view of an entity, like the set of corresponding entities to communicate with), in order to attain a global objective; otherwise the low decisional level might have an uncontrolled emergent behaviour. The high decisional level is represented here by the coordinator holon which besides general guidance offers a mean of integrating the fabrication system into the upper layers of the factory (Ex.: attaching client demands to order holons, supervision of the system, computing parameters describing the global behaviour of the system, etc).

Although an FMS is composed of transportation, processing and storage resources, for fabricating a product only the processing resources are mandatory; the others are used to automate the transportation process. For this reason when executing a product the decisional module should provide an answer to the following questions: What is the next operation? What is the resource that will do that operation? How do I bring the product there? The last two questions are being considered together in order to minimize the sum of the processing and routing times. According to Figure 4 the general order execution process is composed of the following three subprocesses:

- First, an order (seen as an active decisional product) *updates its personal knowledge* about the possibilities of each resource from the system (A);
- Second, a *decision* that regards the three questions posed above is taken (operation, **R**esource for **P**rocessing (RP), **R**esource for **R**outing (RR)) (B);
- and third step, *execution* (C) takes place.

The extended process is a modified version of the Contract Net Protocol [7] and is described in Figure 5.

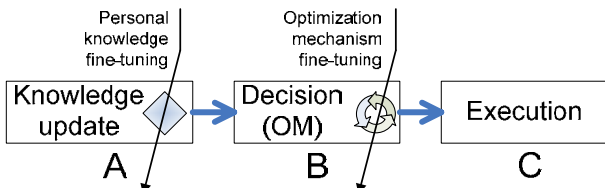


Figure 4 General order execution process

Figure 4 represents the dynamic interaction of the decisional entities presented in Figure 2 for optimizing the allocation and execution operations according to the implicit type of control. The choice for the product to be manufactured is done by the augmentation module in a

fixed location, the input/output of the system. Once a product is chosen it cannot be changed unless its production was completed or it was compromised in the manufacturing process. In order to find out what type of product should be attached to the pallet, the augmentation module interrogates the client's orders database, then the system resources and then, according to the products deadlines, to their complexities and also to the charge of the system a single product representing a production order is chosen for fabrication.

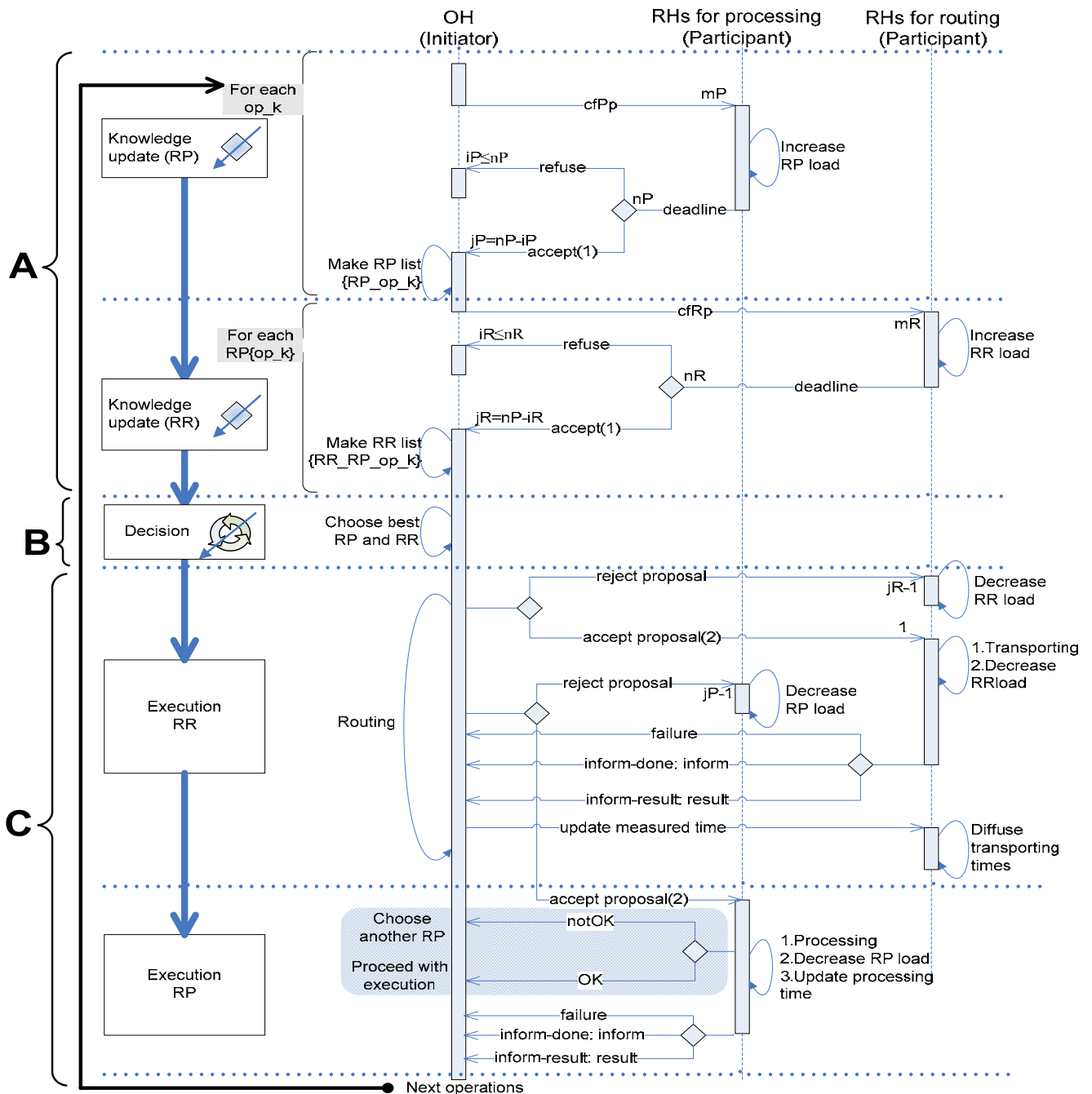


Figure 5 Interactions between order holons and resource holons for optimizing the allocation and execution operations

The interaction process between an OH and the RHs, representing the dialogue arrow in Figure 2, begins with the "knowledge update" stage during which each operation of the order (op_k , $k=1:\text{total_number_of_operations}$) is tested to see if there is a corresponding resource capable of executing it. Then, for each resource found capable of executing a processing operation a path towards it is searched (For each $RP\{op_k\}$). The knowledge update process takes place two times, once for each type of resource (processing and routing). The information exchanged and the way it is exchanged being almost the same except that it is done for different type of resources: update the processing model and update of the routing model.

The updating model process relies on the exchange of information between entities a using messaging mechanism. The messages to resources are sent in the form of call for proposals (*cfPp* referring to calls made for processing resources and *cfRp* referring to calls made for routing resources) and because the dialogue is synchronous, in order not to block an order waiting for a response from a failed resource, timeouts for replies are imposed: if the resource does not respond in the established interval it is declared off-line and it is not taken into account during the decision making process. If the resource replies in this interval the answer can be negative or positive. The negative answer represented by the *refuse* arrow in Figure 5 indicates that the state of the resource does not permit to execute the requested operation because the resource is busy with other products, or the resource can not execute the requested operations; in both cases the resource is operational. The positive response is represented by the *accept* arrow that indicates the availability of the resource to execute the requested operation.

After the "knowledge update" process the model of the system is ready and the order holon can begin the decision process which regards the manufacturing stage: what is the next operation, on what resource it's done and what is the path to the resource.

After the above decisions are taken, the workloads of the chosen routing and processing resources are increased. This process is represented on the diagram of the interactions in negative logic (to respect the standard Contract Net Protocol [7]), with the aid of the *proposal reject* message which is sent to all the resources that have participated in the dialogue and have not been chosen; in order not to increase and then decrease resource charge during each dialogue it was chosen to increase only once the charge, after the decision, when the chain of resources is finally chosen.

Figure 5 shows the case where only a single order holon interacts with the resources of the manufacturing system. In the real case there are several products, the resources being able to face all of them.

The start of an operation, of routing or processing type, is marked by the *accept proposal* message, which in the case

of processing resources may contain additional parameters (e.g.: the points between which an assembly operation is done). Before the production order enters the processing resource a last dialogue takes place between it and the corresponding resource in order to confirm the production possibility. After the *accept proposal (2)* message, the chosen resource must send a message that contains either *OK*, which means that the product can enter, or *notOK*, which means that either the resource broke up during the routing phase of the order holon or another product is in execution or there is no raw materials in the workplace. In this last case the OH jumps at the knowledge update state, seeking another answer to the three questions from above.

The end of an operation is marked by the reception of one of the following messages *inform-done*, *inform-result* or *failure*. *Inform-done* is a simple message sent if the resource has well finished the operation. If more information is required then the resource can send a detailed message of the execution, *inform-result*. *Failure* is a simple message sent by the resource to inform that the requested operation has failed (e.g.: the video inspection has not found the requested characteristics of the object).

For other order holons to take into account the transportation times in real-time (e.g.: instantaneous charge of a line between two resources), travel times are measured and then written at the destination transport resource with the aid of *update measured time* message; this time is then diffused to all the other transport resources via a broadcast mechanism.

The optimization mechanism (OM) is done using the dialogue between the entities of the system. The information exchanged in order to minimize the makespan is the charge of each resource.

4 EXPERIMENTAL RESULTS AND PERSPECTIVES

The open-control concept presented above is currently under deployment at the Flexible Manufacturing System at AIP PRIMECA Valenciennes, Figure 6, composed of a multi-path conveyor, self-propelled pallets with embedded decision capabilities, and flexible workstations with industrial robots and visual inspection cameras.

The transporting resources are composed of the underlying infrastructure on which the physical support of the order holons progress, along with the control represented by WAGO PLCs [18] that drive the transfer gates according to the commands received from the order holons. The processing resources are represented by the corresponding workstations controllers and by the PLCs that are used as interfaces to the workstations controllers. The interactions between resources and orders (Figure 7) take place in special places via an Ethernet-IrDA bridge which aids to both communication and localisation purposes. In our case the bridges consist of IrDa Clarinet systems ESB 101 [4] located for the transporting resources before the transfer gates and for the processing resources in the station workplace.

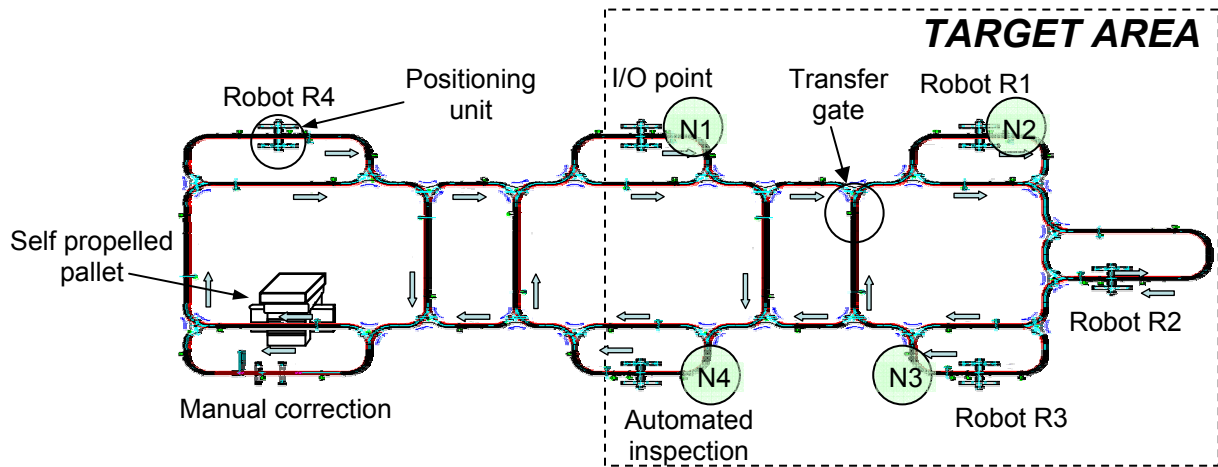


Figure 6 AIP cell system layout

The practical results achieved till now, *dynamic routing* and *resource allocation*, were conducted on a small scale model of a real FMS, more precisely the TARGET AREA zone in Fig.6, and were satisfactory in terms of correctness of operations and stability of the system in face of disturbances such as perturbations jams on the transportation infrastructure.

The implementation of the routing part from the general interaction scheme, presented in detail in Figure 5, is done on a small scale model as depicted in Figure 6 making use of the MODBUS protocol which already exists on the PLC controlling the resources. On the down side the entities that participate at the dialogue are shown, the order holons and the resource holons; in the upper part an adaptation of the general dialogue, the routing with the allocation, from Figure 4 is presented.

Before starting execution, or after finishing an operation the online allocation of the next operation takes place as depicted in Figure 7. Afterwards, the routing towards the selected resource is done.

When the Order Holon arrives at a routing node, the following messages are exchanged after connection for the routing purpose:

- The OH transmits the time measured that it took to travel from the previous node to the current one and the RH broadcasts it to the other RHs updating thus in real-time the routing information;
- Information about the current resource is read from its control PLC;
- The transportation times are sent to the OH, which updates its routing model and chooses the best neighbor by locally applying the Dijkstra routing algorithm [6], work detailed in [19];
- The OH sends a routing demand to the current RH which acts upon the transfer gate.

The future developments to be considered are the implementation of the routing procedure and the online allocation procedure on the real FMS from Figure 6 and then do a comparison between a static (offline) allocation

and the online allocation using the societal open-control concept and holonical approach.

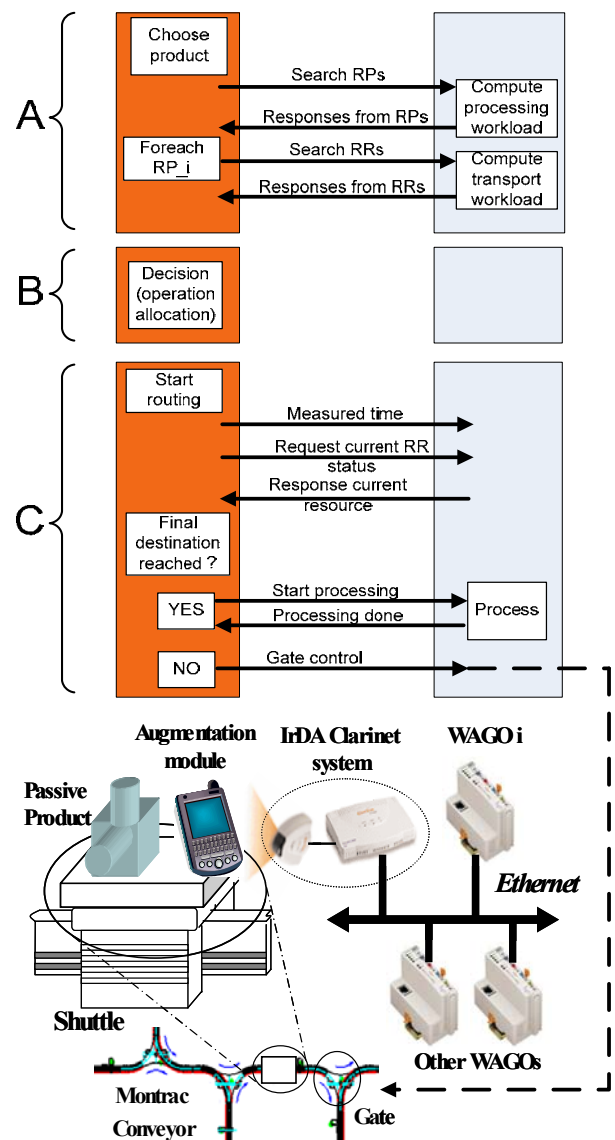


Figure 7 System architecture and order-resource

5 CONCLUSIONS

In this paper we have presented the societal open-control, a control paradigm well suited for decentralised FMS, which combines the advantages of “classical” control architectures, the possibility of hierarchical systems to achieve a global optimum, and the reactivity and easy maintenance due to easy removal and addition of composing elements of heterarchical systems. All these advantages induce a certain price in terms of extensive work and programming knowledge needed which are nevertheless justified if the designed fabrication system should offer an increased productivity and great flexibility. Also, in this paper we tried to show that the open-control concept, and especially the implicit societal part, works very well into a holonic manufacturing system, since the proposed dialogue between entities is key element of the holonic theory.

REFERENCES

- [1] Borangiu, T., Ivanescu, N., Raileanu, S., Rosu, A., Vision-Guided Part Feeding in a Holonic Manufacturing System with Networked Robots, RAAD 2008, Ancona, Italy.
- [2] Borangiu, Th. and M. Dupas, Feature-Based Modelling in Robot Vision Tasks, Proc. of the Int. Conference on Feature Modeling and Advanced Design-For-The-Life-Cycle Systems FEATS 2001, Valenciennes France, June 2001.
- [3] Bousbia, S. and Trentesaux, D. Self-Organization in Distributed Manufacturing Control: state-of-the-art and future trends. In proc. of IEEE SMC'02, Tunisia, 2002.
- [4] Clarinet System, Network Connectivity for Mobile Devices, <http://www.clarinetsys.com>, 2009.
- [5] Dorigo, M., and Stützle, T. Ant Colony optimization. The MIT Press, 2004.
- [6] Dijkstra E W, ‘‘A note on two problems in connexion with graphs’’. Nu-merische Mathematik, 1:269,271., 1959.
- [7] FIPA, 2002, FIPA Contract Net Interaction Specification, www.fipa.org, consulted in February 2009.
- [8] Koestler, A. The Ghost in the Machine. Hutchinson publishing Group, London, 1967.
- [9] Maione, G., and Naso, D. A soft computing approach for task contracting in multi-agent manufacturing control. Computers in Industry, 52, 199–219, 2003.
- [10] Nylund H., Kai Salminen, Paul H Andersson, A multidimensional approach to digital manufacturing systems, 5th International Conference on Digital Enterprise Technology Nantes, France 2008.
- [11] Okino, N. Bionic Manufacturing System in Flexible Manufacturing System: past – present – future. J. Peklenik (ed), CIRP, Paris, 73-95, 1993.
- [12] Raileanu, S., Sallez, Y., Berger, T., Borangiu, T., Trentesaux, D., Holonic implementation of the open-control paradigm, IESM' 2009, May 13 - 15, 2009 Montreal, Canada.
- [13] Sallez Y., Berger T., Trentesaux D., Open-control: a new paradigm for integrated product-driven manufacturing Control, 13th IFAC Symposium on Information Control Problems in Manufacturing (INCOM '09), Russia, June 3-5, 2009.
- [14] Sauer O., Automated engineering of manufacturing execution systems – a contribution to “adaptivity” in manufacturing companies, 5th International Conference on Digital Enterprise Technology Nantes, France 2008.
- [15] Trentesaux, D. Les systèmes de pilotage hétérarchiques : innovations réelles ou modèles stériles ?. Journal Européen des Systèmes Automatisés, 41 (9-10), 1165-1202, 2007.
- [16] Trentesaux, D., Dindeleux, R. and Tahon, C. A MultiCriteria Decision Support System for Dynamic task Allocation in a Distributed Production Activity Control Structure. Computer Integrated Manufacturing, 11 (1), 3-17, 1998.
- [17] Van Brussel, H., Wyns, J., Valckenaers, P., Bongaerts, L. and Peeters, L. Reference architecture for holonic manufacturing systems: PROSA. Computers in Industry, 37 (3), 255–274, 1998.
- [18] Wago system, innovative connections, <http://www.wago.com>, 2009.
- [19] Zbib, N., Raileanu, S., Sallez, Y., Berger, T. and Trentesaux, D. From Passive Products to Intelligent Products: the Augmentation Module Concept. 5th International Conference on Digital Enterprise Technology, Nantes, France, 2008.

A 3D-LASER SCANNER FOR AUTONOMOUS MOBILE ROBOTS

Giulio Reina* Nicola I. Giannoccaro* Arcangelo Messina* Angelo Gentile**

* Dipartimento di Ingegneria dell'Innovazione, Università del Salento, Lecce, Italy

** Dipartimento di Ingegneria Gestionale e Meccanica, Politecnico di Bari, Bari, Italy

ABSTRACT

An efficient and reliable onboard perception system is critical for a mobile robot to increase its degree of autonomy toward the accomplishment of the assigned task. In this regard, laser range sensors represent a feasible and promising solution that is rapidly gaining interest in the robotics community. This paper describes recent work of the authors in hardware and algorithm development of a 3-D laser scanner for mobile robot applications, which features low-cost, lightweight, compactness, and low power consumption. The sensor allows a vehicle to autonomously scan its environment and to generate an internal hazard representation of the world in the form of digital elevation maps. This suggests a general approach to terrain analysis in structured and unstructured environments for a safe and collision-free path planning. The proposed sensor system along with the algorithms for mapping and planning is validated in indoor laboratory experiments as well as in tests on natural terrain using an all-terrain rover.

Keywords: Sensors for mobile robots, laser range-finder, digital elevation map, path planning

1 INTRODUCTION

In order for a mobile robot to perceive effectively the surrounding environment, a suitable onboard sensor technology is primarily required. The choice of sensors for mobile robotics depends on several criteria, such as price, performance, weight, and size of the device. In the last few years, 3-D laser scanners, which are also commonly referred to as LASer Detection And Ranging (LADARs), and LIght Detection and Ranging (LIDARs), have increasingly been adopted in robotics thanks to their precision and wide scanning range [1], [2]. LIDARs measure the distance to objects within their field of view, providing as output a cloud of points with 3-D coordinates. The main problem with conventional 3-D scanners is their size and weight; typical values of weight and height are 7.5 kg and 25 cm, respectively. Thus, they are rather oversized, bulky and heavy for mobile robots, especially when considering applications on rough-terrain or in confined environments, such as pipe and sewer inspection. Recently, Hokuyo has delivered to the market a light 2-D laser scanner, which is gaining increasing interest in robotics [3].

Based on the Hokuyo planar sensor, a lightweight and small 3-D scanner has been developed at the University of Salento for mobile robot applications. With this sensor, a robot can analyze its environment in three dimensions and autonomously recognize and avoid obstacles along its path. The sensor can be useful for both structured and unstructured environments. Examples of potential application can be found in the so-called in-pipe robotics to enable detection methods of cracks and defects along gas, oil and water transmission mains and sewers [4], and for search and rescue robots to map the environment of collapsed buildings and of disaster areas in general [5]. This sensor modality can be of great value to open new application fields, such as automatic health diagnosis of aeronautical structures, using non destructive testing methods [6]. Terrain unevenness and non-traversable obstacles represent a critical issue for outdoor applications, as they may prevent robots from accomplishing certain tasks by invalidating path plans. In the worst-case scenario, it may even result in vehicle's entrapment and physical damage. Valuable resources can be saved by allowing the robot to resolve most obstacles automatically and requiring manual intervention only when absolutely necessary. However, the application of LIDAR to terrain characterization has only recently been suggested. Roberts proposed a fixed-mount laser range finder attached to the front of vehicles to detect immediate obstacles and terrain

Contact author: G. Reina¹

¹ Dipartimento di Ingegneria dell'Innovazione,
Università del Salento, via Arnesano, 73100 Lecce, Italy
E-mail: giulio.reina@unisalento.it

hazards [7]. The sensor is able to gather terrain information only if the vehicle is moving, but the setup is very popular due to its ease of construction and use. While this is sufficient for simple obstacle avoidance, it does not contribute to autonomous robots that navigate by path planning. In order to avoid obstacles in autonomous plans, knowledge of the probable area of traverse must be obtained. In [8], Henriksen and Krotkov compared the performance of LIDAR with vision in detecting terrain hazards. Positive elevation hazards, also known as “steps” indicate an abrupt rise in the level of terrain. This class of hazards includes boulders, natural perforations in the landscape and broken rock surfaces. Both laser and vision perform equally well in detecting step hazards. Negative elevation hazards, called “ditches,” represent abrupt downgrades in the landscape such as craters and cliffs. Laser range finders present a drastic improvement over vision-based methods in detecting negative hazards due to difficulties in identifying distances through vision.

In summary, accurate and reliable perception is generally beneficial for autonomous mobile robots to map the surrounding environment, or to precisely localize itself, or for hazard detection and avoidance. In this paper, laser-generated elevation maps are used for path planning purposes. An algorithm is proposed to find an optimal path between a starting point and a final point of interest, which minimizes the distance to the target and ensures at the same time its safety in terms of danger of entrapment and collision of the vehicle due to terrain roughness or non-traversable obstacles. For the extensive testing of the system during its development, we employed the rover Dune, built at the Applied Mechanics Laboratory of the University of Salento, and shown in Figure 1. Dune is an independently controlled 4-wheel-drive/4-wheel-steer mobile robot, also featuring a rocker-type suspension system, which provides remarkable mobility over obstacles and on natural terrain, in general, allowing the rover to safely traverse rocks over one and half its wheel diameter [9]. In the same Figure 1, the 3-D laser scanner is visible, mounted to the front of vehicle’s body. The robot is also equipped with wheel and steer encoders and an IMU to

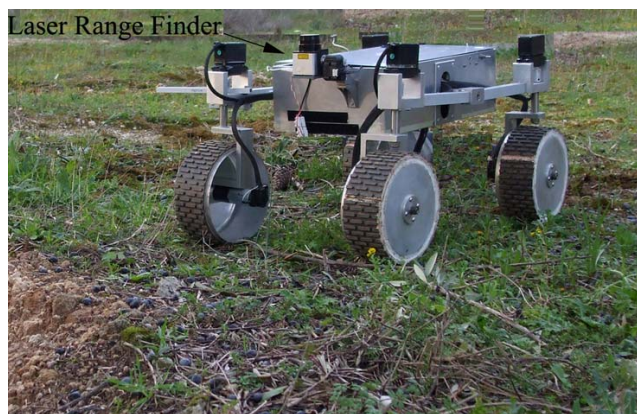


Figure 1 The all-terrain rover Dune, built at the University of Salento.

measure robot’s orientation. Its operational speed ranges from 2 to 30 cm/s.

The paper is organized as follows. In Section 2 the 3-D laser scanner is presented along with the algorithm to generate digital map of the environment. In Section 3, the path planning method is described and demonstrated for indoor and outdoor scenarios. Relevant conclusions are drawn in final Section 4.

2 THREE-DIMENSIONAL LASER SCANNER

Conventional 2-D laser scanners detect objects intersecting their planar field of view. Thus, they fail to recognize ground-level hazards or over-hanging obstacles. This is explained in Figure 2(a). By controlling the inclination of the sensor with respect to the ground (nodding angle), using a servomotor, a full three-dimensional scan of the environment in front of the vehicle can be obtained, as illustrated in Figure 2(b). The proposed 3-D laser scanner is shown in Figure 3. It consists of a planar Hukoyo URG-X002 scanner coupled with a DX-117 Dynamixel servomotor. Its main advantages are the relative low price (about 1.2k €, ten or twenty times lower than current commercial 3-D laser scanners), the weight, the size and the low energy consumption. A mobile robot outfitted with this 3-D scanner can autonomously recognize and avoid obstacles along its way, generate digital maps of the environment and improve its degree of mobility. The Hukoyo sensor is based on the amplitude modulation of a continuous laser beam. By observing the phase shift between the outgoing and return signals, the transit time can be estimated and from this the target distance. The laser scanner can survey the part of a spherical volume with external radius up to 4 m and internal radius down to 0.02 m; the angular span is 240 deg in the horizontal plane with a resolution of 0.36 deg, whereas the servomotor controls

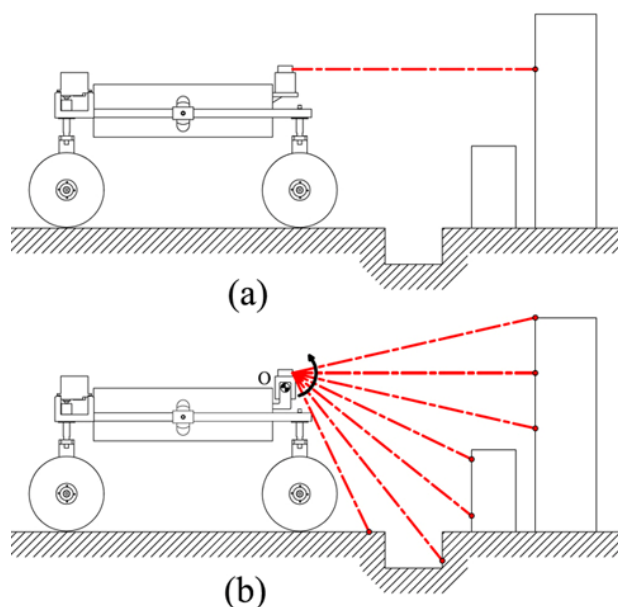


Figure 2 Extending laser field of view from 2D to 3D.



Figure 3 The 3-D laser range finder.

the angular sweep in the vertical plane up to 270 deg and with a resolution of 0.36 deg. The nominal accuracy is of 10 mm up to 1-meter distance and of 2% of distance for higher measurements. Overall, 240 deg × 270 deg point clouds can be acquired in 13 sec. However, note that in the practical implementation of the system a vertical sweep ranging from -90–45 deg is adopted, which was found to be optimal for effective terrain analysis, reducing the scan time to 6 sec. The overall weight of the sensor is 0.4 kg and it fits in a rectangular volume of 0.08 × 0.05 × 0.07 m. Table I collects the relevant sensor specifications.

The laser range sensor generates a 3-D representation of the scene around the robot. The raw sensor data are expressed as an image $d(i, j)$, which records the distance d along the line of sight of the laser ray through image pixel (i, j) to the corresponding scene point $P(x, y, z)$. Based on the sensor geometry, a spherical mapping exists from $(i, j, d(i, j))$ to (x, y, z) , as shown in Figure 4. The sensor rotates about the Y -axis and X -axis. Thus, (i, j) represent the azimuth and elevation of the line of sight, α_i and β_j , respectively, and

$$P = \begin{bmatrix} x \\ y \\ z \end{bmatrix} = \begin{bmatrix} d(i, j) \cdot \cos \beta_j \cdot \sin \alpha_i \\ d(i, j) \cdot \sin \beta_j \\ d(i, j) \cdot \cos \beta_j \cdot \cos \alpha_i \end{bmatrix} \quad (1)$$

The system outputs a cloud of points with 3-D coordinates associated with each point. As an example, two point clouds obtained from the laser range finder are shown in

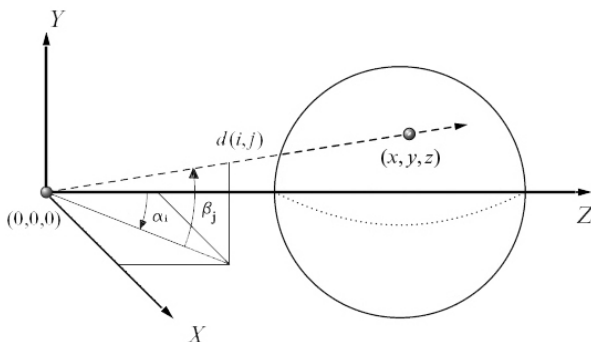


Figure 4 Spherical mapping.

Table I - Sensor specifications

Detection range	20–4095 mm
Accuracy	±10 mm (20–1000mm) 2% of distance (1000–4095mm)
Horizontal sweep	240 deg
Vertical sweep	270 deg
Resolution	0.36 deg
Dimensions	80 × 50 × 70 mm
Weight	0.4 kg
Power	1.7 W

Figure 5 and Figure 6 for an indoor and outdoor environment, respectively. In Figure 5(a) a laboratory scenario is shown with smooth planar floor and five cylindrical-shaped objects with 0.013–0.15 m radius and 0.5–0.7 m height. The output of the sensor for this scene is illustrated in Figure 5(b).

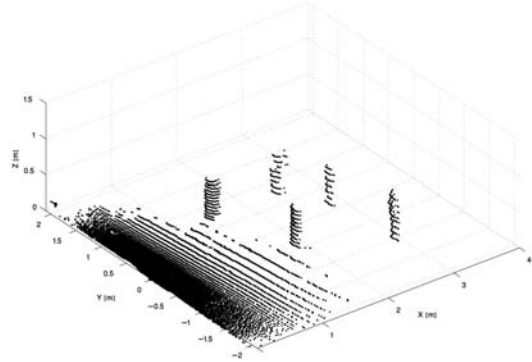
An outdoor scenario is shown in Figure 6(a), where the rover surveys the environment across from it comprising agricultural terrain with sparse rocks and low vegetation, and an olive tree at the center of scene. The corresponding point cloud is reported in Figure 6(b). Note that both acquisitions were performed while the rover was stopped.

2.1 DIGITAL ELEVATION MAP

The problem of learning maps with mobile robots has been



(a)

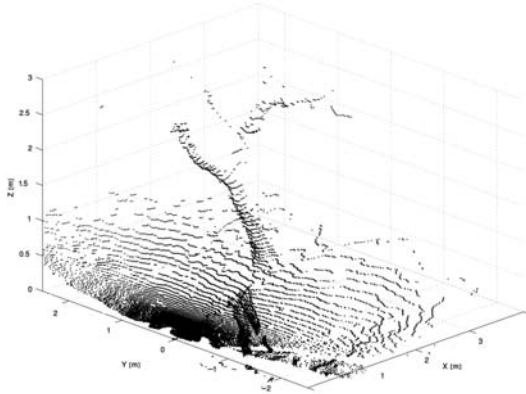


(b)

Figure 5 Indoor environment: Real scene (a), and correspondent point cloud (b).



(a)



(b)

Figure 6 Outdoor environment: Real scene (a), and correspondent point cloud (b).

intensively studied in the past. In the literature, different techniques for representing the environment of a mobile robot were proposed. Topological maps aim at representing environments by graphlike structures, where edges correspond to places, and arcs to paths between them.

Geometric models, in contrast, use geometric primitives for representing the environment. Although topological maps have the advantage of better scaling large environments, they lack the ability to represent the geometric structure of the environment that is essential in unstructured outdoor environments where the ability to traverse specific areas of interest needs to be accurately known. In general, full three-dimensional models have too high computational demands for a direct application on a mobile robot. Instead, most systems use an elevation model. Elevation maps have been introduced as a more compact $2\frac{1}{2}$ -dimensional representation, which assumes that the terrain can be represented as a function $h = f(x, y)$, where x and y are the coordinates on a reference plane and h is the corresponding elevation. Firstly, the proper grid size s needs to be fixed, which is usually 10 cm or 15 cm. The finer the map, the higher the computational cost. Secondly, each 3D data point $P = (x, y, z)$ collected from ladar is assigned to a cell (i, j) as

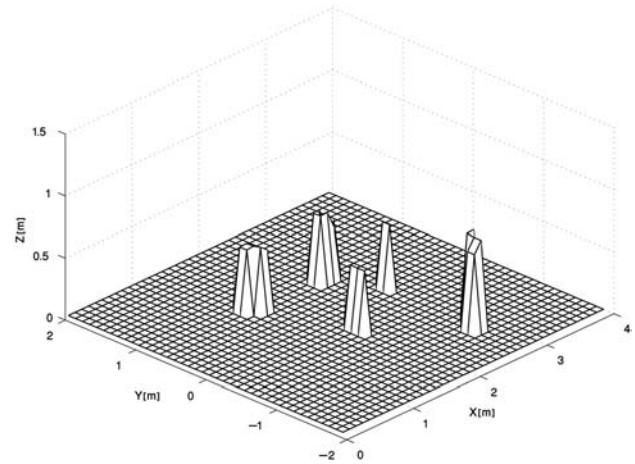


Figure 7 Dem obtained from the point cloud of Figure 5.

$$i = \left\lceil \frac{x}{s} \right\rceil \quad (2)$$

$$j = \left\lceil \frac{y}{s} \right\rceil$$

where the function $\lceil a \rceil$ gives the smallest integer greater or equal to a . In general, a cell (i, j) can have k points $P_k(i, j)$. After cells have been assigned to points, the elevation of a cell can be computed. In its simplest implementation, the digital elevation map (dem) just contains the mean height of range points above the nominal ground plane. Because they are simple data structures and can be generated from sensor data in a relatively straightforward manner, elevation maps have been extensively used for mobile robots operating in natural environments. Elevation maps marked with obstacles have obvious utility for planning and collision-free path for the vehicle.

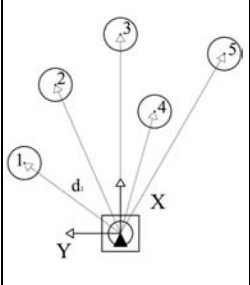
As an example, the dem, obtained from the indoor acquisition described in Figure 5 of Section 2, is shown in Figure 7. An elevation model appears as a tessellated $2\frac{1}{2}$ -D representation of space, where at each cell there is information about the distribution of 3-D points in that cell. A regularly sampled grid was adopted with square cells of 0.1 m and an overall extension of $4\text{m} \times 4\text{m}$. In order to assess the accuracy of the digital model, the distance d from the obstacles, as estimated by the dem, was compared with the actual one, as measured manually with a ruler. A percentage relative error E_i was defined as

$$E_i = \frac{\sqrt{(S_{x,i} - M_{x,i})^2 + (S_{y,i} - M_{y,i})^2}}{\sqrt{S_{x,i}^2 + S_{y,i}^2}} \quad (3)$$

where $M_i = (M_{x,i}, M_{y,i})$ is the location of the obstacle i estimated by the laser scanner with reference to its geometrical center, and $S_i = (S_{x,i}, S_{y,i})$ the ground truth. Table II collects the localization error E_i along with a similarly-defined error H_i in the measurement of the height of each object. The obstacles were located with an average error

Table II - Errors in obstacle localization (E_i) and height measurement (H_i)

Obstacle	d (m)	E_i (%)	H_i (%)
1	1.4	4.6	8.0
2	3.0	3.7	4.0
3	3.1	2.2	3.3
4	2.1	1.9	2.0
5	3.4	2.0	4.5



within 4.0% and a worst-case measurement of 4.6%. Similar results were obtained for the estimation of the obstacle height. Generation of dems, however, can be problematic in presence of vertical surfaces or overhanging objects, such as branches of trees and bridges. For example, consider the three-dimensional data points shown in Figure 6(b). They have been acquired with the rover standing in front of a tree. The resulting elevation map, which is computed from averaging over all scan points that fall into a given cell is depicted in Figure 8(a). As can be seen from the figure, the branches appear as a non-traversable object.

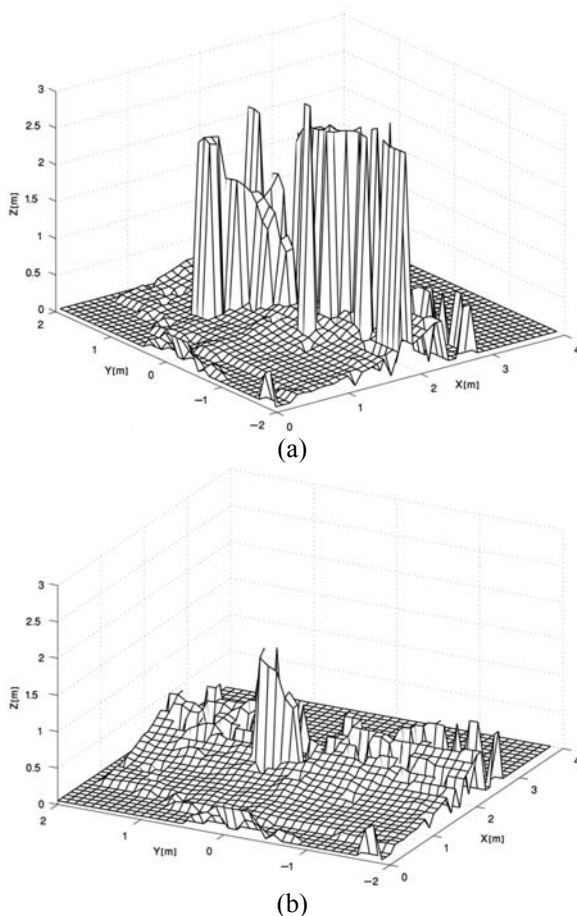


Figure 8 Tree branches appear as non-traversable objects (a), and corrected dem (b).

In order to improve map generation, it is necessary to identify the cells of the elevation map that correspond to vertical structures and those containing gaps. In order to determine the class of a cell, firstly the variance of the height of all measurements falling into this cell is considered. If this value exceeds a certain threshold, it is identified as a point that has not been observed “from above”. Secondly, it is checked whether the point set corresponding to a cell contains gaps exceeding the height of the robot. When a gap has been identified, the minimum traversable elevation in this point set is determined. By applying this approach, a corrected dem can be obtained as shown in Figure 8(b). The area under the branches can now be represented appropriately by ignoring data points above the lowest surface. This, in turn, enables the robot to plan a path through the cells under the branches. Note that, to correctly reflect the steepness of the terrain, a common assumption is that the initial tilt and the roll of the vehicle are known.

3 PATH PLANNING

The availability of a digital map of the environment is generally beneficial for a mobile robot for many obvious reasons, for example, to localize its position, to match known landmarks, and to detect and avoid obstacles or hazardous highly-irregular terrain. In this paper, a path planner is proposed for generating an optimal path through the dem cells, which avoids non-traversable obstacles and minimizes navigation of hazardous rough terrain. The idea is to find a set of neighbouring nodes $p=(n_1, n_2, \dots, n_m)$ toward the target point n_m , which minimizes the danger of entrapment and the occurrence likelihood of the dynamic ill effects, such as longitudinal and lateral slippage, which greatly affect robot's traction and stability properties, and the accuracy of localization systems. To this aim, an objective function can be defined by introducing three indexes: terrain roughness, terrain inclination, and path length [10].

Terrain roughness index—This index estimates the terrain unevenness along the path and aims to minimize the presence of traversable obstacles such as stones, rocks, and boulders, spread along the way. The terrain roughness index B_i can be defined as the standard deviation of the terrain elevation measured in a projection region R_i ($i=1, 2, \dots, m$) of the rover onto the dem, moving along the given path

$$B_i = \sqrt{\frac{1}{n_i} \sum_{R_i} (z(R_i) - \bar{z}(R_i))^2} \quad (4)$$

where n_i represents the number of nodes belonging to the projection patch R_i and $\bar{z}(R_i)$ denotes the average elevation of R_i . The more irregular the terrain, the larger the value of B_i .

Path length index—This index seeks the shortest path between the starting point and the final destination. The path length index L_i between adjacent nodes can be calculated by the following equation

$$L_i = |n_i - n_j| = \sqrt{(x_i - x_j)^2 + (y_i - y_j)^2 + (z_i - z_j)^2} \quad (5)$$

Terrain inclination index—When a rover climbs up a hill or traverses sandy slopes, variations in the load distribution occur on the four wheels of the robot due to longitudinal and lateral weight shifts. This results in an increased likelihood of wheel slippage. This index aims to limit such risk. Two angles measuring the terrain inclination can be defined with respect to the longitudinal and lateral axis of the rover, and denoted with θ_x and θ_y , respectively, as described in Figure 9. The associated indexes, Ω_{xi} and Ω_{yi} , are determined by the average inclination in the projection region R_i :

$$\Omega_{xi} = \bar{\theta}_x(R_i) \quad (6)$$

$$\Omega_{yi} = \bar{\theta}_y(R_i) \quad (7)$$

These indexes provide also indication of the danger of tip-over since the roll and pitch angle of the vehicle are directly related with the terrain inclination. Using the above three indexes, the objective function $C(p)$ to obtain an optimal candidate path p can be defined as follows:

$$C(p) = \sum (W_B N_B B_i + W_L N_L L_i + W_{\theta_x} N_{\theta_x} \Omega_{xi} + W_{\theta_y} N_{\theta_y} \Omega_{yi}) \quad (8)$$

where W_B , W_L , W_{θ_x} , and W_{θ_y} are weighting factors to emphasize each index individually. For example, the smaller W_B , the less the planner will try to avoid terrain irregularities. Note that, W_{θ_x} , and W_{θ_y} are automatically increased if the indexes Ω_{xi} and Ω_{yi} , exceed certain threshold angles, θ_{xmax} and θ_{ymax} . N_B , N_L , N_{θ_x} , and N_{θ_y} are normalization factors, which allow the tree indexes to be compared. The path planning problem can be expressed as the search of the optimal node set p_s that minimizes $C(p)$

$$\min C(p) = C(p_s) \quad (9)$$

In this research, conventional Dijkstra's algorithm is employed [11] to derive the path p_s . Note that rover-like robots are usually controlled, using two primitives of motion: straight motion and turn-on-the spot. The former

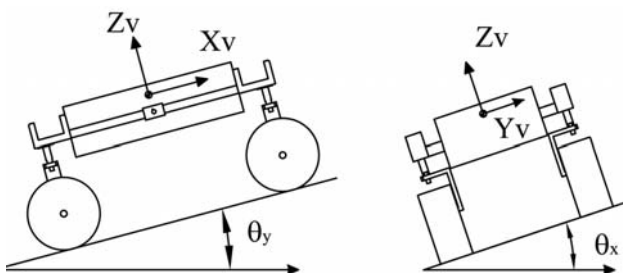


Figure 9 Terrain inclination indexes.

Table III - Weighting factors and thresholds

W_b	W_L	W_{θ}	W_{θ_y}	θ_{xmax} (deg)	θ_{ymax} (deg)
0.3	10.3	0.2	0.2	15.0	15.0

has a curvature path equal to zero, the latter has a pointwise infinitely large curvature. These manoeuvres ensure less likelihood of slippage on uneven terrain [12] and allow translation and orientation to be decoupled. Thus, no path smoothness constraint is required. In order to test the proposed path planning algorithm, some simulations were performed using the dems described in Section 2.1. The set of weighting factors and thresholds used in the simulations is summarized in Table III. It was chosen based on the physical behavior of the rover Dune and on the experience gained during simulations. Figure 10 shows the path obtained from the proposed approach for the laboratory environment of Figure 5, setting as target destination the point $T=(4, 0)$ m. The planner correctly avoids the obstacles present in the scene, resulting in a total travel distance of 4.3 m and three 45-deg turn-on-the-spot maneuvers. When applied to the natural terrain map of Figure 8(b), the algorithm still successfully estimates a safe path avoiding the tree, as shown in Figure 11. Since the final destination T is occluded by the terrain, the planner finds an intermediate destination I within the “visible area”. Planning routes through occluded parts of the environment may be catastrophic since elevation data are entirely unknown and should not be inferred. The intermediate safe destination toward the final goal results in $I=(2, -1.5)$ m. The robot should drive until point I where it can proceed with a new survey of the environment.

5 CONCLUSIONS

In this paper, a 3-D laser scanner was presented featuring low-cost, lightweight, compactness, and low power consumption. It can be employed by mobile robots to

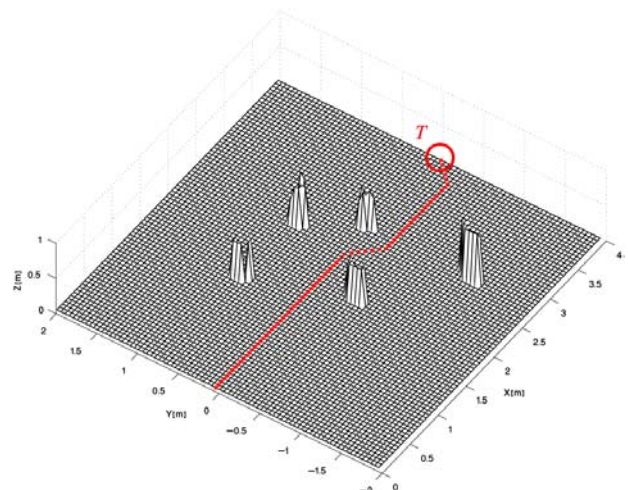


Figure 10 Path planning on flat terrain.

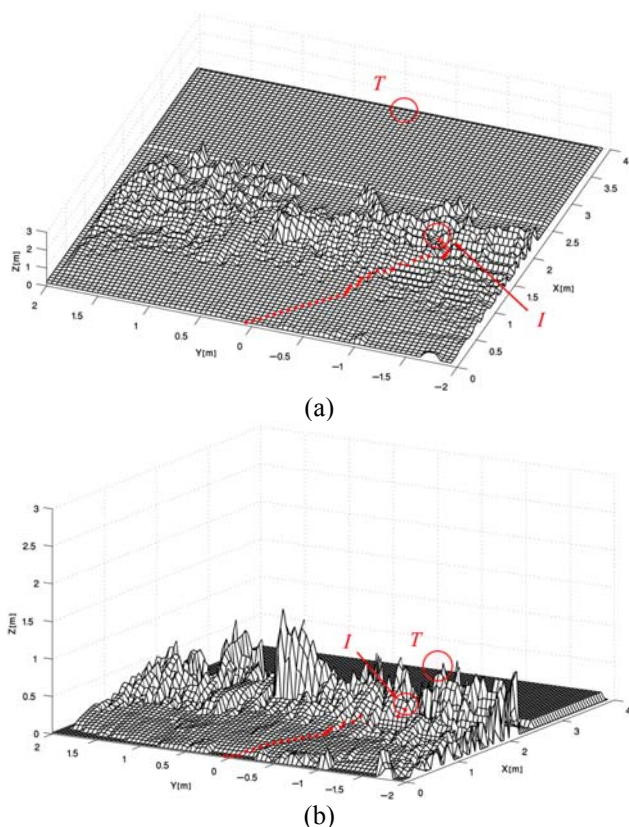


Figure 11 Path planning on rough-terrain from two different perspective views.

improve their degree of autonomy, providing accurate digital elevation maps of the environment. The sensor was experimentally validated in indoor and outdoor scenarios, using an all-terrain rover. It also suggested a general approach to terrain analysis for a safe and collision-free path planning, which was demonstrated through extensive simulations.

REFERENCES

- [1] Thrun S., *Robotic mapping: A survey*. In G. Lakemeyer G. and Nebel B., Editors, *Exploring Artificial Intelligence in the New Millennium*, Morgan Kaufmann, 2002.
- [2] Surmann H., Nüchter A., Lingemann K. and Hertzberg J., A 3D Laser range finder for autonomous mobile robots. *Inter. Symp. on Robotics*, Seoul, Korea, pp. 153–158, 2001.
- [3] Kawata H., Ohya A., Yuta S., Santosh W. and Mori T., Development of Ultra-small lightweight optical range sensor system, *IEEE/RSJ International Conference on Intelligent Robots and Systems*, Edmonton, Canada, pp. 1078–1083, 2005.
- [4] Tătar O., Mândru D. and Ardelean I., Development of mobile mini-robots for in pipe inspection tasks, *Mechanika*, Vol. 6(68), pp. 60–64, 2007.
- [5] Bar-Cohen Y. and Backes P., Scanning Large Aerospace Structures using Open-Architecture Crawlers, *National Space and Missile Materials Symposium*, San Diego, California, USA, 2000.
- [6] Poppinga J., Birk A. and Pathak K., Hough-based Terrain Classification for Realtime Detection of Driveable Ground, *Journal of Field Robotics*, Vol. 25 (1–2), pp. 67–89, 2007.
- [7] Roberts J. and Corke P., Obstacle Detection for a Mining Vehicle using a 2-D laser. *Australian Conference on Robotics and Automation*, Melbourne, Australia, pp. 185–190, 2000.
- [8] Henriksen L. and Krotkov E., Natural Terrain Hazard Detection with a Laser Rangefinder, *IEEE Inter. Conference on Robotics and Automation*, Albuquerque, NM, USA, Vol. 2, pp. 968–973, 1997.
- [9] Foglia M. and G. Reina, Locomotion Performance of an All-terrain Rover, *International Journal of Mechanics and Control*, Vol. 9(2), pp. 13–25, 2008.
- [10] Rohmer E., Reina G., Ishigami G., Nagatani K. and Yoshida K, Action planner of hybrid leg-wheel robots for lunar and planetary exploration, *IEEE/RSJ Intern. Conference on Intelligent Robots and Systems*, Nice, France, pp. 3902–3907, 2008.
- [11] LaValle S.M., *Planning Algorithms*, Cambridge University Press, Cambridge, U.K., 2006.
- [12] Baumgartner E.T., Aghazarian H. and Trebi-Ollennu, A., Rover Localization Results for the FIDO Rover, *Conf. Sensor Fusion and Decentralized Control in Autonomous Robotic Systems*, Newton, MA, USA, Vol. 4571, pp. 34–44, 2001.

MR COMPATIBLE DEVICE FOR ACTIVE AND PASSIVE FOOT MOVEMENTS

Guido Belforte* Gabriella Eula* Giuseppe Quaglia* Silvia Appendino* Franco Cauda** Katuscia Sacco**

* Department of Mechanics, Politecnico di Torino, Torino, Italy

** Department of Psychology, Università di Torino, Italy

ABSTRACT

The present paper presents a new MR compatible robotic device able to induce foot dorsiflexion and plantarflexion movements ('passive' patient mode), or to set and control for a series of parameters (force, amplitude) when the same movements are performed by the subject ('active' patient mode). Recent studies have demonstrated that the foot dorsiflexion is a critical component of the gait cycle; thus, ankle dorsiflexion/plantarflexion has been proposed as part of locomotor rehabilitation protocols, as well as a functional magnetic resonance imaging (fMRI) paradigm for defining brain activity relevant to gait. The principal aim of this work was to develop a robotic device to be used during fMRI testing, in pre- and post-locomotor therapy evaluations of cerebral activity. The same device can furthermore be used in the rehabilitation of neurological paretic patients, who need to practise foot movements and/or to relearn locomotor schemas.

Design criteria and implementation are described, as well as the final prototype. Great concern was given to choice of materials (for MR compatibility) and to anthropometric dimensions (for patient adapting). Furthermore pneumatic circuit and control software are illustrated. Finally preliminary results obtained from a fMRI exam on a healthy subject are pointed up.

Keywords: MR compatible, lower limb rehabilitation, robotics, neuroimaging

1 INTRODUCTION

Functional magnetic resonance (fMRI) is an in vivo imaging technique which allows the mapping of active processes within the brain, thus revealing the cerebral areas involved in a particular motor or cognitive task. Most fMRI studies measure changes in blood oxygenation over time. Because blood oxygenation levels change rapidly following activity of neurons in a brain region, fMRI allows researchers to localize brain activity on a second-by-second basis and within oxygenation occur intrinsically as part of normal brain

millimetres of its origin. Besides, as changes in blood physiology, fMRI is a non-invasive technique that can be repeated as many times as needed in the same individual. It is then used both for clinical aims and for research purposes.

One of the main clinical applications concerns the detection of brain functional changes after rehabilitation programs in order to evaluate their efficacy. Robotics can greatly improve the accuracy of such medical evaluations, especially when the fMRI test is of motor type, i.e. where patient must achieve motor tasks or receive motor inputs during fMRI. For example, the motor rehabilitation of neurological paretic patients can be evaluated through the same fMRI motor task administered before and after the rehabilitation protocol: obviously, the force, the frequency and the amplitude of the limb movements must be identical in the two conditions. As

Contact author: Gabriella Eula¹

¹ Politecnico di Torino, Department of Mechanics
Corso Duca degli Abruzzi, 24 – 10129 Torino Italy
E-mail: gabriella.eula@polito.it

the task usually requires the paretic patient greater efforts before his rehabilitation, a robotic device monitoring for these parameters is essential. Moreover, some patients have difficulty in executing an fMRI motor task because of their brain lesion. In such cases a robotic device inducing passive movement becomes crucial.

Currently MRI compatible devices for the movement of upper limbs have been developed: a force sensing system for monitoring wrist forces and moments exerted by patients during fMRI testing has been proposed in [1]; another device [2] moves the fingers of a hand with the purpose of studying brain activations due to passive hand movement. Furthermore brain activations due to elbow and finger active and passive movements, supported by custom-built devices, are illustrated respectively in [3] and [4].

However, while cerebral activations and modifications following training of the upper limbs have been more extensively investigated, less is known about the functional organization and reorganization of the lower limbs. In particular, investigations of the foot extension and flexion movements would be of special interest, as many works have shown that they are the most critical in studying locomotion ([5], [6]). Indeed, ankle dorsiflexion is a critical component of the gait cycle: The ankle dorsiflexes at heel strike upon initiation of the stance phase and throughout the swing phase. For these reasons, ankle dorsiflexion/plantarflexion has been proposed as a functional magnetic resonance imaging (fMRI) paradigm for defining brain activity relevant to gait; its validity has recently been demonstrated by some experimental works showing that foot extension and flexion alone generate a similar brain activation pattern to that associated with walking ([7], [8]). In [8] foot movement has been studied by limiting it to a single degree of freedom movement (only ankle dorsiflexion/ plantarflexion) thanks to a wooden device. This latter is manually activated by an operator and may be adjusted to fit different sizes and resistance so to permit a comfortable movement. Similar experiences are presented in [9] and [10], and [11].

[12] presents a fMRI compatible device for measuring torques generated from patients during voluntary isometric lower limb contractions. The device employs the same load cell described in [1], by placing it on a footplate that is positioned so to minimize head movements.

This article illustrates a MR compatible robotic device for active and passive ankle movement. Furthermore device validation on a healthy voluntary subject is presented.

The device here described stems from the requirement of better assessing cerebral changes following a rehabilitative locomotor program recently designed by our research group, which makes use of a robotic gait orthosis ([13], [14]). Literature presents several robots for gait rehabilitation (for a

review see [15]). Pre- and post- locomotor training fMRI testing will occur on patients, thus there is the necessity of a robotic device which consents identical testing conditions. Testing protocol demands both “active” (voluntary) and “passive” (imposed) foot movement, hence a novel device was necessary.

The apparatus consents either to induce appropriate ankle plantarflexion/ dorsiflexion in one or both feet or to record angles and forces while the patient achieves the same movement. It is entirely MR compatible.

2 METHODS

2.1 DESIGN CRITERIA

Design criteria are many and stem from different necessities: these are mainly physiological and anthropometric requirements, experimental protocol constraints and need of MR compatibility.

Physiology imposes induced movement to follow certain angular laws in time. Furthermore angles may not become larger than physiological ones for safety reasons: maximum dorsiflexion must be stopped at 25° and plantarflexion at 35°. Physiological ankle joint must always be corresponding to device joint: for this anthropometric data have been studied to adapt foot position for patients between 95 percentile man and 5 percentile woman (data from [16]).

Experimental protocol requires two different kinds of modes: “active patient mode”, where device only records data from patient voluntary movement without creating disturbs, and “passive patient mode”, where device imposes appropriate movement. Complete dorsiflexion/plantarflexion cycles should occur with a frequency of circa 0.5 Hz for 12s followed by 12s of rest for the chosen testing time.

Finally real-time monitoring during fMRI testing entails MR compatibility, which brings to choice of totally amagnetic materials.

2.2 IMPLEMENTATION

Final device (picture in Fig.1a and CAD drawing in Fig. 1b) consists in a box containing regulation systems and providing support for patient’s legs, two pedals which may be coupled and a pneumatic actuator that moves pedals – and thus patient feet.

Pedals (1) may be coupled or independent by means of spins: this permits movement imposing on one or both feet, as protocol requires. Patient feet are strapped to the pedals and a small cushion positioned on contact point provides better comfort. A T-bar (2) connects pedals to pneumatic actuator (3) if pins are inserted: as cylinder moves also pedals rotate

around joint axis and the angle range may be limited by properly positioning pins in two appropriately drilled angular sectors (4). Current foot – or feet – angular position is measured by a custom-built analogue optical encoder (5): a parallelogram structure connects the rotor component to the T-bar (2). Recorded signal is transmitted to electronics positioned outside MR room by means of optical fiber. Box (6) contains height regulation system as well as providing support for patient legs: during use a proper padding furthermore covers it.

Chosen materials are aluminium, bronze, brass and Derlin. In particular bearings are Teflon coated brass L-shape bearings and all parts which require low friction contact couple Derlin and aluminium components.

Fig. 2 depicts main necessary anthropometric adaptations. Device must be suitable to patients with different sex, height and weight but patient ankle joint must always be corresponding to device joint. Distance (h) should therefore vary between 50 and 70 mm and (l) between 70 and 90 mm for adaptation to patients from 95-percentile man to 5-percentile woman. Moreover maximum angles are 25° in dorsiflexion (α_d) and 35° in plantarflexion (α_p). Contact surface – and thus force exchange - between foot and pedal corresponds to padding: its position (d) should also vary between 100 and 150 mm.

Each adaptation occurs thanks to a proper component. Distance (d) changes by means of a slot (Fig. 3a) where screws holding padding may move.

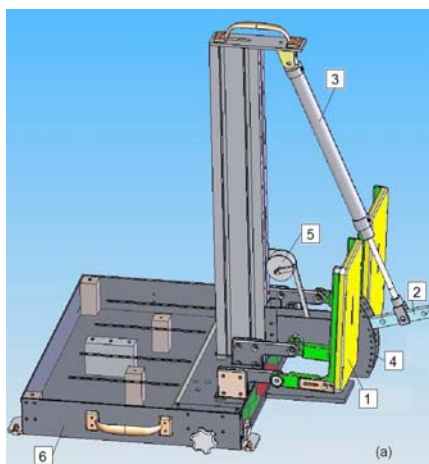


Figure 1 Device CAD drawing with numbered components (a) and picture with paddings and straps (b).

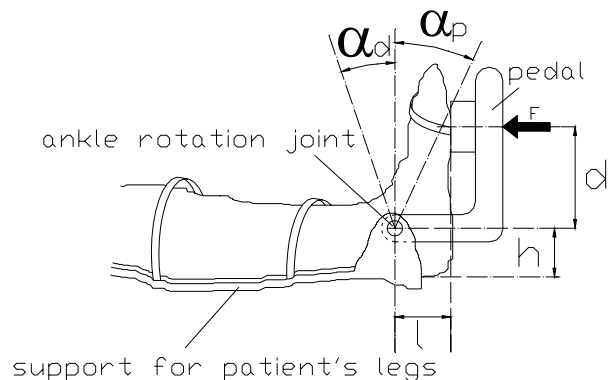


Figure 2 Main anthropometric regulation requirements.

Horizontal coincidence between patient ankle joint and device joint is obtained by means of slots (Fig. 3b) where pedal distance (l) from joint changes. In order to achieve vertical coincidence between joints (distance (h)), operator manually activates a lead screw, which drives a regulation system of overlaid Derlin wedges (Fig. 4).

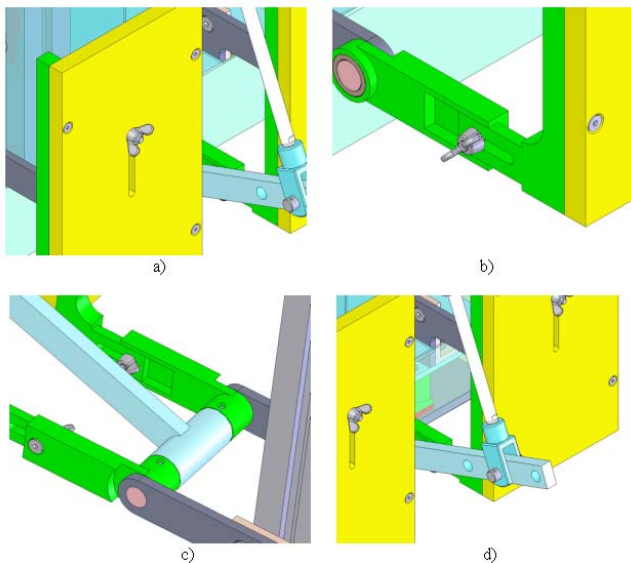


Figure 3 Main device regulations: foot padding position (a), horizontal ankle joint position (b), coupling of one or both feet with T-bar (c), position of actuator constraint for obtaining different torques (d).

Wedges (1) are hidden inside box (2), under patient leg support. Upper wedges are connected to whole pedal-actuation system (3) whereas lower wedges are fixed on a Derlin sled (4), which is brought in horizontal motion by a lead screw system. Latter system consists of female screw (5), connected to sled, and screw (7) connected to a knob (6) for operator activation. When knob (6) is rotated, screw (7) rotates and female screw (5) translates horizontally, driving connected sled (4) and lower wedges. Thanks to proper Derlin lateral slides (8), upper wedge movement is guided and thus whole pedal and actuation system (3) moves vertically.

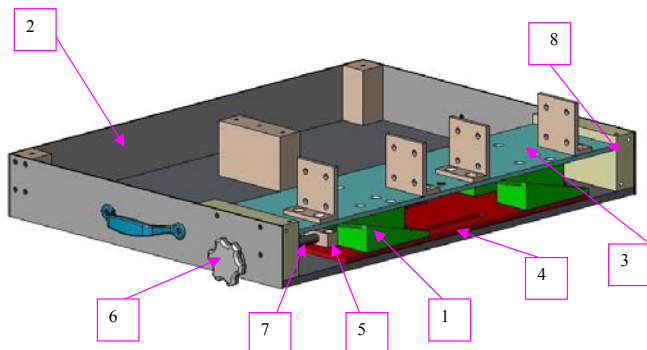


Figure 4 Lead screw and wedge system for regulating vertical ankle joint position.

Furthermore it is possible to choose between single foot movement and two feet movement by placing or removing pins (Fig. 3c) which couple pedals to the T-bar.

Finally the lever arm of transmitted force – thus the generated torque – may vary by differently attaching actuator rod on T-bar thanks to proper holes (Fig. 3d).

Kinematical analysis of pedal system was necessary to choose best constraint positions for mechanism components. In particular the position of the pneumatic actuator is strictly correlated to the force arm and thus to the generated torque. Fig. 5 depicts final kinematical scheme.

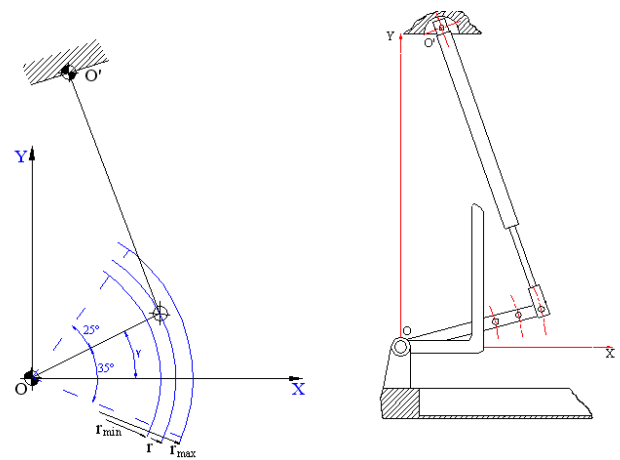


Figure 5 Kinematic scheme.

T-bar is rotated (angle γ) by 20° with respect to horizontal when ankle is in null flexion position: this consents whole range of dorsiflexion/plantarflexion motion without need of free space under the device. This choice consents to place the apparatus directly on the bed where patient lays inside MR room, without requiring other supports (e.g. a table or cart). The position of upper cylinder constraint (O') has been consequently chosen to keep generated torque as constant as possible both during motion and despite different actuator positions on T-bar.

Fig. 6 shows a picture of the prototype worn by a healthy volunteer subject during fMRI testing.

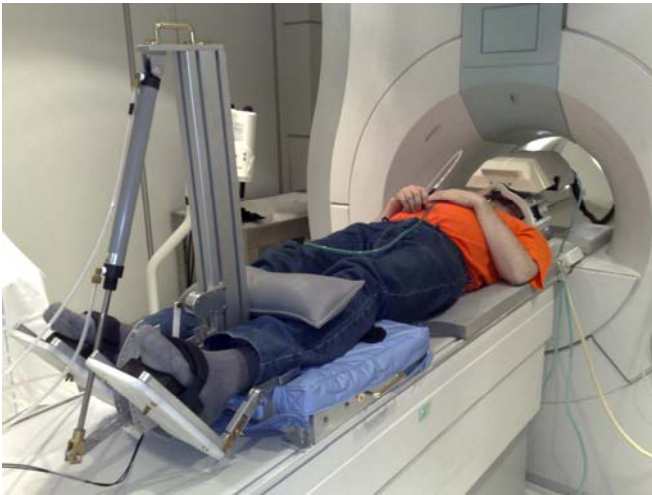


Figure 6 fMRI testing on voluntary healthy subject with MR compatible device.

3 PNEUMATIC CIRCUIT

A pneumatic circuit (Fig.7), positioned outside from MR room, controls the device.

The circuit consists of three main parts: “passive mode” circuit, “active mode” circuit, and “emergency management” circuit.

Air from supply source passes through a filter (1) and a locked pressure reducer (2) that cuts pressure to 4 bars: it then splits (node N) and flows to the three “sub-circuits”.

3.1 “PASSIVE MODE” CIRCUIT

In “passive mode” the device must impose the movement to the patient’s foot. Air from (N) passes through a pneumatically controlled bistable valve (3): if valve (3) is switched by a signal from emergency circuit, it cuts supply out and discharges the air from the circuit. Supply pressure is measured at valve (3) outlet for self-diagnostics of the system by means of pressure transducer T1. While this mode is selected from PC, electrovalve (4) is active. Air enters

through OR valve (7) and reaches electrovalves (8) and (9), connected to the MR compatible cylinder (10) chambers and alternatively activated by the control software. Air pressure is measured by means of T2 and T3, so to calculate the force imposed on patient’s feet. Outlet air from valves (8) and (9) passes respectively through flow regulators (11) and (12) before exhausting, so to allow actuator velocity control.

3.2 “ACTIVE MODE” CIRCUIT

In “active mode” the device must let the patient free to voluntarily achieve foot movement without feeling resistance. Air from (N) passes through another pressure reducer (5) which establishes pressure to the necessary value for balancing device weight. While this mode is selected from PC, electrovalve (6) is active and air passes through OR (7), since valve (4) is inactive. The downstream circuit is the same as above, although in this case valve (9) is always active and valve (8) is always inactive.

3.3 “EMERGENCY MANAGEMENT” CIRCUIT

For safety reasons, circuit presents redundant emergency buttons, which cut supply, stop the machine and discharge the circuit. OR valves (15) and (17) put all emergency signals together and command the pneumatically switched main emergency valve (3), which cuts air and discharges the circuit. Emergency signal may come: from the patient (inside MR room) by means of a bellow (B), placed in patient’s hand, which – if pushed - sends low pressure signal to low-high pressure valve (16), supplied by air coming from (N); from operator (outside MR room) by means of PC emergency button (always displayed on screen) which commands electrovalve (13) or by means of plunger activated valve (14), positioned on operator’s panel. Working conditions may be restored only manually by means of push button valve (18): this brings valve (3) back to its normal position and newly connects air from (N) to the circuit. Valve (18) can not switch valve (3) if any emergency signal is still running.

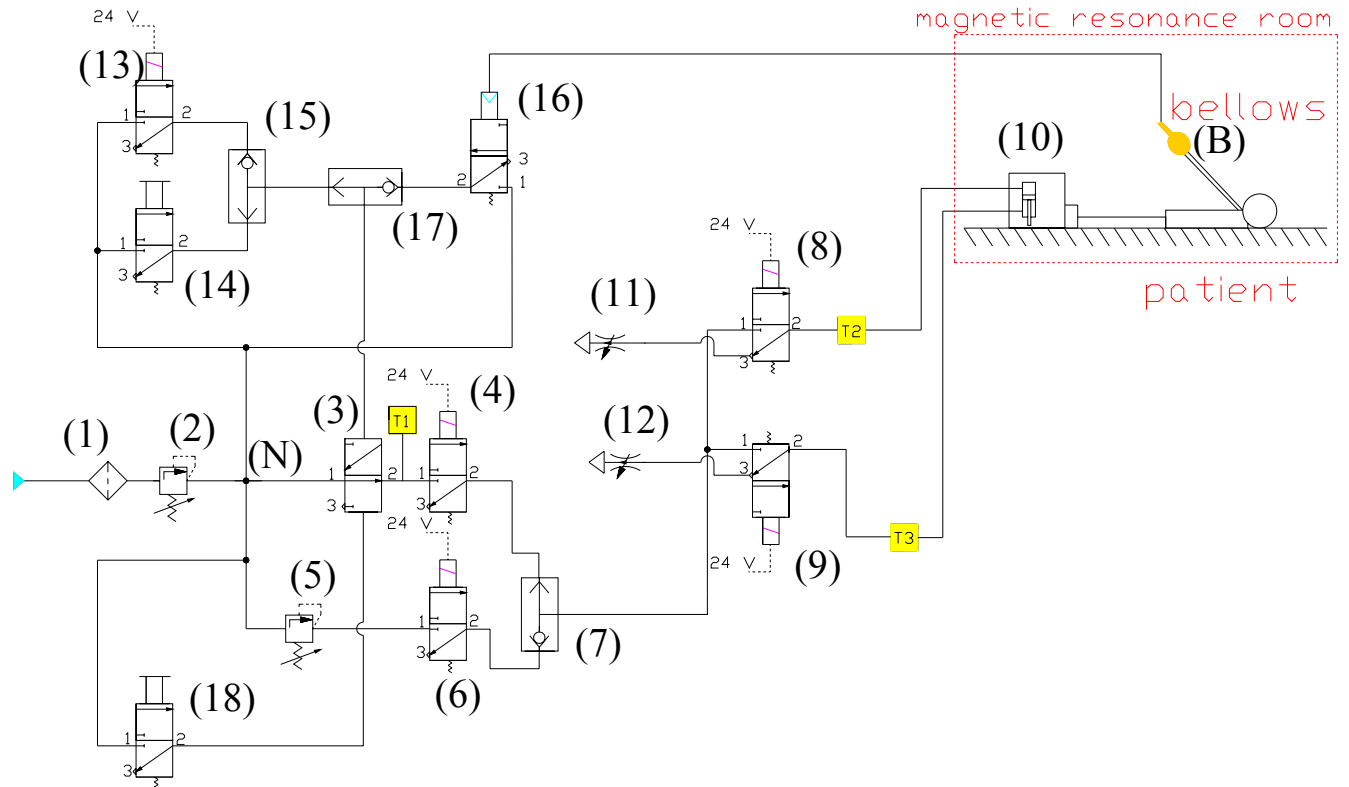


Figure 7 Pneumatic circuit schematics.

4 SOFTWARE AND CONTROL STRATEGY

Control software was expressly developed for this application. Main issues were user-friendly interface and intrinsic safety, so to avoid unwanted device movements. Fig. 8 depicts main software logic by means of a flowchart.

At the start, software makes a general test of the whole system (auto-diagnosis block): in particular it verifies signals from pressure transducers and from the optical encoder. When self-diagnostics is complete, the first screen-page is displayed, where operator can choose between “device regulations” and “testing”.

For safety reasons, operator is initially forced to choose “device regulations” option: this assures that foot movement parameters are well suited to the patient. Operator can manually adjust dorsiflexion and plantarflexion speeds (by means of flow regulators (11) and (12) in Fig. 7) as well as maximum consented angles (by appropriately positioning spins (5) in Fig. 1): software displays current settings when parameter button is pressed. This regulation is also useful for optical potentiometer sensor testing.

Only after regulation has occurred operator may enter “testing” and select between “active patient” mode or

“passive patient” mode.

In “passive patient” mode operator can change movement frequency and cycling time from the default values defined by standard protocol. Patient name must be inserted for data saving during testing.

During both “active patient” and “passive patient” modes, screen displays angular displacement, angular speed and exchanged force. Operator may save all records as data arrays versus time with the chosen name. Furthermore emergency button is always displayed during testing: this permits operator to cut supply pressure and discharge the circuit at any moment.

5 fMRI SUBJECT AND METHODS

A voluntary healthy subject was scanned while performing an active and passive blocked motor paradigm using described device. Paradigm was 12s of plantarflexion/dorsiflexion with frequency 0.5 Hz followed by 12s of rest for total acquisition time lasting 6.6 minutes.

Data acquisition was performed on a 1.5 Tesla INTERA™ scanner (Philips Medical Systems) with a SENSE high-field,

high resolution (MRIDC) head coil optimized for functional imaging. The resting state functional T2-weighted images were acquired using echoplanar (EPI) sequences, with a repetition time (TR) of 2000 ms, an echo time (TE) of 50 ms and a 90° flip angle. The acquisition matrix was 64 x 64, the field of view (FoV) 200 mm. A total of 200 volumes were acquired; each volume consisted of 19 axial slices, parallel to the anterior-posterior (AC-PC) commissure line; the slice thickness was 4.5 mm with a 0.5 mm gap. Two scans were added at the beginning of functional scanning and the data discarded to reach a steady-state magnetization before acquiring the experimental data.

In the same session, a set of three-dimensional high-resolution T1-weighted structural images was acquired for each participant. This data set was acquired using a Fast Field Echo (FFE) sequence, with a repetition time (TR) of 25 ms, ultra-short echo time (TE) and a 30° flip angle. The acquisition matrix was 256 x 256, the field of view (FoV) 256 mm. The set consisted of 160 contiguous sagittal images covering the whole brain. The in-plane resolution was 1 x 1 mm and slice thickness 1 mm (1 x 1 x 1 mm voxels).

BOLD imaging data were analyzed using the Brain Voyager QX software (Brain Innovation, Maastricht, Holland); a plug-in extension of this software was used to compute blind source deconvolution and power spectrum IC analyses (ICA plug-in) which corresponded to a C++ implementation of the fast-ICA algorithm ([17]). Functional data underwent the following pre-processing steps: 1) slice scan time correction, using a sinc interpolation algorithm; 2) 3D motion correction: all volumes were aligned spatially to the first volume by rigid body transformations, using a trilinear interpolation algorithm; 3) spatial smoothing by using a Gaussian kernel of 4 mm FWHM; 4) temporal filters (i.e. linear trend removal and non-linear trend removal using a temporal high-pass filter [frequency pass = 0.008 Hz]) were applied to remove drifts due to scanner and other low frequency noises 5) low-pass temporal filtering (FWHM = 2.8 s) to achieve modest temporal smoothing.

After preprocessing, a series of steps were followed in order to allow for precise anatomical location of brain activity. First, slice-based functional scan was co-registered on his own 3D high-resolution structural scan. Second, the 3D structural data-set of was transformed into Talairach space. Third the functional time course of each run was transformed into Talairach space and the volume time course created.

To circumvent the influence of movement artefacts functional images were measured by independent component analysis (ICA), a statistical technique that separates a set of signals into independent uncorrelated and non-Gaussian spatio-temporal components (IC). The fMRI brain image at each time point is treated as a mixture of spatial independent

components; sICA extracts the different components, each with its unique time course, maximizing their spatial statistical independence. Fig.8 shows the flowchart of the prototype control software.

6 DISCUSSION

6.1 DEVICE PERFORMANCE

Fig. 9 depicts theoretical torques generated by the device with a 25mm bore pneumatic cylinder during plantar- and dorsi-flexion. The different curves depend on the distance (r) between the cylinder rod and the ankle joint (i.e. the radius of the force).

Torque values may vary by changing supply pressure and/or cylinder bore: equivalent force imposed to the foot may consequently vary between 20 and 500N.

Real exchanged forces depend on patient interaction: however pneumatic actuation has been chosen also for its intrinsic compliance, which assures that forces stay under certain imposed values. This is a main issue for safety.

Device can be regulated to adapt joint position to physiological ankle joint for patients between 95-percentile man and 5-percentile woman. Angular displacement reaches maximum values of 25° in dorsiflexion and 35° in plantarflexion: these may be mechanically reduced by means of pins.

Experimental tests gave good results for what regards MR compatibility: chosen materials do not disturb testing magnetic field.

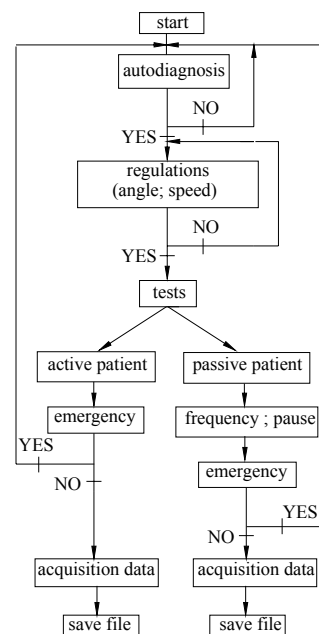


Figure 8 Control software main flowchart

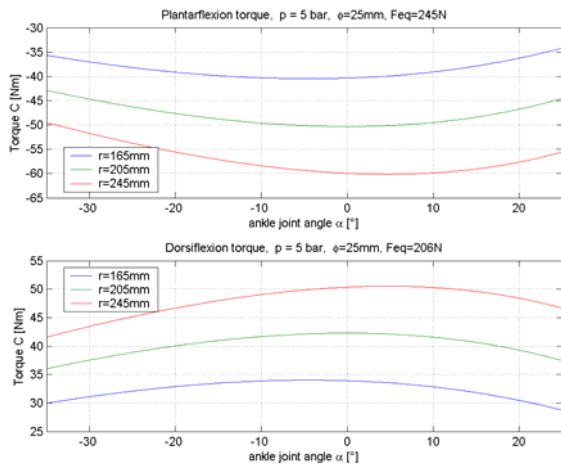


Figure 9 Theoretical torques imposed by pneumatic actuator during ankle range of motion for different values of force lever arm (r).

6.2 fMRI PRELIMINARY RESULTS

We extracted 40 IC with the ICA plugin and correlated each IC timecourse with the stimulation protocol and the 6 motion parameters resulting from the 3D motion correction algorithm. For each paradigm, the four IC found to be more correlated with the stimulation protocol (Fig. 10) and those more correlated with motion parameters (Fig 11) were mapped. The passive stimulation-related IC (Fig. 10), although in some measure affected by motion noise, shows as expected a robust sensorymotor, supplementary motor and cerebellar activity plus some temporal and parietal clusters. The mean M1 timecourse shows that the activity in this area is strongly correlated with the stimulation paradigm.

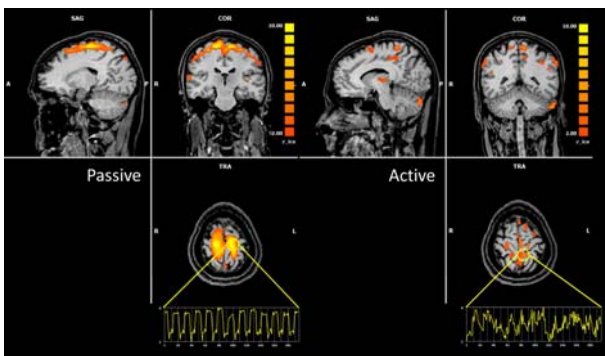


Figure 10 ICA motor components relative to Active (left) and passive (right) stimulation. Boxplots show the mean timecourse of a circular roi placed in the activated left sensorymotor area. Z-ica scale, Images obtained with Brainvoyager QX 1.9.

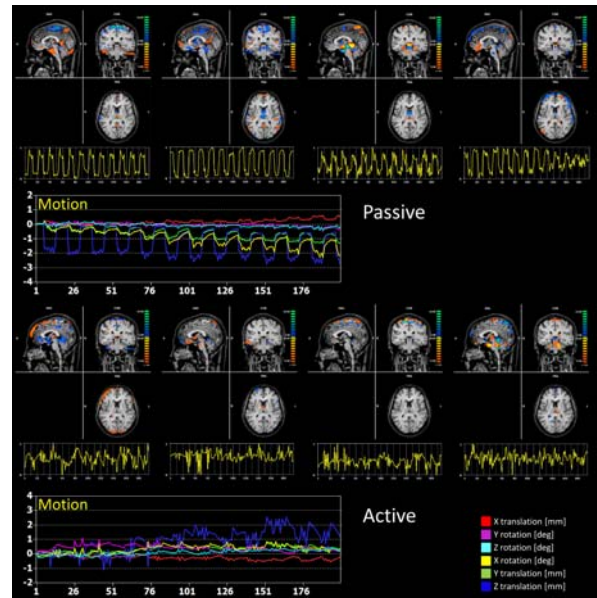


Figure 11 ICA most movement-related noise components relative to passive (upper images) and active (lower images) stimulation. Boxplots show the mean component timecourse and the six parameters motion of the subject head. Z-ica scale, Images obtained with Brainvoyager QX 1.9.

The active stimulation-related IC (Fig. 10) is less affected by motion noise and shows a less robust sensorymotor and supplementary motor activity, a cerebellar activation plus some thalamic, frontal and cingulate clusters. The mean M1 timecourse shows that the activity in this area is less correlated with the stimulation paradigm as well as with motion parameters.

The power analysis of motion-related ICs (Fig. 11) shows that the passive movement can induce stronger motion-related artefacts in the fMRI images than the active one. This is proved by the mean RMS signal that is significantly higher in the passive motion noise IC timecourses than in the active ones (Two sample t-Test, $P=0.022$ uncorrected).

The visual inspection of the motion graphs confirms that the passive movement induces a severe cumulative as well as periodic translation on the Z-axis and a similar rotation on the X-axis.

7 CONCLUSION

MR compatible device for active and passive foot movement has been developed and tested in MR environment and on a volunteer healthy subject. Device is entirely MR compatible and also optical angular encoder gave good compatibility

results. Device achieves imposing required movements and recording voluntary patient movements without interfering. Better fixing patient's head may certainly reduce the recorded movement artefact in the fMRI brain activation due to subject translation and a rotation. Literature [12] presents an interesting solution where patient leg is bent. In such configuration it is likely that most of the z-axis translation of patient – and consequently of his head - is absorbed by leg movement instead, which would not generate such signal disturbs.

The main use of the device is in the fMRI assessment of motor rehabilitation efficacy, as it requires precise and controlled tasks in order to create identical pre- and post-treatment conditions and, with some patients, at least a partial help in performing the movement. However, given its RM compatibility, the device can actually be applied in every fMRI examination where either the patient cannot autonomously move his feet, or the control and standardization of movement parameter are essential (e.g. in research contexts). For instance, another relevant clinical fMRI application concerns the pre-surgical localization of eloquent brain areas, i.e. identify where motor and linguistic functions are placed in the patient's brain. Some patients requiring a brain surgery have difficulty in executing an fMRI foot motor task because of their tumor; on the other hand, a precise localization of their cerebral motor function is crucial for pre-surgical planning. Here again, a robotic device inducing passive foot movement becomes of great help. Finally, in research laboratories, fMRI is used to understand the workings of the normal human brain, including sensory and motor functions. In group studies, standardization of task parameters within participants is required. In repeated study designs, a robotic device provides the possibility of studying the effect of different controlled parameters on cerebral activations.

Besides its primary use in fMRI testing, presented device can be fruitfully applied in the rehabilitation of neurological paretic patients, who need to practise foot movements and/or to relearn locomotor schemas. Indeed, given that foot dorsiflexion/plantarflexion is crucial in deambulation, locomotor rehabilitation protocols have started to include specific foot movement exercises (e.g., [18]). The active/passive modes of the device allow its use in various types of motor therapies. For example, within Active Movement Training therapies (AMT), the 'active patient mode' allows the practice of the dorsi/plantar-flexion exercises; the possibility of setting the 'passive patient mode' at different degrees (according to the patient's motor capabilities) allows to include also patients with scarce motor functions, previously excluded from this type of therapy, who can gradually pass from the passive to the active mode on the

bases of their ongoing motor improvements. Within Constrained-Induced therapies, the healthy foot can be immobilized with the device, while exercising the paretic foot. In the context of Passive Movement Training therapies, the passive movement of the plegic foot is helpful for the proprioceptive inputs to motor cerebral networks ([19]). In the context of recent Motor Imagery rehabilitation protocols, the passive foot movement can be accompanied by cognitive exercises with a locomotor attention focus.

The fundamental advantage is that the same device can be used both inside and outside the RM scanner, thus allowing to directly correlating patient's progresses in rehabilitation with his cerebral functional changes.

ACKNOWLEDGMENT

This work was supported in part by the "Compagnia di San Paolo" on the project "Active exoskeleton for functional gait rehabilitation in paretic patients" and in part by the Piedmont Region project entitled "Validation of a gait rehabilitation method for paretic patients with the aid of an active orthosis". Authors would like to thank Prof. G. Geminiani, from the Department of Psychology of the "Università di Torino", A. Nascimbeni from "S. Croce" Hospital of Moncalieri, S. Duca from "Koelliker" Hospital of Torino, Prof. M. Zettin from "Cooperativa Sociale Puzzle" of Torino and Eng. L. Gribaldi.

REFERENCES

- [1] Hidler J., Mbwana J., and Zeffiro T. "MRI compatible force sensing system for real-time monitoring of wrist moments during fMRI testing", Presented at the 9th International Conference on Rehabilitation Robotics, June-July 2005, Chicago.
- [2] Lange R., Nowak H., Hauelsen J., and Weiller C., "Passive finger movement evoked fields in magnetoencephalography" Biomagnetic Center, Department of Neurology 2000 October.
- [3] Weiller C., Juptner M., Fellows S., Rijntjes M., Leonhart G., Kiebel S., Muller S., Diener H. C., and Thilmann A. F. "Brain Representation of Active and Passive Movements", *Neuroimage* 4, 105-110, 1996.
- [4] Mima T., Sadato N., Yazawa S., Hanakawa T., Fukuyama H., Yonekura Y., and Shibasaki H. "Brain Structures related to active and passive finger movements in man" *Brain*, 122, pp. 1989-1997, 1999.
- [5] Lavoie B. A., Devanne H., Capaday C.. "Differential control of reciprocal inhibition during walking versus postural and voluntary motor tasks in humans". *J Neurophysiol* 78: 429-438. 1997.
- [6] Capaday C., Lavoie B.A., Barbeau H., Schneider C., Bonnard M.. "Studies on the corticospinal control of human walking. I. Responses to focal transcranial

- magnetic stimulation of the motor cortex” *J Neurophysiol.* 81: 129-139, 1999.
- [7] Dobkin B. H., Firestine A., West M., Saremi K., and Woods R. “Ankle dorsiflexion as an fMRI paradigm to assay motor control for walking during rehabilitation” *NeuroImage* Elsevier Inc. 23, 2004, pp. 370-381.
- [8] Sahyoun C., Floyer-Lea A., Jahansen-Berg H., and Matthews P.M. “Towards an understanding of gait control: brain activation during the anticipation, preparation and execution of foot movements”, *NeuroImage*, Elsevier Inc., 21, 2004, pp. 568-575.
- [9] Ciccarelli O., Toosy A.T., Marsden J.F., Wheeler-Kingshott C.M., Sahyoun C., Matthews P.M., Miller D.H., Thompson A.J., “Identifying brain regions for integrative sensorimotor processing with ankle movements”. *Exp. Brain Res.* 166, 31–42, 2005.
- [10] Christensen M.S., Lundbye-Jensen J., Petersen N., Geertsen S.S., Paulson O.B., Nielsen J.B. “Watching your foot move—an fMRI study of visuomotor interactions during foot movement”. *Cereb. Cortex.* 17 (8), 1906–1917, 2006.
- [11] Kapreli E., Athanasopoulos S., Papathanasiou M., Van Hecke P., Strimpakos N., Gouliamos A., Peeters R., Sunaert S. “Lateralization of brain activity during lower limb joints movement. An fMRI study”. *Neuroimage* 32, 1709–1721, 2006.
- [12] Newton J. M. a, Dong Y., Hidler J., Plummer-D'Amato P., Marehbian J., Albistegui-DuBois R. M., Woods R. P., and Dobkin B. H. “Reliable assessment of lower limb motor representations with fMRI: Use of a novel MR compatible device for real-time monitoring of ankle, knee and hip torques” *NeuroImage*, to be published.
- [13] Belforte G., Gastaldi L., Sorli M. “Pneumatic active gait orthosis” *Mechatronics*, v 11, n 3, April 2001, p 301-23.
- [14] Belforte G.; Gastaldi L.; Sorli M. “Active orthosis for rehabilitation and passive exercise”, Proc. Of International Conference on Simulations in Biomedicine, BIOMED, 1997, pp. 199-208.
- [15] Dollar A. M. and Herr H. “Lower Extremity Exoskeletons and Active Orthoses: Challenges and State-of-the-Art” *IEEE Transactions on Robotics*, vol. 24, no. 1, Feb. 2008.
- [16] Tilley A. R. *The Measure of Man and Woman* Henry Dreyfus Associates.
- [17] Hyvärinen A., Hoyer P.O., Inki M. “Topographic independent component analysis”. *Neural Comput.* Jul;13(7):1527-58, 2001.
- [18] Jackson P.L., Doyon J., Richards C. L., and Malouin F. “The efficacy of combined physical and mental practice in the learning of a foot-sequence task after stroke: a case report”. *Neurorehabil Neural Repair.* 18: 106-111, 2004.
- [19] Nelles G., Spiekermann G., Jueptner M., Leonhardt G., Müller S., Gerhard H., Diener H.C.. “Reorganization of sensory and motor systems in hemiplegic stroke patients. A positron emission tomography study” *Stroke.* Aug;30(8):1510-6, 1999.

CALIBRATION OF ROBOT-MOUNTED LASER SCANNING PROBE BASED ON A TOOL TRANSFORMATION

Theodor Borangiu* Anamaria Dogar* Alexandru Dumitrache*

* Centre for Research & Training in Industrial Control,
Robotics and Materials Engineering, University Politehnica of Bucharest

ABSTRACT

This paper describes a method for calibrating a 3D laser scanning device mounted on the wrist of a 6-DOF robot arm, by computing a tool transformation for the laser sensor reference frame. The calibration procedure involves scanning a spherical object fixed in the robot workspace, and it makes possible aligning many individual scans taken from different orientations. Another advantage of this approach is that further applications become possible, such as using the laser sensor for accurate robot guidance and alignment.

Keywords: 3D scanning, sensor calibration, tool transformation

1 INTRODUCTION

This article presents a technique for calibrating a 2D laser profile sensor mounted on the arm of a 6-DOF robot for reconstruction of 3D models of existing parts from range data. An overview for the scanning system is presented in Figure 1. This approach will consider that the laser probe is the tool used by the robot arm, and therefore a tool transformation will be computed, so that all the contour data from the profile sensor can be expressed in the reference frame of the robot.

In a previous paper [3], there was presented a calibration method for the 7th degree of freedom of the scanning system, which is the rotary table holding the scanned part. However, it was assumed that the transformation matrix between the robot wrist and the laser probe is already known with good accuracy, which was not true in practice. This paper focuses on a method for determining the tool transformation for the laser sensor, which includes the orientation and the tool center point.

The data from the laser sensor is a set of unorganized 2D points, which can be mapped to the 3D reference frame of the laser sensor by assigning $X = 0$, $Y = x_{2d}$ and $Z = y_{2d}$.

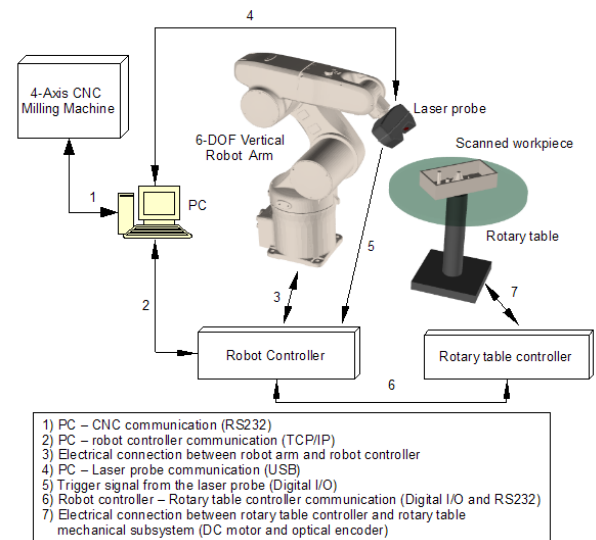


Figure 1 Overview of the laser scanning system

The scanned data has to be aligned into a common 3D reference frame, which is attached to the object of interest, and this is done using the *alignment equation*. This equation pre-multiplies the laser measurements with the following matrix equation [4]:

$$T_{align} = T_L^R = T_0^R(\theta_R) \cdot T_6^0(\theta_{1..6}) \cdot T_6^L \quad (1)$$

Contact author: Theodor Borangiu¹, Alexandru Dumitrache²

¹ E-mail: borangiu@cimr.pub.ro

² E-mail: alex@cimr.pub.ro

where T_6^0 represents the direct kinematics of the robot arm [1], T_0^R is the transform between the table and the robot, and T_L^6 (also called T_L^W) is the transform from the robot wrist to the field of view (FOV) of the sensor $X_L Y_L Z_L$ (Figure 2).

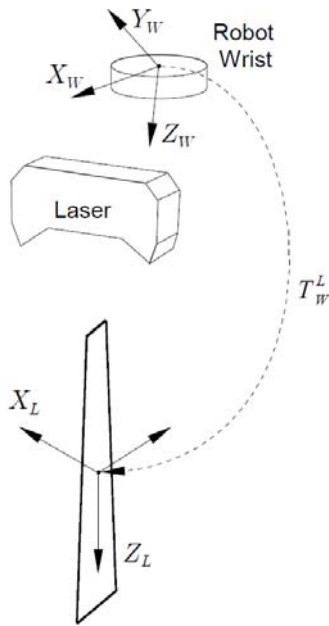


Figure 2 Tool transformation for the laser probe.

The direct kinematics function of the robot was considered ideal, and there are two transformation matrices that are determined using two calibration procedures:

- robot – laser probe calibration
- robot – rotary table calibration

The calibration between the robot and the table was presented in detail in [3], and this paper will only address the *robot – laser probe calibration*.

The software which controls the laser probe has a calibration routine for the linear stages of the scanning system (X , Y and Z), which is performed using a tooling ball placed in the workspace, in a fixed, but not precisely known position. The laser sensor is translated over the tooling ball, scanning with a sweeping motion. The acquired data is then fitted to a sphere, and its center is computed and used for calibration. The sphere is placed in various locations in the field of view (FOV) of the laser probe; for determining the orientation of the FOV, at least 3 locations are needed. For better accuracy, a higher number of locations is used (by default 9), because the errors will be averaged, increasing the accuracy of the calibration.

Aside from the orientation, this procedure, which is named *ball matching*, computes also the parameters for internal calibration of the sensor itself, which include the offsets between the two cameras, the scaling factor and also a nonlinear (quadratic) correction for the 3D data.

This method of calibration does not compute the origin of the sensor reference frame; only its orientation is determined. However, because the implementation of this method is mature, stable and provides good results, the calibration process will not be rewritten from scratch; instead, the existing method will be reused. Therefore, the first step of the calibration will be executed using the existing ball matching method, but the calibration results will have a slightly different interpretation. A second calibration step will be necessary in order to determine the origin of the sensor, i.e. the cartesian offsets dx , dy and dz .

2 CALIBRATION EQUATIONS

The procedure for finding the TCP (tool center point) $P = (x_P; y_P; z_P)$ is presented in [9]. The user has to teach at least 3 robot locations, $L^{(1)} \dots L^{(n)}$, with $n \geq 3$, by placing the tool tip in the same physical location, with different orientations. The method will find the point whose local coordinates (in the tool reference frame) map to the same World coordinates, regardless of the arm orientation.

The point P can be mapped in the World reference frame by pre-multiplying it with the direct kinematics matrices for the taught robot locations, $L^{(1)} \dots L^{(n)}$:

$$\begin{aligned} P_W^{(1)} &= L_1 P \\ &\vdots \\ P_W^{(n)} &= L_n P \end{aligned} \quad (2)$$

Since all points $P_W^{(i)}$, $i = 1 : n$, represent the same physical location, which is unknown to the calibration routine, the conditions for finding the tool center point P become:

$$P_W^{(i)} = P_W^{(j)}, \forall i \neq j \quad (3)$$

If exactly 3 locations are taught, the point P can be computed by solving a linear system in $Ax = b$ format. Eqs. (2) and (3) will be rewritten using homogeneous transformation matrices as:

$$P_W = \begin{bmatrix} x_W \\ y_W \\ z_W \\ 1 \end{bmatrix} = \begin{bmatrix} R^{(i)} & T^{(i)} \\ 0 & 1 \end{bmatrix} \begin{bmatrix} x_P \\ y_P \\ z_P \\ 1 \end{bmatrix}, \quad i = \overline{1,3} \quad (4)$$

where $R^{(i)}$ and $T^{(i)}$ represent the rotation and translation components of the robot location $L^{(i)}$:

$$R^{(i)} = (r_{ij}), \quad i = \overline{1,3}, \quad j = \overline{1,3} \quad \text{and} \quad T^{(i)} = \begin{bmatrix} x_L^{(i)} \\ y_L^{(i)} \\ z_L^{(i)} \end{bmatrix}, \quad i = \overline{1,3} \quad (5)$$

Decomposing the rotation and translation, Eq. (4) is rewritten as:

$$P_W = \begin{bmatrix} x_W^{(i)} \\ y_W^{(i)} \\ z_W^{(i)} \end{bmatrix} = R^{(i)} \begin{bmatrix} x_P \\ y_P \\ z_P \end{bmatrix} + T^{(i)}, \quad i = \overline{1,3} \quad (6)$$

Since P_W is an unknown, but its value is not required in the calibration process, only $P = (x_P, y_P, z_P)$ will be computed. The P_W term can be removed by considering Eq. (6) for $i = 1$, from which there is subtracted the same Eq. (6), multiplied by 0.5, using $i = 2$ and $i = 3$. The result of the subtraction is:

$$\left(R^{(1)} - \frac{R^{(2)} + R^{(3)}}{2} \right) \begin{bmatrix} x_P \\ y_P \\ z_P \end{bmatrix} = - \left(T^{(1)} - \frac{T^{(2)} + T^{(3)}}{2} \right) \quad (7)$$

which is a 3×3 linear system in $Ax = b$ format.

If the calibration is performed with more than three points, Eq. (3) can be solved in a least squares sense [2], or it can be regarded as a minimization problem. A possible quadratic criteria for minimization is:

$$e = \text{var}[x_W^{(1..n)}] + \text{var}[y_W^{(1..n)}] + \text{var}[z_W^{(1..n)}] \quad (8)$$

where $\text{var}(a)$ is the variance of a :

$$\text{var}[a^{(1..n)}] = \sum_{i=1}^n [a^{(i)} - a_m]^2 \quad (9)$$

and a_m is the arithmetic mean of a .

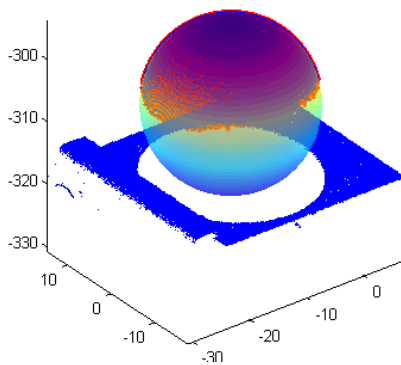


Figure 3 Sphere identification and fitting from 3D point cloud data.

For the laser calibration problem, the $n \geq 3$ robot locations are also taught using the ball matching method. If the ball is in the field of view, it will be seen as a circle having the radius less than or equal to the real radius R of the ball, and the circle will be in the YZ plane of the tool coordinate system. The center of the circle in YZ can be determined easily, but the X coordinate is not known, since the laser

plane does not intersect the center of the ball. The ball matching method will perform a sweep on the X direction of the tool reference frame, from $-R$ to $+R$ with respect to the current position, and from the 3D point cloud acquired, the center of the ball can be computed by a sphere fitting procedure (Figure 3).

The sphere is fitted using the Riemann method, by projecting the data points on a 4D paraboloid, the result being a hyperplane. A similar method was presented in [7] for fitting a circle, and it was straightforward to extend the method for fitting the sphere. This method is advantageous because the hyperplane fitting problem is linear, and can be solved by well-known robust fitting methods based on weighted least squares [8]. The robust fitting method is iterative and slower than the classical least squares fitting technique, but the results (center and radius) are not affected by outliers in the input data.

3 SIMULATION RESULTS

The method for computing the tool center point from three or more robot locations taught with different orientations was simulated using ideal data affected by random Gaussian noise, employing a Monte Carlo approach for determining the standard deviation of the estimation errors. The first test used three simulated robot locations, the first one being vertical and downlooking, the second being rotated around X with an angle α , and the third one rotated around Y with the same angle α . The position of the three taught locations was altered with a Gaussian noise on each axis, having a standard deviation of $\sigma = 0.1 \text{ mm}$, zero mean and zero cross-correlation. The orientation of the locations was not altered.

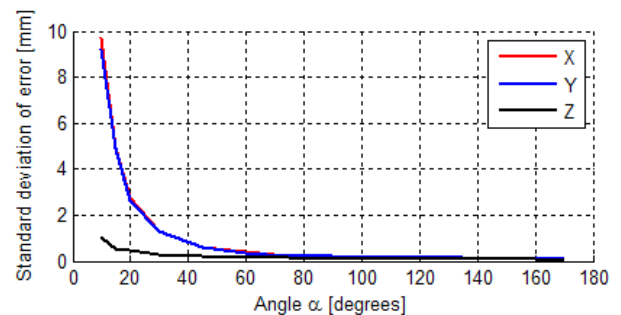


Figure 4 Estimated standard deviation of the translation errors in the tool transformation, for the three axes.

The error function was considered the difference between the ideal and estimated position of the Tool transformation. The ideal position was chosen $(60, 10, 200)$, which is very close to the actual (physical) position. Using the Monte Carlo approach, for each constant value of α , 200 tests were performed, from which the standard deviation of the error was estimated for each axis (X , Y and Z).

The conclusion from this simulation is that the angle between the Z axes of any two robot locations used for calibration has to be greater than 45° , if only 3 points are

used, since for lower values the accuracy decreases rapidly, and for higher values there are no significant gains.

Also, the error is biased, so the position on the Z axis has the least standard deviation. Further experiments revealed that the bias is heavily dependent on the set of orientations used for calibration, so a balanced solution should include more than 3 points, which cover the entire range of orientations which will be used in the application.

4 EXPERIMENTAL RESULTS

The calibration routine has been successfully implemented on the scanning system, and it allows scanning the parts with any orientation of the laser sensor that can be achieved physically with the mechanical setup. The scanning procedure can be completed in two modes:

- The laser probe follows a complex 3D path, changing simultaneously the position and orientation.
- The laser probe follows a sequence of simple linear sweep motions (scan passes), keeping its orientation constant. The orientation is changed before beginning the next scan pass.

While the second approach is simpler to implement, the first method is more elegant, but also more complex, and it requires a very high absolute accuracy for the mechanical subsystem that moves the laser sensor. Since in the current setup a vertical robot arm was used, and its kinematic structure has only rotary joints, the transformation to Cartesian space is performed using the direct and inverse kinematics routines. These are nonlinear functions, and may introduce nonlinear errors if the physical kinematic model of the robot has slightly different parameters with respect to the nominal (ideal) values, and the calibration method presented in this paper does not account for nonlinearities. Therefore, it is expected that the calibration method will be better suited to a Cartesian mechanical structure, such as a coordinate measurement machine (CMM) with a 3-DOF spherical wrist.

The best results were obtained using the second approach, with many scan passes, each pass maintaining constant orientation. The result of every scan pass is a point cloud, and the point clouds obtained from all the scan passes are already almost aligned, with very small differences, i.e. up to 0.5 mm distance between two overlapping surfaces. These differences are corrected using the Iterative Closest Point (ICP) algorithm, and the method was successfully tested using the open-source mesh processing software MeshLab [6]. An example of reconstruction of a small decorative object is presented in Figure 5.

While it is true that the alignment of individual meshes is still not perfect, it provides a good initialization for the ICP algorithm, very close to the optimal result, and the user is not required to manually align the meshes before executing the automatic alignment procedure.

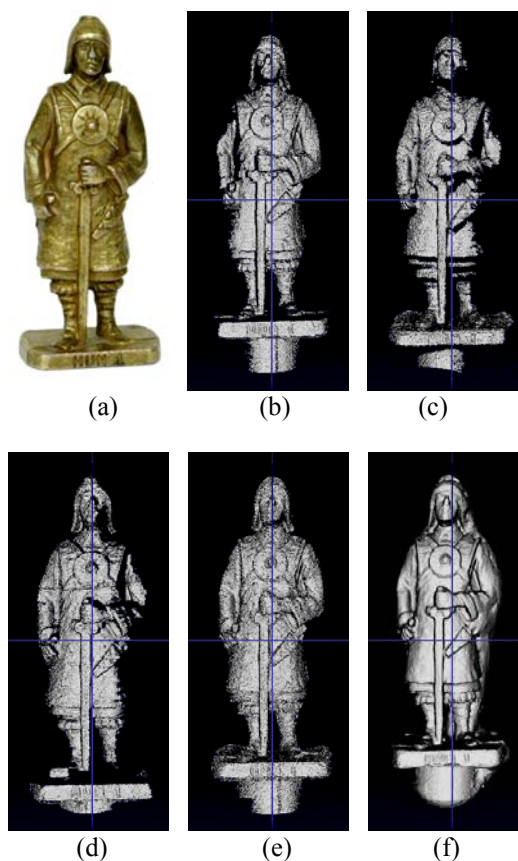


Figure 5 Reconstruction of a decorative object
 (a) - photography;
 (b), (c), (d) – scans from different orientations;
 (e) – the scans merged into a single mesh;
 (f) – 3D surface model created using the Poisson filter in MeshLab.

5 OTHER USES FOR THE CALIBRATION METHOD

The calibration method presented in this paper has a much wider applicability in other tasks, different from 3D reconstruction using the laser scanner. For example, the laser probe can be used as a highly accurate distance sensor, which can be used for delicate tasks such as manipulating very small parts, or as a tool for teaching robot locations with high accuracy.

The simplest application is learning a reference frame for a tilted plane on which the robot has to work. Instead of manually teaching at least 3 robot locations on the tilted plane, the laser sensor can be used as a distance sensor in order to teach the location with an automatic procedure.

A more complex application involves 3D path following around a given workpiece, when the 3D data is not available. The 3D path is defined along an edge of the part (e.g. Figure 6), which can be identified by the laser sensor. The robot has to move a tool along the edge of the art in order to perform various technological operations, such as sealant dispensing, edge deburring, or welding.

After the user teaches the edge model into the vision software, the robot uses the laser sensor in order to automatically identify the 3D path, adjusting its position and orientation, and learning the trajectory with a resolution specified by the user, e.g. 1 mm. After the trajectory is learned, since the tool transformation for the sensor is known, the locations are expressed in the robot's reference frame. Therefore, the robot can use the tool specific to the technological operation needed, change the tool transformation matrix to the one for the physical tool, and replay the learned path with high accuracy.

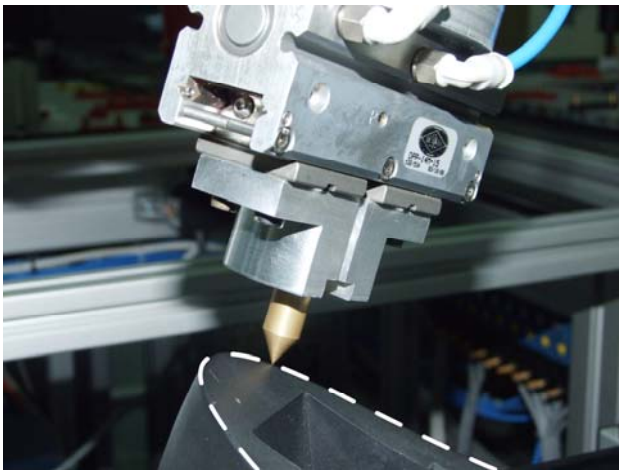


Figure 6 Sample 3D path following problem.

The 3D contour learning and following application is presented in detail in [5].

6 CONCLUSIONS

This article presented a calibration method for a wrist-mounted laser scanning probe, which is able to reconstruct 3D surfaces of existing objects by having a 6-DOF robot arm move the probe around the objects with different orientations. The method computes a tool transformation which moves the tool center point of the robot in the origin of the laser's field of view and aligns the axes of the wrist reference frame to the ones of the laser sensor, thus making possible for the data from the laser scanner to be expressed in the robot reference frame only by pre-multiplying it with the direct kinematics of the robot at the moment of the data acquisition.

Having the tool center point in the origin of the reference frame, the position of the laser sensor in the workspace is also much easier to control, since the user can move the probe on its own axis, i.e. X is normal to the laser plane, and $Y-Z$ define the laser plane, with positive Z approaching the scanned part. The rotations of the probe around the part can be performed either around the center of the laser's field of view, or around any point defined by the user, for example, the "center" of the data visible in the sensor. This is a significant improvement to the usability of the scanning

system, since the scanned part will remain visible while rotating the probe around it.

Further applications with the laser sensor are possible using the tool transformation defined. For example, since the laser sensor can measure distances with very high accuracy (tens of micrometers or even micrometers for very short range devices), the sensor can be used for robot guidance in order to manipulate very small parts and to perform precise operations. Another possibility is to use the laser sensor for guiding the robot along a visible edge of an existing part, in order to learn and follow a complex 3D path, even if a CAD model for the part is not available.

ACKNOWLEDGEMENTS

This work is funded by the National University Research Council, in the framework of the National Plan for Research, Development and Innovation.

The 3D data was postprocessed using MeshLab, an open-source tool developed by the VCG group with the support of the Epoch NOE.

REFERENCES

- [1] Spong, M.W., Hutchinson, S. and Vidyasagar, M., *Robot Modelling and Control*, John Wiley, 2005, ISBN: 978-0-471-64990-8.
- [2] Dumitrescu, B, Popeea C., Jora B., *Numerical Methods for Matrix Computation. Fundamental Algorithms*, ALL, Bucharest, 2006.
- [3] Borangiu, Th., Dogar, A. and Dumitrache, A., Integrating a Short Range Laser Probe with a 6-DOF Vertical Robot Arm and a Rotary Table, *Proceedings of RAAD 2008*, Ancona, Italy.
- [4] Borangiu, Th., Dogar, A. and Dumitrache, A., Modelling and Simulation of Short Range 3D Triangulation-Based Laser Scanning System, *Proceedings of ICCCC'08*, Oradea, Romania, 2008.
- [5] Borangiu, Th., Dogar, A. and Dumitrache, A., Flexible 3D Trajectory Teaching and Following for Various Robotic Applications, *Proceedings of SYROCO 2009*, Gifu, Japan.
- [6] Cignoni, Paolo et. al., MeshLab: an Open-Source Mesh Processing Tool, *Sixth Eurographics Italian Chapter Conference*, pp. 129-136, 2008
- [7] Frühwirth R, Strandlie A et.al.. A review of fast circle and helix fitting. *Nuclear Instruments and Methods in Physics Research*, vol. A 502, pp. 705-707, 2003.
- [8] Fox, J. Robust Regression. in *An R and S-PLUS Companion to Applied Regression*, Sage Publications, 2002.
- [9] Hallenberg, J., *Robot Tool Center Point Calibration using Computer Vision*. Master Thesis, Electrical Engineering Dept., Linköping University, Sweden, 2007.

A LUNAR ROVER LEG: OPTIMAL DESIGN OF A DECOUPLING JOINT

Rita Ambu

Costantino Falchi

Andrea Manuello Bertetto

Department of Mechanical Engineering, University of Cagliari, Italy

ABSTRACT

The development of vehicles for the exploration in the lunar environment is a topic of great interest. In particular, recently, there has been a growing attention toward the lunar rovers for working missions since the building of lunar bases is a primary objective for the lunar exploration. However, these vehicles have peculiar requirements to be taken into account in the design of each component. In this paper a particular component of a worker rover, developed as a collaboration between two academic institutions, has been designed for an optimal functionality. Each leg of this rover comprises a mechanism for lifting weights and the component considered, a decoupling joint, is a part of this mechanism. The design optimization was performed by means of parametric modelling and numerical simulations.

Keywords: Lunar rover, decoupling joint, design

1 INTRODUCTION

Because of its closeness to Earth, the Moon is an obvious target for long-term human exploration beyond Earth. Knowledge of the Moon's characteristics, especially its potential usefulness and resources, has become critical for planning the human future in space [1]. Missions to the Moon were responsible for a big volume of data, ranging from measurements of the tenuous lunar gravitational field to sample analyses. Beyond Earth, the Moon is the only body in space that has been systematically sampled. Meteorites have provided chance samples of solar system debris from the asteroids, and may even include fragments of Mars, but the Moon is the only other planet from which samples have been chipped, scooped, raked, spaded, and collected in cores.

Analyses of rocks and soils from different sites have allowed their use as "ground-truth" points for remotely-sensed physical and geochemical maps of the Moon [2].

Many conceptual designs for lunar bases have already been prepared by Americans as well as by European and Japanese engineers. In the 1950's and 1960's, many designs were put forth by scientists and engineers who hoped that by the next century a lunar base would be fully operational. In 1992, the FLO design, the First Lunar Outpost reference, mission was developed by NASA. Igloos, railroads, ecospheres, have been proposed. Inflatable structures, underground structures have all been designed. Hotels, laboratories, observatories, sports arenas, as well as mining and manufacturing plants are all very real possibilities [3,4].

A rover is generally a vehicle assigned to the transport of the crew, the exploration of the land and the picking of material samples on celestial bodies. These machines are designed to move on impervious surfaces and to cross obstacles [5,6,7].

Among the rovers that operated on the moon it is worth to mention those of the Apollo missions, known as LRV (*Lunar Roving Vehicles*), which allowed the transport of the crew and those, automatic, of the mission Lunokhod. The Apollo 13 mission was the first that included a lunar rover for the transport of the crew thus allowing the astronauts to move away from the neighbourhoods of the landing place.

Contact author: Rita Ambu¹

¹ Department of Mechanical Engineering,
University of Cagliari, Piazza d'Armi,
09123 Cagliari (ITALY)
E.-mail: ambu@iris.unica.it

The use of a lunar rover greatly increased the capability of the astronauts to explore the surface of the moon. In fact, during the first missions, when the rovers were not available, their action was limited to few steps near the Lunar Module, since the bulky spacesuit hindered the movements. In the subsequent missions, the rovers were used to accomplish the specific tasks and then they were left on the moon where actually stand [8, 9, 10].

Recently, a new concept of rover has been devised which differs from the predecessors for the tasks assigned. In fact, this rover is mainly assigned to working operations such as the movement of weights to clear from obstacles and arrange the lunar soil, the assembling of lunar bases which will be used as base field for the exploration of the deep space.

This paper focuses on the optimal design of a particular device developed for the leg of a lunar rover. The rover, designed as a collaboration between the Technical University Politecnico di Torino and the University of Cagliari, was conceived as a skilled worker with the task to clear an area allocated to the building of a lunar base for an accurate exploration.

The main component of the device is an uncoupling joint which is capable to uncouple shear and bending loads transmitted to it from the other parts. This particular device allows a correct operating of the linear actuator when the vehicle is under load. After a description of the main characteristics of the rover, the functionality of the device is analysed and a design optimisation [11] of the decoupling joint is reported.

2 DESCRIPTION OF THE LUNAR ROVER

The rover was designed to catch and lift objects with a weight up to 800N, corresponding to a mass of about 500Kg in the lunar gravity.

A scheme of the vehicle is reported in Figure 1.

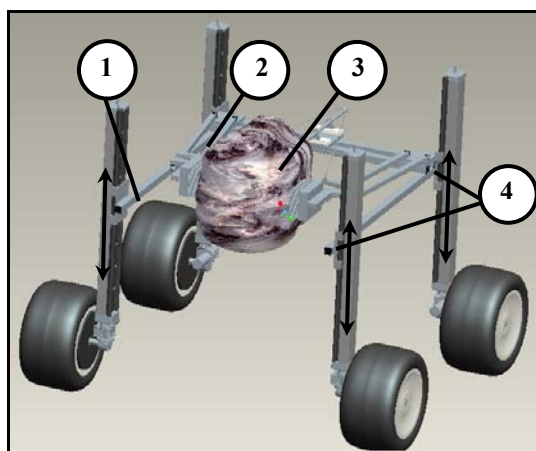


Figure 1 The worker rover.

The main components of the rover are a frame (1) which is connected to a catching mechanism (2) of the load (3). The

four columns transmit the load to the frame by means of slides (4) which are united to the frame.

This vehicle has several degrees of freedom and each column is motorized to achieve a linear motion, to manoeuvre it and correct the attitude which can be controlled to keep a defined plane, independently from the contour of the soil. In particular, each leg of the rover has been designed to allow the motion of the vehicle, the lifting of the vehicle and that of the load, the control of the attitude.

The components of the column are shown in Figure 2.

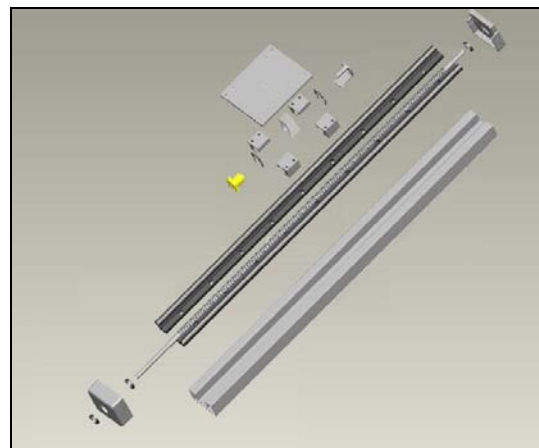


Figure 2 Components of the rover leg.

The mechanism of transmission of the lifting device uses a precision coupling between a lead screw and nut, as reported in Figure 3, where the assembling of the main components of the leg are depicted.

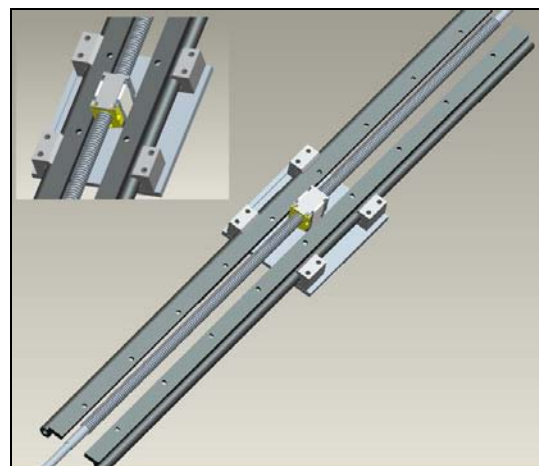


Figure 3 Assembling of the rover leg.

This mechanism was chosen as lifting device because of the advantages it offers. In fact, pneumatic and oleodynamic actuators are not suitable for the environment in which the rover operates; furthermore, this mechanism allows to stop very simply the excursion of the slide on intermediate

positions. This allows to choose the position of the frame of the rover according to the size and geometry of the weight, keeping at the same time the barycentre of the vehicle as low as possible, thus restricting the likelihood of its overturning. The lifting mechanism on each leg can be driven independently, thus allowing the vehicle to cover impervious surfaces and to cross obstacles as large as the diameter of the wheels, maintaining the attitude of the vehicle. The lead screw and the nut were assembled inside a box like metal sheet, shown in Figure 2, which was designed to contain the two guides of the slide which is connected to the lead screw mechanism by means of a decoupling device.

3 THE DECOUPLING DEVICE

The device, conceived with a different stiffness according to the component of the load transferred, was designed for transmitting to the lead screw only the axial component of the load.

This device is capable of transmitting to the lead screw only the normal component of the load, while the other components are transferred to the loading bearing structure, that is the frame of the column.

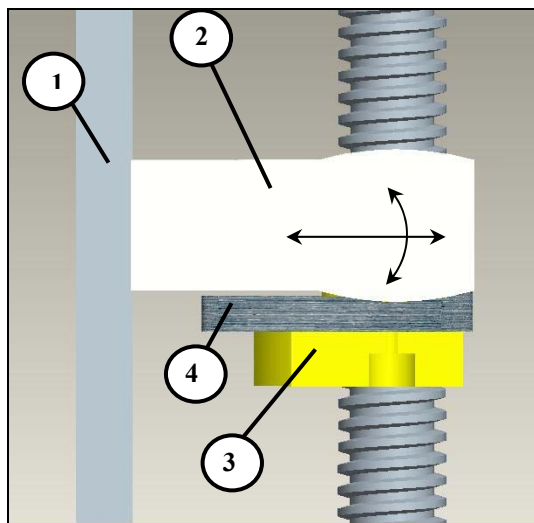


Figure 4 The decoupling device.

Referring to the Figure 4, the slide (1) is rigidly connected to a decoupling joint (2) on one side, while on the opposite side it is left free to move. In this way, the joint is simply placed on the flange (3) of the screw nut. This assembling gives to the joint the capability to rotate and to slightly slide in the radial direction with respect to the axis of the lead screw also compensating the possible misalignment between the axis of the lead screw and the axes of the guides fixed to the column. A meniscus (4), made of a material with a low friction coefficient and high strength, was placed between the joint and the screw nut to reduce the friction between the two surfaces in contact.

The slide, as evidenced in the previous Figure 3, runs on the guides and it is connected to the frame of the rover, avoiding the risk that the radial loads are transmitted to the lead screw. The parts described are assembled introducing another meniscus on the opposite side of the joint and a proper counterpart fastened to the nut by means of a screw. The overall assembly is shown in Figure 5, where the parts numbering is the same as in Figure 4.

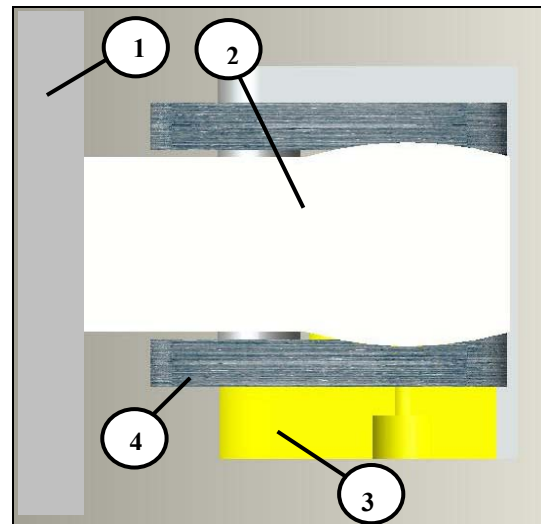


Figure 5 The overall assembly of the decoupling device.

This device, as previously described, allows to decouple the slide from the screw nut as concerns all the load components: if, during the motion of the slide, small variations of the distance between the axis of the screw nut and the slide occurs, these will not be transferred to the lead screw. As an example, in Figure 6, a small bending of the axis of the box like metal sheet is evidenced.

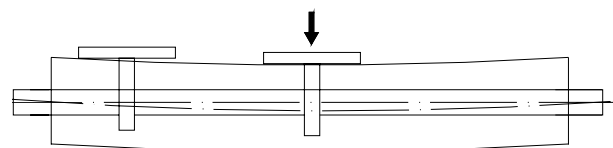


Figure 6 The bending of the column

This defect should produce a change of the relative distance between the axis of the lead screw and the slide according to the advancement of the slide. In fact, since the lead screw is constrained at its edges, it maintains a linear motion independently from the shape of the box like metal sheet, which, however, causes a deflection of the two guides that are rigidly fastened to it by means of screws. A portion of the joint was modelled as a curved shape along its arms to allow small rotations along with an axis perpendicular to the lead screw. In this way, if small misalignment errors are introduced between the lead screw and the nut, the joint is free to rotate without transmitting any bending moment on the screw nut thus avoiding the risk of the fitting of the nut on the lead screw.

4 DESIGN OPTIMIZATION OF THE DECOUPLING JOINT

Each part of the rover was designed with a parametric CAD modeller, which allows a great versatility in the design of solid components. In particular, a commercial parametric modeller was used to model the joint and the other components of the decoupling device which were then assembled together.

The detailed geometry and the functional dimensioning scheme of the joint set up according to the GD&T standards [12] is shown in Figure 7. The general tolerances were set according to the international standards [13], choosing a “f” tolerance class.

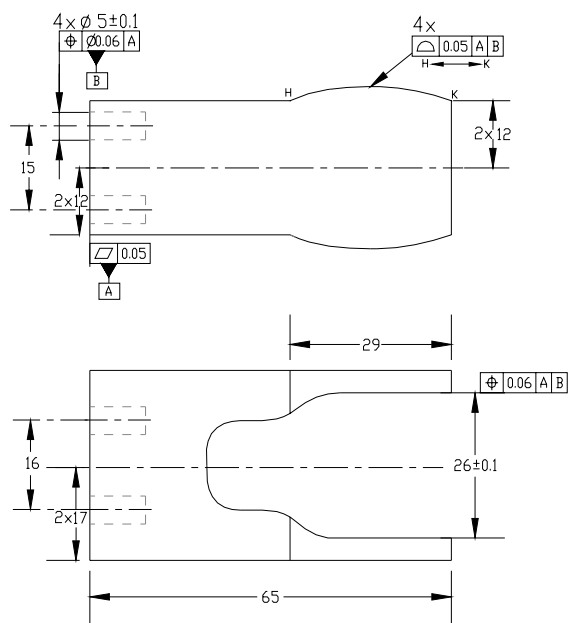


Figure 7 The geometry of the joint.

The shape and geometry of the joint were chosen to satisfy the functional requirements described in the previous paragraph. In particular, the curvature of the joint was accurately designed and that of the underlying meniscus was fitted to it so as to guarantee a correct operating of the joint together with the meniscus under load.

The Figure 8 reports the CAD model of the meniscus.

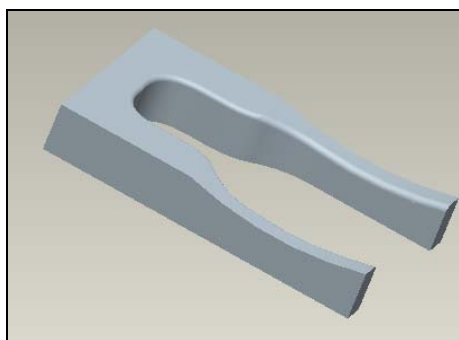


Figure 8 The model of the meniscus.

In fact, the real working conditions of the joint under load are better described by taking into account the interaction with the meniscus interposed between its surface and the flange of the screw nut.

Therefore, the process of optimization involved the evaluation of the functional parameters and the subsequent verification of the designed geometry by means of finite element simulations taking into account, in particular, extreme loading conditions.

As for the evaluation of the functional parameters, the CAD software can operate synchronised with a commercial CAT software [14] which was used to perform a mechanical variation analysis. The CAT model was set as parametric, that is, the parametric dimensions of the solid modeller are used for the construction of the dimensioning scheme of each part. This analysis was used, in particular, for the estimate of two parameters, significant for the correct operating of the joint, schematically indicated in Figure 9.

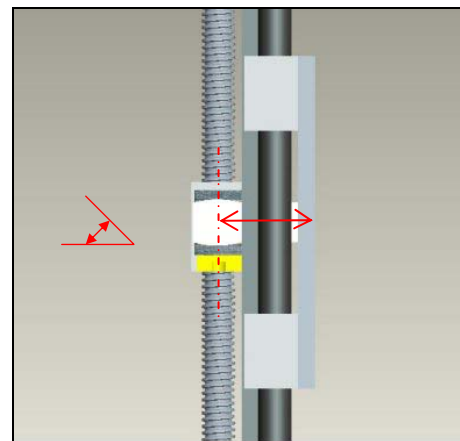


Figure 9 The functional parameters of the joint.

The first parameters is the allowed linear displacement of the joint in the direction perpendicular to the axis of the lead screw. The other parameter is the maximum angle of rotation allowed to the curved surface of the joint with respect to the upper surface of the meniscus. In fact, as discussed in the previous paragraph, the joint is designed and assembled to allow linear and angular adjustments.

As for the first parameter, it was determined by simulating the assembling at the two extreme positions corresponding to the minimum and the maximum distance between the plane of the slide and the axis of the lead screw. The calculated minimum distance between the axis of the lead screw and the slide was equal to 46,27mm, while for the maximum distance was found a value of 48,5mm. As for the angle of rotation a value of 4° was obtained.

The finite element simulations were performed by means of the ANSYS F.E.M. commercial software. The joint was made of an aluminium alloy, Anticorodal, while the material used for the meniscus was Nylon, a synthetic polymer with a low friction coefficient.

The models were made by using 3D brick elements, while contact elements were used to simulate the interface between the joint and the meniscus. The Figure 10 reports the F.E.M. models of the two components.

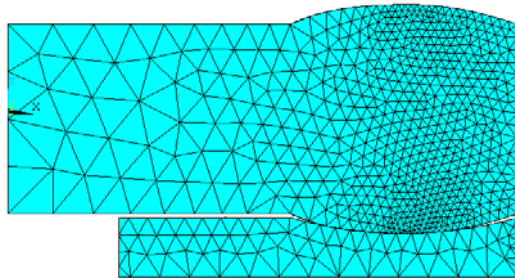


Figure 10 The FEM model of the joint and meniscus coupling.

Different simulations were performed corresponding to various conditions of loading and attitude of the rover. In particular, an extremely heavy limit condition was considered.

During the working operations of the rover on the lunar soil, an unexpected attitude of the vehicle can occur, relative to a condition where the rover is sustained only on two of the four legs. Furthermore, this situation can happen when the rover is loaded at its upper limit, thus forcing each of the two operating joints to carry the overall load. The subsequent Figure 11 reports the results obtained for this examined condition.

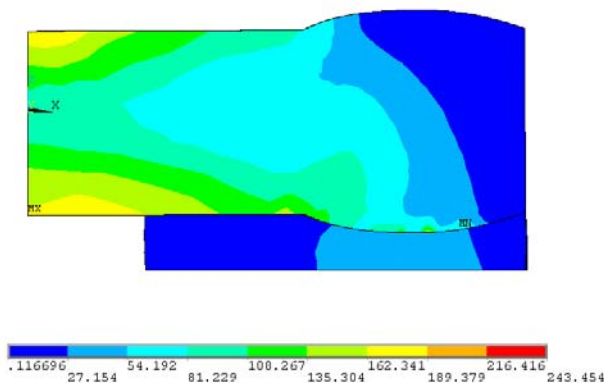


Figure 11 The von Mises stress distribution of the joint and meniscus coupling.

In particular, the Figure 11 refers an iso-colour representation of the Von Mises stress distribution relative to the joint and the underlying meniscus.

These results highlight the interaction between the joint and the meniscus and show that the assembly is under the limit stress condition.

The geometries of the parts were further verified by the evaluation of the distance between the joint and the meniscus. The nominal distance between the plane lower

portion of the joint and the plane upper portion of the meniscus is a constant value defined by the geometry of the two parts. When the rover is operating, this distance changes, depending on the attitude of the vehicle and the load it carries.

The distance was evaluated by taking into account different operating conditions, corresponding to the rover loaded at its maximum limit and the various attitudes, normal and anomalous, that can occur during the working of the rover. The results of these simulations are reported in Figure 12.

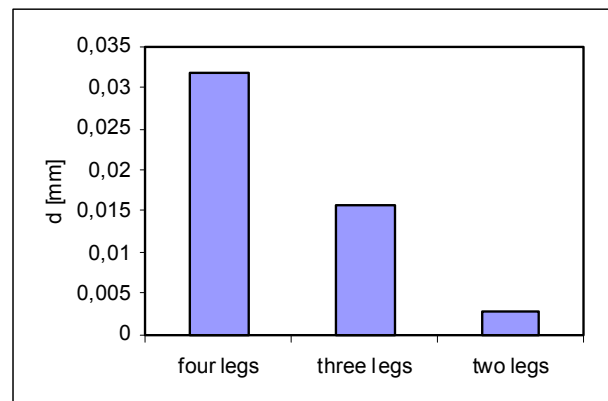


Figure 12 The distance between the joint and the meniscus

The diagram, in particular, shows that when the most critical condition occurs, corresponding to the rover sustained only on two of the four legs, a gap between the parts still exists, thus assessing the designed geometries.

5 CONCLUSIONS

In this paper a design optimization of a decoupling joint for a lunar rover leg is reported. The objective was performed by a preliminary analysis of the functionality required. The use of drawing modellers allowed to estimate the functional parameters and numerical simulations were used to verify the designed geometry of the joint, in particular, under extreme conditions.

ACKNOWLEDGMENTS

The research activity presented in this work was financially supported by the Italian Ministry of Research.

REFERENCES

- [1] Heiken G. H., Vaniman D.T. and French B.M., *Lunar Sourcebook, a user's guide to the moon*, Cambridge University Press, 1991.
- [2] Larson W. J. and Pranke L. K., *Human Spaceflight, mission analysis and design*, McGraw-Hill Higher Education, 2003.
- [3] Jones T. D., *Homesteading the Moon Aerospace America*, April 2007, pp.12-15, 2007.

- [4] <http://aerospacescholars.jsc.nasa.gov/HAS/Modules/Earth-to-Mars/6/8.cfm>
- [5] Fosness E., Guerrero, J., Qassim K. and Denoyer S.J., *Recent advances in multi-functional structures*, Aerospace Conference Proceedings, 2000 IEEE , 18-25 March 2000 Vol.4, pp. 23 – 28, 2000.
- [6] <http://www.robotics.jpl.nasa.gov/applications/applicationArea.cfm?App=1>
- [7] <http://lunarandplanetaryrovers.com/index.htm>
- [8] Fuke Y., Apostolopoulos D., Rollins E., Silberman J., and Whittaker W.R.L., *A Prototype Locomotion Concept for a Lunar Robotic Explorer*, IEEE International Symposium on Intelligent Vehicles, September ,1995, pp. 382 – 387, 1995.
- [9] Thueer T., Krebs, A. and Siegwart R., *Comprehensive Locomotion Performance Evaluation of All-Terrain Robots*, Proceedings of the IEEE/RSJ International Conference on Intelligent Robots and Systems, October 9-15 2006, pp. 4260-4265, 2006.
- [10] Estier T., Crausaz Y., Merminod B., Lauria M., Piguet R., and Siegwart R., *An Innovative Space Rover with Extended Climbing Abilities*, Proceedings of Robotics 2000: The Fourth International Conference and Exposition/Demonstration on Robotics for Challenging Situations and Environments, February 27-March 2, 2000, Albuquerque, New Mexico, USA, 2000.
- [11] Skakoon J.G., *Detailed Mechanical Design: a practical guide*, The American Society of Mechanical Engineers, 2000.
- [12]]Neumann Al., *Geometric Dimensioning and Tolerancing Workbook*, TCI- Technical Consultant Inc.,1995.
- [13] ISO 2768-1:1989, *General tolerances- Part 1: Tolerances for linear and angular dimensions without individual tolerance indications*, International Organization for Standardization,1989.
- [14] User Reference Manual CETOL 6σver.7.1 for Pro/ENGINEERING, Sigmatics, 2004.

DESIGN AND OPERATION ISSUES FOR PARALLEL ROBOTIC DEVICES IN THE REHABILITATION OF STROKE PATIENTS

Marco Ceccarelli* Doina Pîslă** Florin Graur*** Erika Ottaviano*
Călin Vaida** Rodica Ungur*** Salvatore Grande* Monica Pop***

* University of Cassino, Italy

** Technical University of Cluj-Napoca, Romania,

*** University of Medicine and Pharmacy "Iuliu Hatieganu", Cluj-Napoca, Romania,

ABSTRACT

Robotics in rehabilitation provides important opportunities to improve the quality of life for physically disabled people. Special attention must be paid to the specific needs of individual users and their physical handicaps after a stroke. The paper proposes design and operation considerations for a new multipurpose modular robotic system that will assist a patient from the first hours post stroke adapted to a specific disability of each patient with the aim to reduce the time and efficiency for limb rehabilitation.

Keywords: parallel robotic structures, rehabilitation, stroke patients, cable-based systems.

1 INTRODUCTION

Physical medicine and rehabilitation (shortly physiatry) aims to enhance and restore functional ability and quality of life to those patients with physical impairments or disabilities. Psychiatrists specialize in restoring optimal function to people with injuries to the muscles, bones, tissues, and nervous system (such as stroke patients).

The occurrence of brain trauma (stroke) is, based on the data from World Health Organization, between 1,8 – 5,4 per 1000 persons and increases with 2% each year [1]. Stroke patients often suffer post-traumatic syndromes, such as:

1. Psychic dysfunctions;
2. Neurologic organic syndromes;
3. Vegetative insufficiency;
4. Epilepsy;
5. Musculoskeletal dysfunctions.

Most patients suffer partial paralysis affecting different body regions (depending on the area of the brain where the stroke occurs) and need intensive care and recovery programs to regain mobility in the affected body areas.

Worldwide there are several robotic solutions which help the patients with disabilities in different stages of their recovery, but each of them addresses a single specific problem and in most of the cases they are still at level of laboratory prototype.

One of these robotic systems is KineAssist [2], which applies robotic technology to help the patients learn to walk forward and backward, step sideways, climb stairs and regain the balance, strength and mobility to carry on daily activities without the fear of falling.

Active Leg EXoskeleton (ALEX) has been designed for gait rehabilitation of patients with walking disabilities [3]. The manufacturer proposes force-field controller which can apply suitable forces on the leg to help it move on a desired trajectory.

Important researches take place in the Department of Rehabilitation Robotic of the Fraunhofer IPK where current research projects include the HapticWalker [4], the world's first universal robotic walking simulator for gait rehabilitation therapy of patients with impairments of the Central Nervous System (CNS), e.g. after stroke, spinal cord injury or traumatic brain injury.

A low cost and very effective solution has been proposed by Prof. Ceccarelli and his team in Cassino, who studies at the LARM Laboratory [5, 6, 7], the use of cable-based parallel mechanisms for rehabilitation tasks.

Cable-based parallel manipulator systems [8] (Figure 1) present a great interest since their architectures can overcome mainly the workspace limits of the conventional parallel manipulators with rigid body limbs.

Contact author: Marco Ceccarelli¹

¹ University of Cassino
Via Di Biasio 43, 03043 Cassino (FR), Italy
E-mail: ceccarelli@unicas.it

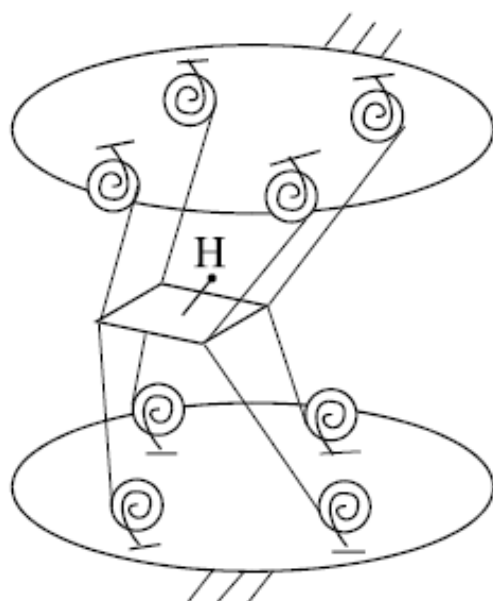


Figure 1 A scheme for cable-based parallel manipulator.

Thus, in the last decade intensive research has been dedicated on developing both theoretical/numerical investigations and prototype experiences, as indicated by the many papers that are published in journals and conference proceedings, and even with specific conference sessions. Cable-based parallel architectures can be classified as active (cable-driven parallel robots) or passive (cable-based measuring systems). Cable-driven robots are a type of parallel manipulators wherein the end-effector is supported in-parallel by n cables with n tensioning actuators. Indeed, the end-effector is operated by actuators that can release or retract cables. Cable driven manipulators are structurally similar to parallel ones, but they have additional good properties, such as large workspace, if compared to the workspace of traditional parallel manipulators. Furthermore, they have few moving parts, which give good inertial properties, high payload-weight ratio, transportability, and economical construction, as outlined in [9, 10, 11, 12, 13]. Nevertheless, feasible tasks are limited due to main characteristics of the cables. In fact, they can only pull the end-effector but do not push it. Therefore, in cable-driven parallel manipulators cables' tension must be bounded to avoid both excessive forces but also no sufficient cable's tension.

Their cheap construction and simple use makes them affordable and reliable tools for rehabilitation purposes on a large scale.

This paper proposes a new multipurpose modular robotic system that will assist a patient from the first hours post stroke until the moment he/she is capable of walking again with little or no external support. The new robotic system will be very useful in different stages of the patient recovery program in order to reduce the recovery time and improve the quality of life for stroke patients.

The paper is organized as follows: Section 2 is dedicated to the rehabilitation process and the potential use of robotic systems. Section 3 deals with the design and operation

problems for rehabilitation. Section 4 presents the some developed robotic devices for human rehabilitation at LARM. The innovative robotic system for stroke patients is presented in section 5. The conclusions of this work are presented in Section 6.

2 THE REHABILITATION PROCESS AND THE POTENTIAL USE OF ROBOTIC DEVICES

The principles of a rehabilitation process consist of: restitution, substitution and compensation. [14]. The patient state tends to improve over time but the recovery degree of different functions, as well as the recovery time depends mainly on the external support which is provided to the patient.

Restitution is relatively independent on external variables such as cognitive and physic stimulation. It includes the biochemical and genetic induced events that occur for a better restoration of the nervous tissue functionality, such as: oedema reduction, blood resorption or ionic currents and axonal transport restoration.

Substitution is influenced by external stimuli (e.g. gymnastics and exercises with the affected limb). The accommodation can depends largely on the cognitive, visual and proprioceptive networks, which contribute for learning and governs the plasticity depending on the activity. Substitution includes the functional accommodations of the remaining neural networks or those partially reconstructed for the compensation of the lost of destroyed components. Substitution can occur through the neural path partially unaffected or plastic reorganization of the cortical representation of the motions, the modification of the neuromotoric network components activities or other biologic mechanisms associated with learning and synaptic efficiency.

Compensation aims to reduce the existing non-conformities between the patient abilities and environmental necessities. It represents the most common way for patient recovery integrating several aspects: recovery (the progressive training of a partially lost function), behavioural substitution (replacing a lost aptitude with a new one, using, if necessary orthosis), accommodation (replacing the final goal with a new attainable one) or assimilation (changing the attitude of those surrounding the patient of modifying the environment).

In the figure 2 the process of rehabilitation is presented. After the neurological primary stabilization of the stroke patient, his clinical assessment follows and then the emergency treatment (medication) is applied.

In parallel, the rehabilitation process should begin as soon as possible. The first step consists of passive emergency mobility procedures (easy motions of the patient) in the first 4-6 weeks. Afterwards the spasticity could come and the active mobility procedures should be made, in which difficult motions are performed by the patient. Spasticity is common after stroke and it is manifested as muscle tightness in the affected arm and/or leg.

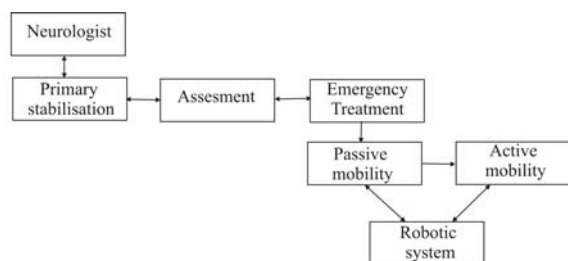


Figure 2 The rehabilitation process.

Rehabilitation helps stroke survivors relearn skills that are lost when a part of the brain is damaged. For instance, these skills can include coordinating leg movements in order to walk or carrying out the steps involved in any complex activity. Rehabilitation also teaches survivors new ways of performing tasks to circumvent or compensate for any residual disabilities. Patients may need to learn how to bathe and dress using only one hand, or how to communicate effectively when their ability to use language has been compromised.

There is a strong consensus [27] among rehabilitation experts that the most important element in any rehabilitation program is carefully directed, well-focused, repetitive practice - the same kind of practice used by all people when they learn a new skill, such as playing the piano or pitching a baseball.

Rehabilitative therapy begins in the acute-care hospital after the patient's medical condition has been stabilized, often within 24 to 48 hours after the stroke. The first steps involve promoting independent movement because many patients are paralyzed or seriously weakened. Patients are prompted to change positions frequently while lying in bed and to engage in passive or active range-of-motion exercises to strengthen their stroke-impaired limbs. ("Passive" range-of-motion exercises are those in which the therapist actively helps the patient move a limb repeatedly, whereas "active" exercises are performed by the patient with no physical assistance from the therapist.)

Patients progress from sitting up and transferring between the bed and a chair to standing, bearing their own weight, and walking, with or without assistance. Rehabilitation nurses and therapists help patients perform progressively more complex and demanding tasks, such as bathing, dressing, and using a toilet, and they encourage patients to begin using their stroke-impaired limbs while engaging in those tasks. Beginning to reacquire the ability to carry out these basic activities of daily living represents the first stage in a stroke survivor's return to functional independence.

For some stroke survivors, rehabilitation will be an ongoing process to maintain and refine skills and could involve working with specialists for months or years after the stroke.

Post-stroke rehabilitation involves physicians; rehabilitation nurses; physical, occupational, recreational, speech-language, and vocational therapists; and mental health professionals.

From the overall recovery process for stroke patients, robotic devices can be successfully used in physiotherapy,

integrating processes which require the mobilization of the patient on any level [16, 19, 20]:

- Repositioning of patients to prevent bruising, sitting lesions or joint pain (these are performed every 2 – 3 hours);
- Posture sustenance and spasticity reduction;
- Repetitive motions to retrain an affected limb to regain its mobility by creating new synapses in the brain;
- Partial or progressive sustenance of a patient's weight during the walking retrain.

Robotic devices [21, 26] present several useful characteristics which recommend their integration in a process of rehabilitation of stroke patients:

- They give tremendous opportunities for repetition and practice
- They can adjust the exerted forces at the optimum amount;
- They can repeat motions with accuracy;
- They can exert forces higher than a human therapist;
- They can work in awkward positions;
- They can work continuously.

The actual level of progress in the medical robotics field shows a clear need for the development of new devices that would contribute to a faster patient recovery, the decrease of the dedicated time per patient by the specialized personnel and the implementation of such systems in home care.

3 DESIGN AND OPERATION PROBLEMS FOR REHABILITATION PURPOSES

Several aspects must be taken into consideration for implementing robotic devices in activities that involves the direct human-machine interaction, in general and rehabilitation tasks in particular, such as: technical, operation and acceptance aspects.

Technical aspects for developing feasible safe assisting robotic devices:

- suitable workspace (which requires a careful kinetostatic analysis), transportability, in-home usage;
- force interaction at human-machine level;
- comparison with design simulations and simulated operations, (to simulate an exercise before performing it with a patient)
- parameters identification;
- end-effector design and operation (mechanical human-machine interface and therefore ergonomics considerations);
- safety issues (in case of wrong use of the motion planning and any other source of risk).

Operation features (user customized) for each specific patient:

- programming of motion patterns for the limbs, (to be customized);
- installation and transportability (to adjust the location);
- force regulation in guiding limb motion;

- end-effector adaptability (as based on the patient limb anatomy and psychological comfort).

Acceptance by doctors, physiotherapists, and patients:

- In general, doctors look for assisting devices for diagnosis and therapy exercises separately, and with the goal of medical perspective without considering the practical feasibility for the nursery and for the comfort of patients;
- On the other hand, a physiotherapist looks for flexibility and easy operation of the assisting devices;
- Finally, only recently the patients are considered for acceptance considerations of assisting devices in medical fields, even because the large variety of situations and physiological predisposition of patient.

The above short survey makes clear the need of new assisting device with new more flexible capabilities. Parallel manipulators can be used successfully as explained as follows.

4 PARALLEL ROBOTIC DEVICES FOR HUMAN REHABILITATION AT LARM

The use of robotic devices in rehabilitation is a field that has been extensively approached at the LARM Laboratory of Prof. Ceccarelli in the Cassino University Italy [5, 8, 17, 18, 22-25]. At LARM there have been developed several cable-based mechanisms having a parallel architecture that can be used in rehabilitation for various tasks.

CATRASYs is composed of a mechanical part, an electronics/informatics interface unit, and a software package, Figure 3.

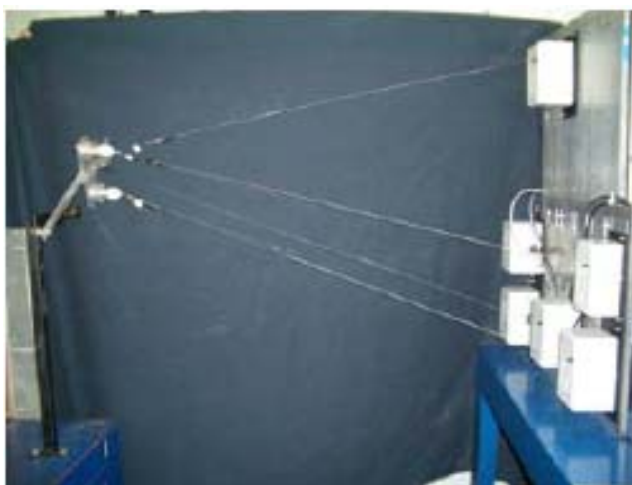


Figure 3 CATRASYs (Cassino Tracking System).

The mechanical part consists of a fixed base, which has been named as Trilateral Sensing Platform, and a moving platform, which has been named as end-effector for CATRASYs. The two platforms are connected by six cables, whose tension is maintained by pulleys and spiral springs that are fixed on the base. An end-effector for

CATRASYs is the moving platform operating as a coupling device: it connects the cables of the transducers to the extremity of a movable system. It allows the cables to track the system while it moves. Signals from cables transducers are fed through an amplified connector to the electronic interface unit, which consists of a Personal Computer for data analysis.

One simple application for the CATRASYs robotic system for rehabilitation is the muscle strengthening for the leg Figure 4, or arm, Figure 5.

Another developed robotic device is CALOWI that is composed by a mechanical cubic-frame structure, a controller, a PC for programming and monitoring, a suitable end-effector (Figure 6.)

The actuation system is composed by four DC motors, which can extend or retract cables, whose tension is controlled with suitable sensor units near the motors. The cubic-frame structure will permit to operate the parallel manipulator for either planar or spatial tasks.



Figure 4 Leg movements monitored by CATRASYs.



Figure 5 Arm exercises with CATRASYs.



Figure 6 The CALOWI (Cassino Low-Cost Wire System) robotic system.



Figure 7 Leg exercises using CALOWI robotic system.

The current CALOWI design will operate as fully constrained for planar tasks in upper plane of the frame, and as under constrained for spatial tasks within the volume of the cubic-frame structure.

Typical applications for CALOWI in rehabilitation are limb exercises with the aim to guide the limb motion patterns, and force capability, as shown in the example in Figure 7, [15].

5 AN INNOVATIVE DEVELOPMENT OF ROBOTIC DEVICES FOR REHABILITATION PURPOSES

Worldwide there are several robotic solutions which come in the aid of patients with disabilities in different stages of their recovery, but each of them addresses a single specific problem.

The paper presents a multipurpose modular robotic system that will assist a patient from the first hours post stroke until the moment he/she is capable of walking again with little or no external support.

As it is designed to assist the patient from the beginning to the end of the rehabilitation process the robotic system has been thought in a modular structure consisting of:

- a base module resembling a bed which allows the mobility of the patient (through segmental position modification);
- a dedicated module for head sustenance and mobility;
- detachable modules for upper and lower limbs mobilization;
- monitoring system for patient state and comfort.

The size of the robotic system (e.g. actuation strokes and workspace range) could be adapted to the anthropomorphic parameters of the patient. For different modules of the robotic system, kinematic parallel structures (fully or hybrid) can be used and the corresponding modules will be based on either traditional robots, cable-based robots and haptic devices. The robotic system allows the adding of dedicated specialized modules depending on the stroke topography.

The structure of a new robotic platform for rehabilitation is presented in Figure 8, emphasizing its conceptual design.

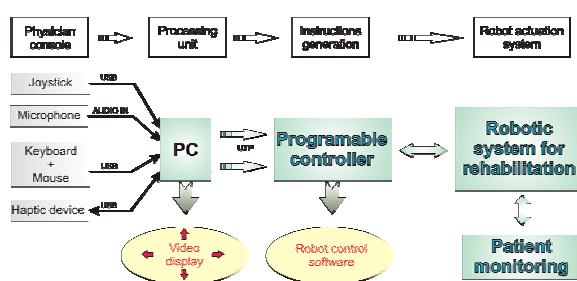


Figure 8 The structure of a new robotic system for multi-task rehabilitation purposes.

The physician's console is equipped by: a microphone (for the communication with the patient), keyboard and mouse for the configuration of the procedure parameters, a multi-functional joystick with configurable buttons that allows the repositioning of the robot and a haptic device that allows force-controlled actions. The processing unit consists of a PC that serves as a visual monitoring system for the patient and communicates with the programmable controller. On the instructions generation level the programmable controller communicates with the PC through UTP protocol and then it controls the actuators of the robotic system for rehabilitation. The robot actuation system positions the robotic device segments and sends back important data regarding the patient state (position, comfort, vital signs, distress etc.).

The novel design of the proposed robotic module will have the capability of motion along two directions, namely parallel and perpendicular with respect to the patients' position in bed. This will allow both the achievement of different postures for the patient and also the possibility of rotating the patient position in bed, critical aspect in the early hours after the stroke and for patients with severe paralysis. The possible motions of the body parts of the patient are shown in Figure 9.

The robotic device will have several predefined simple or complex individual positions and through a series of force sensors will be able to monitor the patient position.

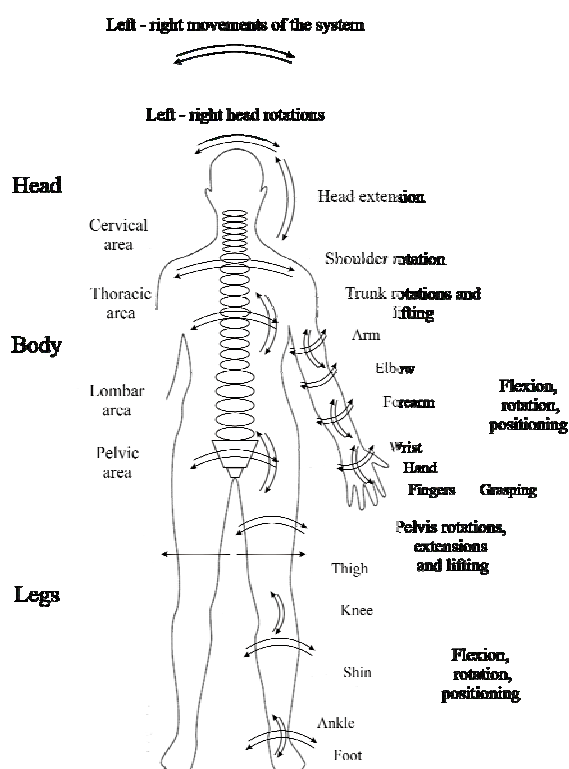


Figure 9 The possible motions of the patient.

The system will have also a contention system to prevent a severely disabled patient to fall from the bed. There will be also a thermal pneumatic mattress to regulate the body temperature and for massage. Connected to the internet, the system can be programmed by a therapist and due to the continuous patient monitoring the rehabilitation plan can be adapted for each particular individual to obtain the best results even in the home environment.

The use of haptic devices in rehabilitation is a new concept that can be applied successfully to speed up the hand-eye coordination of the patients and also the measurement of the exerted force by different body muscles which allows a very thorough evaluation pointing out which muscles require more training.

Thus, the haptic devices can be located on the upper limbs aim to help the patient to regain the tactile sense and to also regain gradually the muscle force. The tactile feedback data can be obtained by using the haptic and a virtual environment will help the patient to regain sensitive touch and the capability to perform fine motions.

6 CONCLUSIONS

The paper emphasizes the need of a joint effort of doctors and engineers in the development of new assisting devices in rehabilitation therapies of stroke patients. An analysis of current solutions with robotic devices has shown problems and possibilities in using successfully cable-based parallel manipulators as assisting devices in rehabilitation therapies.

In particular, in the paper an innovative multitask solution is proposed with a modular design and flexible operation through an outline of basic considerations for a new system with suitable features of low-cost, easy-operation, and user-oriented installation. The proposed robotic device can be adapted to a specific disability of each patient through a predefined schedule and monitoring of suitable exercises with the aim to reduce the time and efficiency for limb rehabilitation in stroke patients.

ACKNOWLEDGEMENTS

The work reported in this paper has been developed in a joint collaboration between the University of Cassino, Italy, Technical University of Cluj-Napoca, Romania and University of Medicine and Pharmacy "Iuliu Hatieganu", Cluj-Napoca, Romania.

7 REFERENCES

- [1] Ganea, M. Brain vascular insufficiency for invalid persons after a brain trauma (Neurologic, medical and social aspects). PhD Thesis. 2006.
- [2] KineaDesign, <http://www.kineadesign.com/portfolio/kineassist/> 2009.
- [3] Agrawal, S., Banala S., Fattah A., Sangwan V., Scholz J., Hsu, W. Assessment of Motion of a Swing Leg and Gait Rehabilitation with a Gravity Balancing Exoskeleton, *The IEEE Transactions on Neural systems and Rehabilitation Engineering*. 2007.
- [4] Schmidt, H., Werner, C., Bernhardt, R., Hesse, S., Krüger, J. Gait rehabilitation machines based on programmable footplates *Journal of NeuroEngineering and Rehabilitation* 2007, 4:2 (9 February). 2007.
- [5] Ceccarelli, M., Ottaviano E. Cable-Based Parallel Manipulators for Rehabilitation purposes of human limbs, *2nd international Colloquium Collaborative Research Centre 52*, Braunschweig, Germany, pp.53-67. 2008.
- [6] Lahouar S., Ottaviano E., Zeghoul S., Romdhane L. Ceccarelli M. Collision Free Path Planning for Cable Driven Parallel Robots, *2nd International Congress Design and Modelling of Mechanical Systems*, Monastir, 19-21 March. 2007.
- [7] Palmucci F., Ottaviano E., Ceccarelli M. An Application of CaTraSys, a Cable-Based Parallel Measuring System for a Kinetostatic Analysis of Human Walking, *Proceedings of MUSME 2008, the International Symposium on Multibody Systems and Mechatronics San Juan (Argentina)*, 8-12 April. 2008.
- [8] Ceccarelli, M., Ottaviano E., Tevolieri C. 2007. Experimental activity on cable-based parallel manipulators: *issues and results at LARM in Cassino*, Tunisia.
- [9] Verhoeven R., Hiller M., Tadokoro S., Workspace, Stiffness, Singularities and Classification of Tendon-Driven Stewart-Platforms, *Int. Symposium on Advances*

- in *Robot Kinematics ARK*, Strobl, Austria, pp. 105-114. 1998.
- [10] Fattah A., Agrawal, S.K.. Workspace and Design Analysis of Cable-Suspended Planar Parallel Robots”, *ASME Mechanisms and Robots Conf.*, Montreal, paper MECH-34330. 2002
- [11] Riechel A. T., Ebert-Uphoff I. Force-Feasible Workspace Analysis for Underconstrained, Point-Mass Cable Robots, *IEEE Int. Conf on Robotics and Automation ICRA'04*, New Orleans, pp. 4956-4962. 2004.
- [12] Hiller M., Fang S., Mielczarek S., Verhoeven R., Franitza D. Design, Analysis and Realization of Tendon-Based Parallel Manipulators, *Mechanism and Machine Theory*, Vol. 40 pp. 429-445. 2005.
- [13] Ottaviano E., Ceccarelli M., Toti M., Avila Carrasco C. CaTraSys (Cassino Tracking System): A Wire System for Experimental Evaluation of Robot Workspace, *Journal of Robotics and Mechatronics*, Vol. 14, No.1, , pp.78-87. 2002.
- [14] Popescu C.D, Băjenaru O., Muresanu Fior D., Bohotin V., Buia R., Popescu B.O. Therapeutic protocol for the neurologic disfunctions recovery for stroke and brain trauma patients, *In the Romanian Neurology Journal*, Vol. V., No. 4., pp. 181-188. 2006.
- [15] Grande, S. Operation and Optimisation of Catrasys for walking monitoring, *LARM Internal Report*, LARM, Cassino (in Italian). 2008.
- [16] Berteanu M. Stimulation triggered through electromiographic feedback for had recovery for the hemiplegic patient. *Rev de Recup. Med Fiz și Baln. Nr. 1*. 2003.
- [17] Ceccarelli M., Ottaviano E., Toti M. Experimental Determination of Robot Workspace by means of CATRASYS (Cassino Tracking System), *13th CISM-IFTToMM Symposium on Theory and Practice of Robots and Manipulators Ro.Man.Sy.'2000*, Springer-Verlag, Wien, pp.85-92. 2000.
- [18] Castelli G., Ottaviano E., Ceccarelli M. Modeling and Simulation of A Cable-Based Manipulator for Rehabilitation Therapies, *3rd International Conference Optimization of the Robots and Manipulators OPTIROB 2008*, PREDEAL, Bucharest, pp.277-282. 2008.
- [19] Dutsch, J., J. Latonio, G. Burdea, R. Boian. Rehabilitation of Musculoskeletal Injuries Using the Rutgers Ankle Haptic Interface: Three Case Reports, *Eurohaptics Conference*, Birmingham UK, 6 pp. July 1-4. 2001.
- [20] Hesse S, Werner C, Matthias K, Stephen K, Berteanu M. Non-velocity-related effects of a rigid double-stopped ankle-foot orthosis on gait and lower limb muscle activity of hemiparetic subjects with an equinovarus deformity. *Stroke*, Sep;30(9):1855-61. 1999.
- [21] Merlet J. P., *Parallel Robots*. Springer, 2006.
- [22] Ottaviano E., Ceccarelli M. Numerical and experimental Characterization of Singularities of a Six-Wire Parallel Architecture, *Robotica*, Vol. 25, pp. 315-324. 2007.
- [23] Ottaviano E., Ceccarelli M., De Ciantis M. A 4-4 Cable-Based Parallel Manipulator for an Application in Hospital Environment, *15th Mediterranean Conference on Control and Automation – MED07*, Athens. 2007.
- [24] Ottaviano E., Ceccarelli M., Palmucci F. “Experimental Identification of Kinematic Parameters and Joint Mobility of Human Limbs”, *2nd International Congress Design and Modelling of Mechanical Systems*, Paper 103, 2007.
- [25] Ottaviano E., Ceccarelli M., Grande S. An Experimental Evaluation of Human Walking, *3rd International Congress Design and Modelling of Mechanical Systems CMSM'2009*, Paper 43. 2009.
- [26] Pisla, D. *Kinematic and Dynamic Modelling of Parallel Robots.*, Cluj-Napoca, Casa Cartii de Stiinta Publishing House. 2005.
- [27] Pop, L. *Textbook of Physiotherapy.* Iuliu Hatieganu Publishing House Cluj. 2006.

EXPERIMENTAL MOBILE ROBOTIC PLATFORM

Peter Čepon* Roman Kamnik* Jernej Kuželički** Tadej Bajd* Marko Munih*

* Faculty of Electrical Engineering, University of Ljubljana, Slovenia

** Iskra Avtoelektrika, d.d., Šempeter pri Gorici, Slovenia

ABSTRACT

Paper presents an experimental mobile robotic platform aimed at user friendly development of new mobile robotics applications. The development system incorporates the mobile platform construction, the drive unit with traction and steering wheel, main controller, the drive controller and the software development environment. The embedded controller running under xPC Target real time operating system is implemented in mobile platform. The controller controls drive units via CAN communication. The system enables software development and robot control on a remote host supervisory computer. The development system is based on Mathworks Matlab tools Simulink, Stateflow and xPC Target. This configuration allows the development of control algorithm in graphical mode by building and connecting functional blocks. In this way the development system is built providing user friendly graphical software development environment, optimal tuning of parameters, acquisition and logging of signals, and easy incorporation of new devices.

Keywords: mobile robotic platform, CAN bus, experimental development system

1 INTRODUCTION

Mobile robots are automatic devices that are capable of autonomous motion in a given environment. They can move over ground, in air, or water using wheels, legs or other locomotion mechanisms. With the latest development in drives, perception, control, and localization the number and areas of mobile robots applications are increasing. Most mobile robots use wheels to move in their environment. Wheeled mobile robots are divided according to their kinematic configuration into the unicycle, bicycle, differential drive, and tricycle. The kinematics of motion of a wheeled mobile robot depends on friction in the contact between the wheel and ground. In literature different approaches to modelling the kinematics can be found [1], [5], [8], [9].

Software development for mobile robot is often time consuming process. An important issue in the development is open access to the robot controller what enables the development of low level control algorithms, management, and easy integration of new sensors and other components [6], [11]. In the development of real autonomously moving system the use of simulations is recommended [4]. Simulation environments provide a rapid prototyping environment for modelling, programming and simulating mobile robots motion (Webots - Cyberbotics Ltd. [10], Matlab/Simulink - Mathworks, Inc. [2]). Mobile robots are becoming commercially available and thus becoming accessible to a wider range of users (K-TEAM: Hemisson, KoalaII, KheperaIII, and MobileRobots: Pioneer 3, Patrol-Bot and Seekur).

In this paper, a mobile robotic platform developed for rapid software prototyping is presented. In the first chapter the mechanical configuration and drive system are described. In the second chapter, the kinematic model of mobile robotic platform is derived. The third chapter presents open access robot controller. In final chapter, a simple motion control algorithm is developed and evaluated by reference kinematic measuring system.

Contact author: Peter Čepon¹, Roman Kamnik²

¹ E-mail: peter.cepon@robo.fe.uni-lj.si

² E-mail: roman.kamnik@robo.fe.uni-lj.si

URL: <http://robo.fe.uni-lj.si>

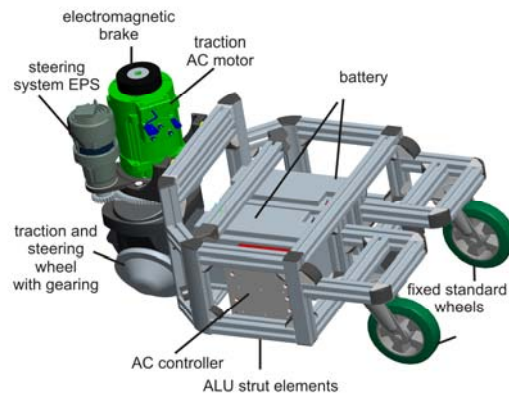


Figure 1 Mechanical construction of mobile robotic platform

2 MECHANICAL CONFIGURATION

Mobile robotic platform was built on the basis of a driving system used in industrial forklifts. The driving system is a compact unit incorporating the traction and steering modules aimed for driving a single wheel. Steering is controlled by an EPS system which incorporates a DC motor (0.15 kW, max torque 1.1Nm at 1600 rot/min) and a DSP based controller implemented in the motor housing. The driveline motor is a three phase AC motor (Iskra AML7103, 15 V, 2.2 kW) driven by a separate DSP based controller AES1136 which controls the magnetic field vector by 10 kHz sampling frequency and maximal current of 400 A. Both motor controllers are connected with the supervising computer via CAN bus [7] using CANopen protocol [3]. Besides, an electromagnetic brake is implemented at the traction motor.

The kinematic configuration of a mobile robot encompasses two passive and one driving wheel. At the robot construction the AC motor controller, the robot controller and two dry lead-acid batteries are mounted. The mechanical construction is build of Aluminium strut elements as presented in Figure 1. The platform is designed as to enable mounting and manipulation of an additional robot system at the top of the platform. The dimensional drawing of the mobile platform is presented in Figure 2.

3 KINEMATIC MODEL

Kinematic model of the mobile robot describes its position and orientation in the global coordinate system. The kinematic model accounts for motion constraints imposed by wheels. The position of the robot in the plane is represented by a vector of two position coordinates and an angle of rotation:

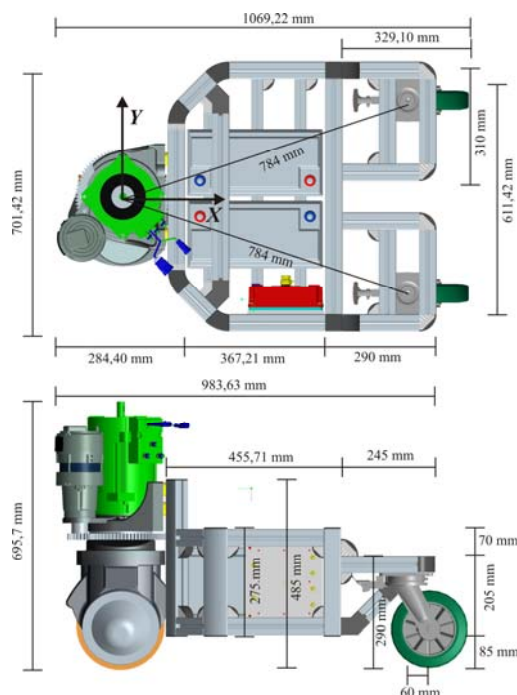


Figure 2 Dimensional drawing of a mobile robotic platform.

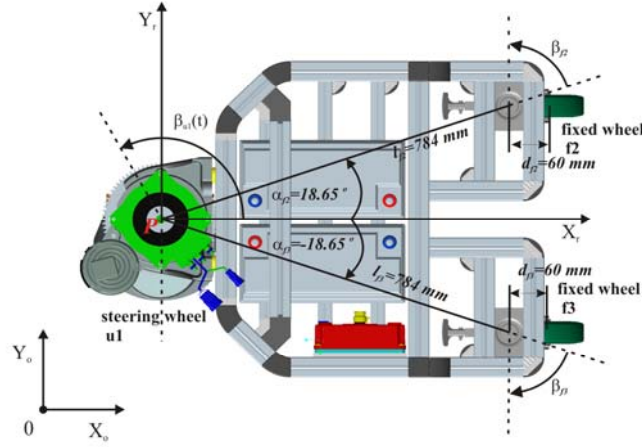


Figure 3 Kinematic parameters of three wheel configuration with fixed standard wheels.

$$\xi_o = \begin{bmatrix} x \\ y \\ \theta \end{bmatrix}$$

- (1) The configuration parameters for mobile platform with one steering and two fixed wheels are presented in Table I.

Table I - Configuration parameters of mobile platform with one steering and two fixed wheels

wheel	α [°]	β [°]	l [mm]	d [mm]	r [mm]
u1	0	$\beta_{u1}(t)$	0	0	115
f2	18,65	71,35	784	60	100
f3	-18,65	108,65	784	60	100

Assuming planar motion, the speed vector $\dot{\xi}_o = [\dot{x} \ \dot{y} \ \dot{\theta}]$ can be transformed into robot local coordinate system by using rotational RotZ homogenous matrix:

$$\dot{\xi}_r = \mathbf{R}(\theta) \cdot \dot{\xi}_o \quad (2)$$

Constraints of motion imposed by fixed standard wheels depend on five constant parameters (α , β , l , r , d) which are determined by wheel mounting (see Figure 3) and a variable angle of wheel forward rotation $\phi(t)$.

For a single standard fixed wheel, the rolling constraint is expressed as:

$$[\sin(\alpha + \beta) \quad -\cos(\alpha + \beta) \quad (-l) \cdot \sin \beta] \cdot \mathbf{R}(\theta) \cdot \dot{\xi}_o = r \cdot \dot{\phi}(t)$$

When above equation is written in a matrix form encompassing all standard fixed wheels, the rolling constraint is described:

$$\mathbf{J}_1(\beta_u) \cdot \mathbf{R}(\theta) \cdot \dot{\xi}_o - \mathbf{J}_2 \cdot \dot{\phi}(t) = 0 \quad (3)$$

Similarly, the sliding constraint for a fixed standard wheel is expressed as:

$$[\cos(\alpha + \beta) \quad \sin(\alpha + \beta) \quad d + l \cdot \sin \beta] \cdot \mathbf{R}(\theta) \cdot \dot{\xi}_o = 0$$

and, when written in a matrix form incorporating all standard fixed wheels, the equation gets the form:

$$\mathbf{C}_1(\beta_u) \cdot \mathbf{R}(\theta) \cdot \dot{\xi}_o + \mathbf{C}_2 \cdot \dot{\beta}_k(t) = 0 \quad (4)$$

On this basis, the matrices describing the wheel rolling and sliding constraints are:

$$\mathbf{J}_1(\beta_{u1}) = \begin{bmatrix} \sin \beta_{u1}(t) & -\cos \beta_{u1}(t) & 0 \\ 1 & 0 & -251 \\ 1 & 0 & 251 \end{bmatrix}$$

$$\mathbf{J}_2 = \begin{bmatrix} r_{u1} & 0 & 0 \\ 0 & r_{f2} & 0 \\ 0 & 0 & r_{f3} \end{bmatrix} = \begin{bmatrix} 115 & 0 & 0 \\ 0 & 100 & 0 \\ 0 & 0 & 100 \end{bmatrix}$$

$$\mathbf{C}_1(\beta_{u1}) = \begin{bmatrix} \cos \beta_{u1}(t) & \sin \beta_{u1}(t) & 0 \\ 0 & 1 & 803 \end{bmatrix}$$

$$\mathbf{C}_2 = 0$$

Since the passive standard fixed wheels do not constrain the rolling in the direction of motion, the kinematic model is simplified:

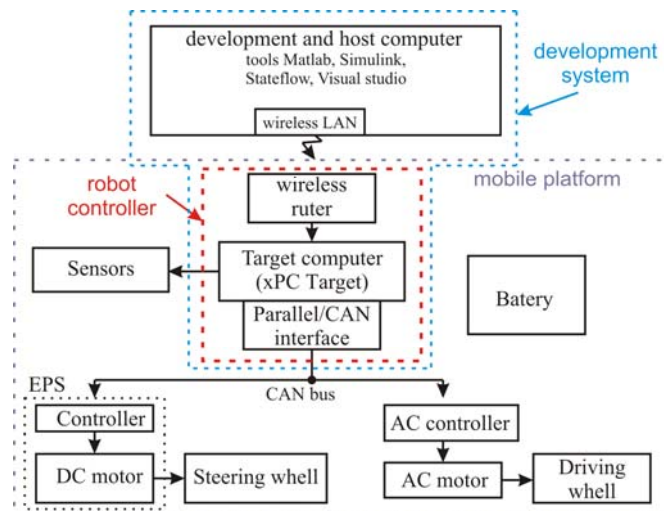


Figure 4 Conceptual scheme of the mobile robot control system.

$$\begin{bmatrix} \mathbf{J}_2 \cdot \dot{\phi}(t) \\ 0 \end{bmatrix} = \begin{bmatrix} \mathbf{J}_{1u}(\beta_{u1}) \\ \mathbf{C}_1(\beta_{u1}) \end{bmatrix} \cdot \mathbf{R}(\theta) \cdot \dot{\xi}_o \quad (5)$$

what gives:

$$\begin{bmatrix} 115 \cdot \dot{\phi}(t) \\ 0 \\ 0 \end{bmatrix} = \begin{bmatrix} \sin \beta_{u1}(t) & -\cos \beta_{u1}(t) & 0 \\ \cos \beta_{u1}(t) & \sin \beta_{u1}(t) & 0 \\ 0 & 1 & 803 \end{bmatrix} \cdot \mathbf{R}(\theta) \cdot \dot{\xi}_o$$

On the basis of kinematic parameters the degrees of mobility δ_m , steerability δ_v and manoeuvrability δ_M are defined for the mobile robotic platform:

$$\delta_m = \dim N [\mathbf{C}_1(\beta_{u1})] = 3 - \text{rang} [\mathbf{C}_1(\beta_{u1})] = 1$$

$$\delta_v = \text{rang} [\mathbf{C}_{1u}(\beta_{u1})] = 1$$

$$\delta_M = \delta_m + \delta_v = 2$$

4 ROBOT CONTROLLER

For the software development, operation supervision and control of the mobile robot platform the host/target concept is used. This concept employs two computers: the target computer, which is mounted at the robot platform, and the host computer, which is a desktop or portable computer. Both computers communicate via wireless TCP/IP link. A PC/104 PCM3380 (Advantech, Inc.) is employed as target controller. This small size (108 mm x 115 mm) embedded controller implemented at the platform performs data exchange with host computer, acquisition of sensory feedback signals, calculation of the command signals and control of the steering and driving motors. It operates in a hard real time on the basis of xPC Target operating system (Mathworks, Inc.) with sample rate of 1 kHz. On the host computer, the Matlab/Simulink software environment is utilized for development of control algorithms and supervision of target controller operation. The host/target concept of the mobile robot control system is presented in Figure 4 and 5.

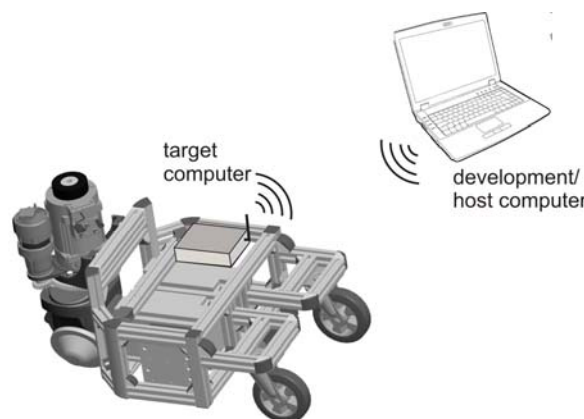


Figure 5 Conceptual drawing of the host/target control principle.



Figure 6 Mobile robotic platform during manoeuvring.

Robot controller software is developed in graphical environment of the Matlab/Simulink package that enables usage of tools and blocks from Matlab libraries (including I/O interfaces), development of own blocks via S-function interface and usage of Stateflow tool for controlling discrete events. Programming is user friendly and eased by graphical approach. When the program is developed in the form of functional Simulink model, it is compiled to the executable code by the help of Real-Time Workshop tool. The executable code is loaded to the target computer and executed in real time. The remote access to control of the target computer operation, signals logging and parameters changing from the host is provided.

5 EXPERIMENTAL EVALUATION

In the experimental evaluation of the mobile robotic platform, the developed control system was tested. In the experiment, the robot controller guided the mobile platform along the pre-programmed trajectory. In Figure 6 the mobile robotic platform is shown during manoeuvring at

flat surface. During manoeuvring the steering direction was controlled in a position control mode, while the velocity controller controlled the velocity of traction. Tested block scheme of control concept is presented in Figure 7, and the Simulink scheme of the control algorithm in Figure 8. The information about driving wheel velocity $\dot{\phi}$ and steering direction β was used in kinematic model (5) to determine the robot calculated position. For reference comparison, the kinematics measurement system OptotrakCertus was used to measure the platform's absolute position and orientation. The results shown in Figure 9 compare the measured and calculated position and orientation of the mobile robotic platform in three graphs presenting robot's position along x and y directions, and its rotation, respectively. The calculated position and orientation were determined as relative displacements with regards to the initial pose by the help of integration of velocities.

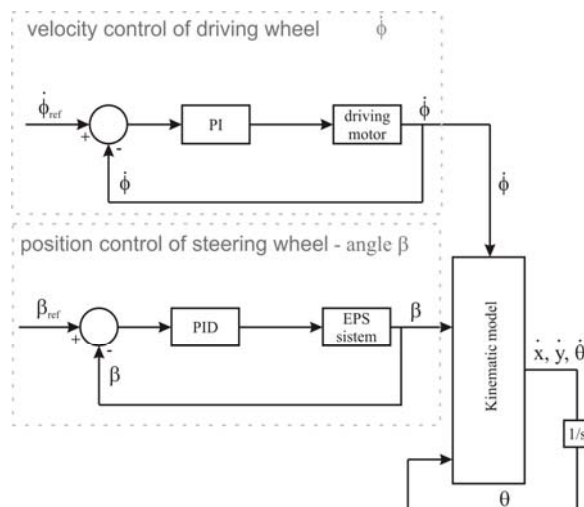


Figure 7 Control algorithm block scheme for driving and steering.

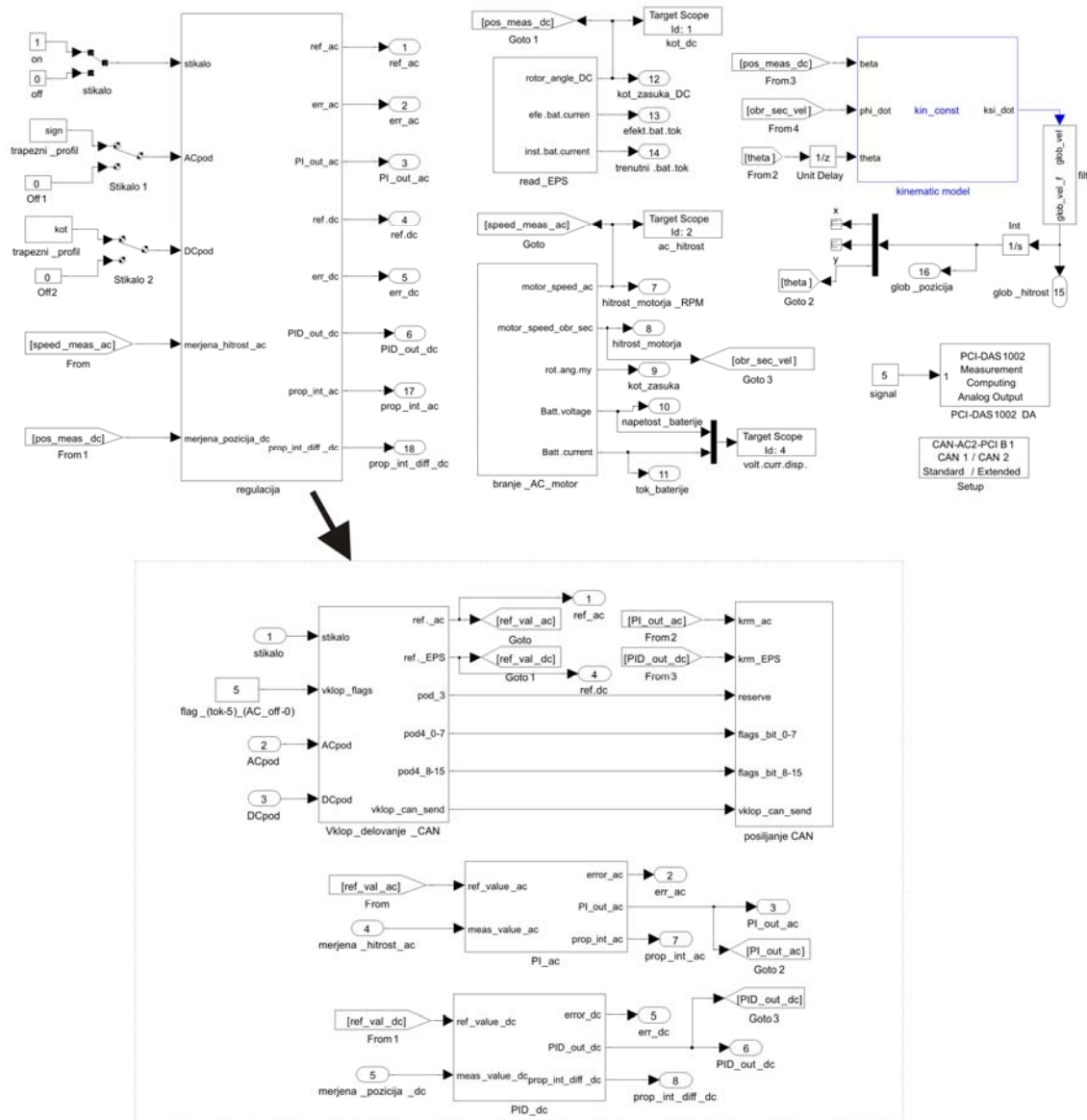


Figure 8 Control algorithm for driving and steering realized in Simulink environment.

6 CONCLUSION

The paper presents the design and control of the experimental mobile robotic platform. The mobile platform is built on the basis of driving system used in industrial forklifts. Chosen configuration provides robust operation in heavy duty operating conditions. The platform is mechanically designed as a three-cycle incorporating one traction and two passive wheels. The chassis is build of Aluminium strut elements providing flexibility in configuration changing and mounting of various sensors and loads.

The robot controller is designed as embedded target controller with additional host/development computer. It is based on Mathworks Matlab/Simulink environment and real time xPCTarget operating system. This configuration

provides an open concept with access to the low level motor control. The controller enables position, velocity or torque control mode of operation. The programming environment enables easy and user friendly development of control algorithms, easy implementation of additional sensory systems, and easy access to the signals logging and parameters tuning.

The presented experimental evaluation of mobile platform automatic manoeuvring proved the kinematic model and implemented control concept.

The proposed areas of applications for developed mobile robotic platform are in education and experimental development of new control algorithms for novel applications of mobile robots.

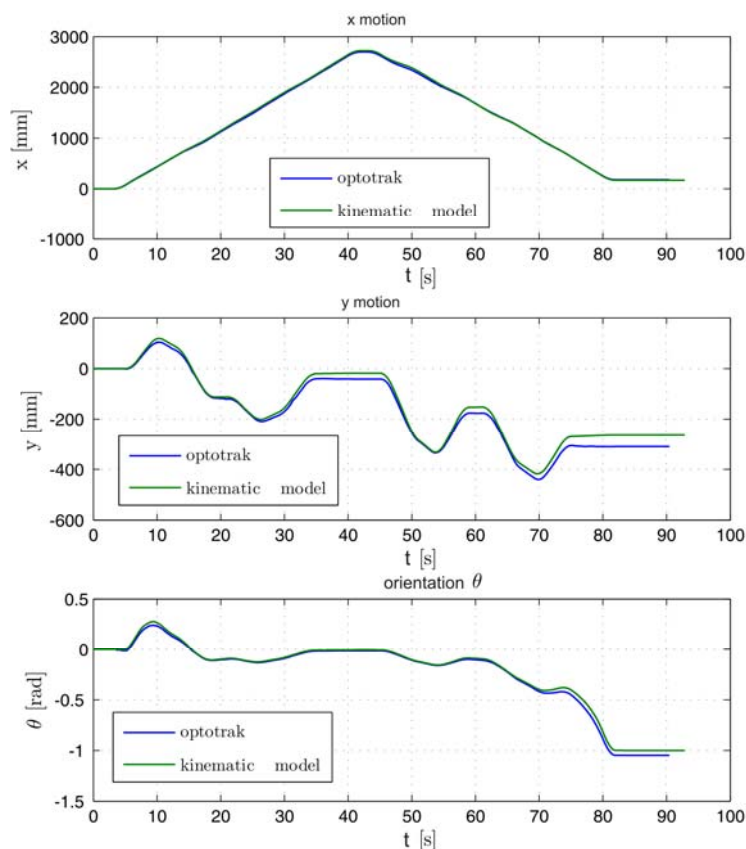


Figure 9 Comparison of measured and calculated pose of mobile robotic platform during motion.

7 ACKNOWLEDGMENTS

The authors acknowledge the Republic of Slovenia Ministry of Defense and Ministry of Education, Science and Sport grants "Mobile Robot System for Supervision, Search and Rescue Missions" (M2-0116), "Motion Analysis and Synthesis in Human and Machine" (P2-0228 C).

8 REFERENCES

- [1] Alexander, J. C. and Maddocks, J. H., On the kinematics of wheeled mobile robots. In: *Autonomous robot vehicles*. pp. 5-24, Springer-Verlag New York, Inc., 1990.
- [2] Bongiovanni, M., An experimental framework for rapid prototyping of mobile robot controllers. *International Conference Towards Autonomous Robotic Systems (TAROS)*, London, pp. 21-27, 2005.
- [3] Boterenbrood, H., *CANopen high-level protocol for CAN bus*. NIKHEF Amsterdam, 2000.
- [4] Campion, G. and Chung, W., Wheeled robots. In: *Springer Handbook of Robotics*. pp. 391-410, Springer-Verlag, Berlin, 2008.
- [5] Campion, G., Bastin, G. and D'Andrea-Novell, B., Structural properties and classification of kinematic and dynamic models of wheeled mobile robots. *IEEE Transaction on Robotics and Automation*, Vol. 12, No. 1, pp. 47-62, 1996.
- [6] Dudek, G. and Jenkin, M., *Computational Principles of Mobile Robotics*. 1st edition, Cambridge University Press, Cambridge, 2000.
- [7] Farsi, M. and Barbosa, M., *CANopen Implementations: Applications to Industrial Networks*. Research Studies Press Ltd., Exeter, 2000.
- [8] Kim, D., Kwon, W. H. and Park, H. S., Geometric Kinematics and Applications of a Mobile Robot. *International Journal of Control, Automation, and Systems*, Vol. 1, No. 3, pp. 376-384, 2003.
- [9] Muir, P. and Neuman, C. P., *Kinematic Modeling of Wheeled Mobile Robots*. Technical report, Robotics Institute, Pittsburgh, PA, 1986.
- [10] Oliver, M., Webots: Professional Mobile Robot Simulation. *International Journal of Advanced Robotic Systems*, Vol. 1, No. 1, pp. 39-42, 2004.
- [11] Siegwart, R. and Nourbakhsh, I., *Introduction to Autonomous Mobile Robots*. The MIT Press, Cambridge, 2004.

HIGH RESOLUTION PLANE ANGULAR MEASUREMENT SYSTEM: REALISATION AND ERROR EVALUATION

Andrea Manuello Bertetto Roberto Ricciu

Department of Mechanical Engineering, University of Cagliari, Italy

ABSTRACT

An high resolution angular measurement system, based on an indirect time measuring to detect the angular value, is designed and realised. In the paper the basic principle is referred and the logical scheme of the device is discussed. Finally the measurement error is evaluated and are referred and discussed the performed tests.

Keywords: high resolution, angular measurements, error evaluation.

1 INTRODUCTION

The object of this research is the development and implementation of a compact instrument for the measurement of angles with a resolution higher than those of the instruments currently in the market. The cultural background of this research is the discipline of the mechanical measures in relation to the instruments for the angular measurements [1, 8]. An improvement in the resolution of angular measurements should give advantages in many disciplines such as topography, applied mechanics, astronomy, biomechanics, robotics.

Among the most widespread angular transducers, the commercial angular encoders can be essentially subdivided in optical and magnetic ones [2, 3, 5]. Despite its consolidate technology, the research is very active in this field [4, 7, 9-12].

To obtain a resolution close to the sessagesimal arc second, the classical way is to divide a circumference in equal portions either physically or by an optical technique. The physical limit of this subdivision is due to the radius dimension. For example for a disk having a radius of 1cm, a subdivision correspondent to a sessagesimal arc second requires a distance between the subdivisions of $5 \cdot 10^{-8}$ m. This distance is the same order of magnitude of the inter-atomic distance between the atoms of a metallic material.

Currently, to obtain this resolution value it is necessary to use circumferences with a diameters of several meters. For example, one of the most accurate commercial instruments available, used in topography, has a resolution that does not exceed $0,5''$ (sessagesimal arc second), but they do not often exceed $1''$ and sometimes the uncertainty is not declared but it is included between the value of the resolution and $3''$.

The state of the art is represented by the various base units for the measurement of the angles. Until some years ago the base angular unit devices were essentially a mechanical system. It was essentially a plate with index driven by a couple of gears. Actually these devices are replaced by a plate whose constant angular velocity is controlled by an interferometer. The system is based on the relativistic property of the invariance of the velocity of the light. In this device interference fringes are produced when the plate rotates with respect to an inertial system generating a signal similar to that of a typical angular optical encoder. The declared uncertainty is currently $0.2''$ sessagesimal arc second for a covering factor "k" equal to 2 [6].

These base units are laboratory instruments with a high resolution and are representative of the state of the art in the field. The improvement of the resolution and uncertainty of these measure instruments should improve each specific branch of applications.

Some examples of innovative applications can be cited. In Topography the use of the so called "total stations", with a resolution higher than those actually available, should promote a better accuracy in the definition of the cadastral public register maps, IGM maps, etc., thanks to a higher accuracy in the determination of the distances between the landmarks. In mechanical engineering new encoders are placed on rotating shafts in engines or electrical servomotors: these should assure a better resolution in the measurement of the rotation angles of the shafts. This should promote a higher accuracy in specific applications like the motion of robots for clinic applications, in particular for those addressed to the remote surgery. Compact sizes of the angular gauge are fundamental to design robotic arms. A higher resolution of the encoders assembled on the joints should improve the operating accuracy of the end effector. In astronomy encoders mounted on orbiting telescopes should assure higher angular resolutions than those actually available, for

example, in the measurement between two target points. It is important to point out that the instruments for the measurement of the angles for spatial applications are useful only if they are compact and have a low mass because they must be shippable in the space; furthermore, a higher resolution should be desirable.

2 THE BASIC PRINCIPLE AND THE PROTOTYPE

The device is based on a principle actually not exploited by the angular gauges: an indirect angular measurement is carried out by time measuring, which should be most resolving than a direct angular measurement.

As shown in the scheme represented in figure 1, the target P travels circular paths with an angular velocity ω , for a time period t . A scheme of the device is shown in figure 2. It can be seen the frame (1), supporting the high precision speed controlled brushless motor (2) and the optical encoder (3). The disk (4) is keyed on the rotating motor shaft. The disk was built using a sandwich technology interposing a black layer between two Plexiglas transparent layers. On the shaft, in the upper side, there is a high precision low friction bearing, for hard disk drive technology, to decouple the shaft motion respect to the arm (5), supporting the mobile sensor (6).

The measure can be performed because the motor is rotating the disk transparent to electromagnetic radiation coming from sensors (3) and (6) in figure 2. These gauges are photoelectric grooved sensors like those in high precision printers.

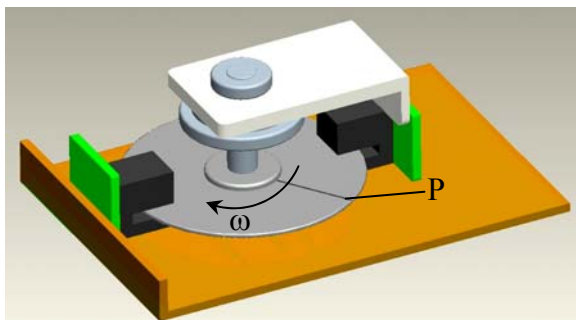


Figure 1 The device scheme.

The path could be seen as a sequence of finite distances Δs , corresponding to given angular amplitudes $\Delta\theta = \Delta s/r$, where r represents the radius of the circular path.

If the angular velocity ω is given as a constant for each interval of the path Δs_i , related to the generic angular amplitude $\Delta\theta_i$, it can be written:

$$\omega = \frac{\Delta\theta}{\Delta t} = \frac{\Delta\theta_i}{\Delta t_i} \quad (1)$$

As the angular velocity is supposed constant, the cumulated angular path can be related to each interval:

$$\omega = \frac{\theta}{t} = \frac{\sum_{i=0}^{n-1} \Delta\theta_i}{\sum_{i=0}^{n-1} \Delta t_i} \quad (2)$$

where n is an integer, indicating the partial path of the travelling point on its trajectory. Initially the P position corresponds to $\theta = \theta_0$ for a time instant $t = t_0$; if t_0 and θ_0 are assumed zero, referring to equation (1), for a given time Δt_i , a $\Delta\theta_i$ will be defined.

Currently it is possible a time unit partition, by oscillator, of $1,0 \cdot 10^9$ [Hz]. If n , in equation (2), is 10^9 the angle of a complete turn can be subdivided in $1,0 \cdot 10^9$ parts with a $\Delta\theta_i$ amplitude of about $5,0 \cdot 10^{-9}$ radiant.

A logical scheme is shown in figure 3. This scheme shows two time sample elements indicated as CA and CB counters, working with a partition device and a constant multiplier.

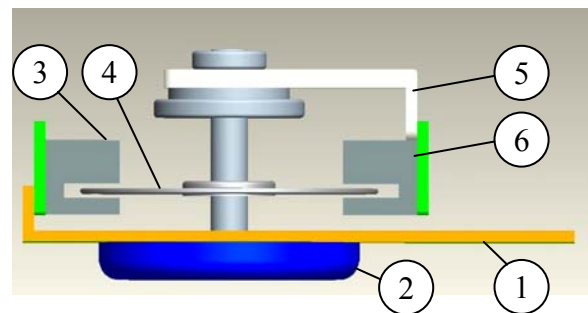


Figure 2 Schematic side view of the device.

The time sample elements have a unique wave generator and the motor is speed controlled in order to have a constant shaft motor speed. In general, the optical sensors and the target could be realised with a different basic principle, and the sensor until defined as fixed could be mobile.

In order to measure angles close to the complete round will be necessary to have two traces on different planes to avoid a physical overlapping of the two sensors. Being the motor in steady conditions, the fixed sensor is positioned along a reference direction representing the zero angle; the mobile sensor will be along the direction of the angle that must be measured.

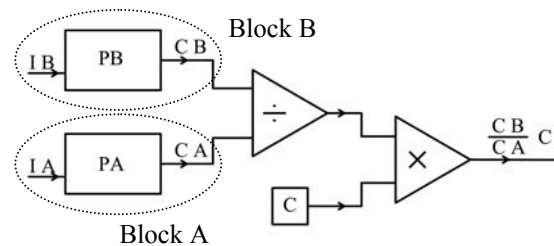


Figure 3 Logical scheme of the device.

The sensor (3), in figure 2, points out the target transit, starting the counter CA and CB, synchronised to the wave generator; later the sensor (6) detects the target transit and the counter B stops. Finally the second target transit on the sensor (3) stops the counter A.

The angle between the two direction of the two sensors respect to the motor shaft axis will be computed as:

$$\text{angle} = \frac{B \text{ numbering}}{A \text{ numbering}} \cdot K \tag{3}$$

where K constant depends on the angle units. The numbering of different particulars are the same in figure 2 and in the photograph of figure 4.

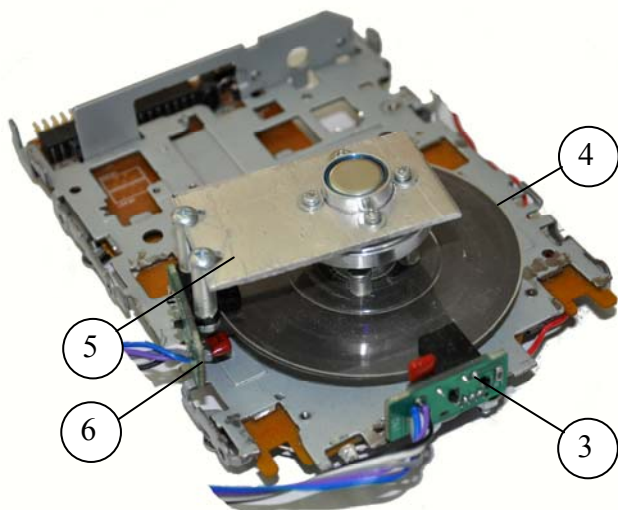


Figure 4 Photograph of the device.

3 THE TESTS AND THE ERROR EVALUATION

The tests conditions are chosen as significant and corresponding to those found in real working conditions. In particular, the tests environment is referred to standard ambient conditions.

During the performed tests, the motor runs with a reference rotating speed of 300 RPM. The square wave generator has a wave at 80 MHz. In the first round, for many angular positions of sensors (3) and (6), in figure 2 and 4, the counters CA and CB, represented in figure 3, will be reset to zero, when the target transits in front of sensors (3) and (6) respectively. Then the two numbering start at the same time corresponding to the CA reset, with the target in front of sensor (3). The two numbering CA and CB stop when the target transits in front of the two sensors.

At this time the divisor operator, represented in figure 3, divides the smaller numbering for the bigger one.

This data is multiplied for a constant to obtain the angular value. This allows an indirect angle measure between the angular position of sensors.

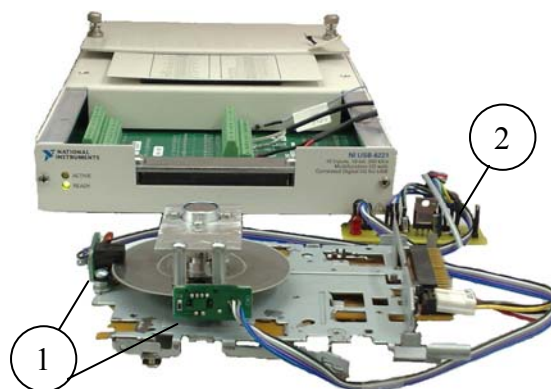


Figure 5 The plane angular measurement system with the data acquisition hardware.

The set up and the plane angular measurement system, with the data acquisition hardware, is shown in figure 5. In this photograph it can be seen the optical sensors (1) and the supply and conditioning system (2). These sensors generate a high-low signal reversing when the target transits in front of them.

The device is linked to a data acquisition hardware having an internal clock generating a square wave of 80 MHz. The software is an object-oriented programming system. An high frequency digital oscilloscope allows the control of the output clock signal of the hardware. The brushless motor, moving the disk, is supplied by an external controlled power unit. The signal commutation activates the time numbering as previous described.

The device resolution will be:

$$\frac{360^\circ}{80 \cdot 10^6} = 4.5 \cdot 10^{-6} = 0^\circ 0' 0,045'' \text{ sessadecimal} \tag{4}$$

i.e. $0^\circ 0' 0,027'' \text{ sessagesimal}$

This evaluation is relative to a clock frequency not so high; there are clocks having a frequency of some GHz, allowing a some more fine resolution. In any case the theoretical resolution is quite higher than that of the referring instrument.

The geometrical overall dimensions and mass of the device are referred in table I. These data are the actual dimensions of the tested device; in any case this kind of device allows smaller dimensions and masses keeping the resolution.

Table I - Dimensions and mass of the device.

length [mm]	140
width [mm]	100
thick [mm]	50
mass [gr]	250

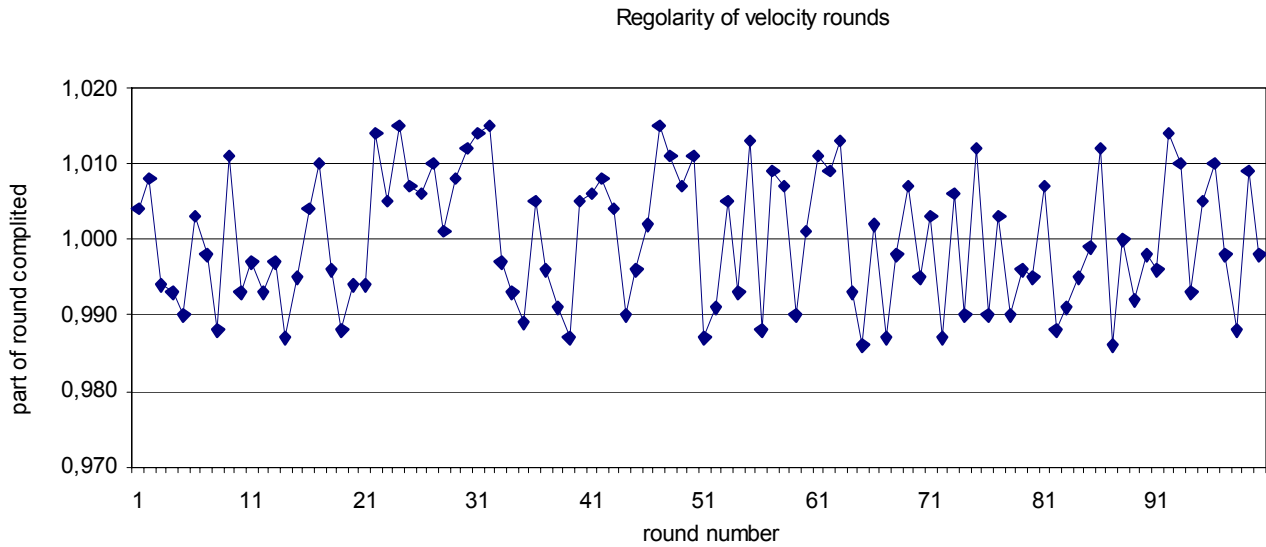


Figure 6 Rounds fulfilment referred vs. the round order number.

The uncertainty propagation evaluation, here proposed, will be performed referring to the [13]. This is a statistical approach to evaluate the uncertainty propagation for a variable G computed indirectly as a function of directly measured variables X, Y, Z, \dots

$$G = f(X, Y, Z, \dots) \quad (4)$$

The following equation will give the deviation value S_{G_M} :

$$S_{G_M} = \sqrt{\left(\frac{\partial G}{\partial x}\right)^2 S_{G_x}^2 + \left(\frac{\partial G}{\partial y}\right)^2 S_{G_y}^2 + \left(\frac{\partial G}{\partial z}\right)^2 S_{G_z}^2 + \dots} \quad (5)$$

where S_{G_M} is the mean standard deviation of the computed variable and the $S_{G_{x,y,z}}$ are the standard deviation of the directly measured variables. To perform this evaluation, will be necessary to know the uncertainty given in the device data sheet or estimated as in [13].

The equation, in steady condition, giving the angle amplitude θ , as a function of the angular velocity ω , and time interval Δt , is:

$$\theta = \omega \cdot \Delta t \quad (6)$$

The time interval Δt can be written as difference between instant time measuring:

$$\Delta t = t_2 - t_1 \quad (7)$$

where t_1 and t_2 are evaluated as number of times when a signal exceeds a given trigger level on a square wave (generated by the reference oscillator) started or stopped when the target crosses the optical sensors position.

The given variables values by the data sheet are the following:

Angular motor speed: 5 ± 0.05 rounds per second;

Clock of the system: $80 \pm 50 \cdot 10^{-5}$ MHz.

The uncertainty value of the computed angle θ will be then evaluated: this value turns out to be about one per cent of the read value.

The graph in figure 6 comes from tests of precision and constancy of the angular velocity on a 100 rounds range, using an high precision chronometer, represented by on board the clock, measuring the time interval between a turn and the following one. By this way it is possible to underline that: because of the realisation is workmanlike, the motor performs a system rotation motion with the precision declared by the FFD builder as in the referred data sheet. The data correspond to a mean of $5,0 \pm 5,0 \cdot 10^{-2}$ turns per second, having a standard deviation of $8,7 \cdot 10^{-3}$ turns per second.

Actually are available motors with a better regularity than that used in the present test, as described in the patent [14] using a spindle motor of a disk drive having a suitable architecture for this type of application: these devices are less subject to acceleration values. This type of devices could have a precision in the rotation of 0.1% instead of the 1.0% like those in this work. In the application discussed in this paper this fact will improve the precision value up to 0.1% more or less: i.e., the referring timing uncertainty is, in any case, significantly better; overall, in this case, the uncertainty in time measuring has not influence on the final indirect computed variable precision.

In figure 7 is represented a layout of the device actually in progress. It can be seen the fixed frame (1); the rotating motor, with constant angular speed (2); the shaft (3), driving the disk topographic theodolite like (4), with the target; the mobile frame (5), supporting the mobile sensor; the needle bearing (6); the support (7), of the fixed sensor.

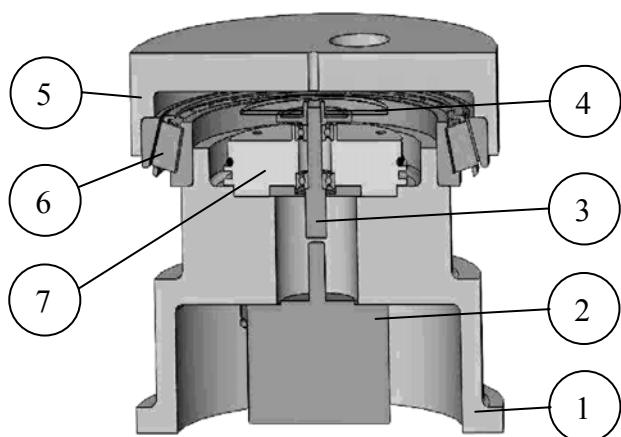


Figure 7 The layout of the new plane angular measurement system.

This architecture allows a better coaxially arrangement of the rotating elements and a useful rigidity of the transmission, with a higher constancy of the angular velocity.

6 CONCLUSIONS

An indirect angular measurement was performed by a special innovative device that allows to get a very high resolution system for Plane Angular Measurements. The resolution of the gauge corresponds to the expected one and the tests highlight that: the realised device has a very high resolution, but a low accuracy, as discussed in the paper. In particular, the low accuracy comes from a not sufficiently constant angular speed, compared to the clock uncertainty, although a workmanlike mechanical realisation. Other technologies are actually in progress to perform other way to upgrade the constancy of the angular velocity.

ACKNOWLEDGMENTS

The research was founded by the Italian Ministry of Research.

REFERENCES

- [1] Auckland D.W., Sundram S., Shuttleworth R., and Posner D. I., The measurement of shaft torque using an optical encoder, *J. Phys. E: Sci. Instrum.*, Vol.17, 1984.
- [2] Doebelin E. O., *Measurements System Application and Design*, McGRAW-HILL International Editions, 1990.
- [3] Doebelin E. O., *Strumenti e metodi di misura*, McGRAW-HILL ed. it. A. Cigada, 2008.
- [4] Engelhardt K., and Seitz P., High-resolution optical position encoder with large mounting tolerances, *Applied Optics*, Vol.36, No.13, 1 May, 1997.
- [5] Engelhardt K., and Seitz P., Absolute, high-resolution optical position encoder, *Applied Optics*, Vol.35. No.1, Jan. 1996.
- [6] Various Authors, Guide to the expression of uncertainty in measurement, *International Organization for Standardization*, Genève, 1995.
- [7] Kaye J.E., Balakrishnan S., Popplewell, N., and Menzies, R., High resolution adaptive tachometer for spindle motor drives, *Int. J. Electronics*, vol. 69, No.6, pp.835-848, 1990.
- [8] Orgen R., A high resolution optical shaft encoder, *Journal of the Institution of Electronics and Radio Engineers*, Vol.55, No.4, pp.133-138, April 1985.
- [9] Yeh W., High resolution optical shaft encoder for motor speed control based on an optical disk pick-up, *Review of scientific Instruments*, Vol. 69, No.8, August 1998.
- [10] Zaccariotto M., De Cecco M., Debeil S., Ricciu R. High resolution servomotor for space application. *International Journal of Mechanics and Control*, Vol. 07, pp. 41-49 ISSN: 1590-8844 - 2006.
- [11] Manuello Bertetto A., Ricciu R., Steinmetz D., sistema di misura assoluto per posizioni, velocità ed accelerazioni angolari ad elevata risoluzione, Italian Patent CA2009A000002, April 2009.
- [12] Manuello Bertetto A., Ricciu R., Steinmetz D., Plane Angular Measurement System for High Resolution Robotic Arm Positioning, Proc. of 18th International Workshop on Robotics in Alpe-Adria-Danube Region, May 25-27, 2009, Brasov, Romania.
- [13] UNI CEI ENV 13005: *Guide to the expression of uncertainty in measurement*, 1999.
- [14] Warren Jr. et all, Patent No. US 7,126,772 B1, October, 2006.

POSITION CONTROL OF XY PIEZO ACTUATED STAGE WITH NEURAL NETWORK USING STRUCTURAL GENETIC ALGORITHM

Jure Čas*

Dragan Kusić**

* Faculty of Electrical Engineering and Computer Science/Institute of Robotics, University of Maribor, Slovenia

** Faculty of Electrical Engineering and Computer Science/Institute of Automation, University of Maribor, Slovenia

ABSTRACT

This paper describes a position control of 2 degrees of freedom XY piezo actuator stage (XY PAS) with feedforward neural network (FNN) and additional structural genetic algorithm (SGA), which is used for the optimization of the neural network topology. XY PAS is fabricated by a photo structuring process from micro-structured photosensitive glass and two piezo actuators (PEAs), which are built-on to meet the request for its precise movement on the working plane with approximate dimensions 60 by 60 micrometres. It is evident from the simulation model of XY PAS, that accurate positional control is an exact piece of work. The FNN is used as adaptive feedforward controller describing the estimated inverse function of XY PAS for each reference position of XY PAS's tip. Due to the optimal control performance of FNN, the SGA is introduced in order to optimize the FNN topology. A simulation model of the XY PAS and the proposed FNN control algorithm with SGA have been developed in Matlab/Simulink.

Keywords: position control, simulation, piezo actuator stage, neural networks, structural genetic algorithm

1 INTRODUCTION

This Micro-robotics, due to its promising research results and growing employment in modern industry, is emerging as one of the most popular technical fields for current extensive exploration. The assembly of micro-components, such as optic components and micro-systems, requires new dedicated manipulators. They must have a submicron resolution and precision. Also they have to be reliable and compact. Moreover, they must be modular and flexible in order to accomplish several different micro-assembly tasks. Certain high-precision manipulators are also required for specific micro-machining and micro-positioning tasks.

PEAs, due to their nano-metre resolution, high stiffness, big driving force and fast response, are now recognized as fundamental elements for the actuation of robots, when managing extremely small displacements. However, their potential has been impaired by the adverse effects of highly-nonlinear hysteresis behaviour. This results in nonlinear and multi-valued mapping between the actuator's input and output and, hence, influences any desired control precision. Following this fact, an understanding of hysteresis behaviour is a fundamental step when designing the positional control of XY PAS.

In [1] authors approximated the hysteresis model by using motion dynamics constructed by an applied force to one set of mass-less bodies parallel to the springs, and the relationship in terms of applied force, spring constants and break forces is used to determine the hysteresis dynamics. However, from the given experimental results, it is difficult to determine the critical numbers of springs and mass-less bodies used to accurately represent the hysteresis dynamics. As a result, an electromechanical model is proposed [2], constructed by transduction of the electrical charge and discharge behaviours, in order to generate applied force. In

Contact author: Jure Čas¹, Dragan Kusić²

^{1,2} Address Faculty of Electrical Engineering and Computer Science/Institute of Robotics - Automation Smetanova ulica 17, 2000 Maribor, Slovenia.

E-mail: jure.cas@uni-mb.si
dragan.kusic@uni-mb.si

the mentioned study, the functions used for both shaping the hysteresis loop and describing the mechanical model of PEA were derived by using first order differential and partial differential equations, respectively. However, by means of this design method, the represented model of PEA is more suitable for vibration control than displacement control. The hysteresis effect inherent in the PEA is possible by collation using mechanical friction phenomena with included *Stribeck effect* [3]. Accordingly, the overall dynamics of PEAs, including characteristics of the *Stribeck effect*, hysteresis and spring-like behaviours, are assembled into mechanical motion dynamics [4].

Following these facts, an advanced control technique must be used for efficient positional control of XY PAS's tip. Those techniques based on neural networks, fuzzy logic and genetic algorithms belong to the group of soft computing control techniques. These techniques offer promising solutions for nonlinear control tasks, when implemented alone [5] or in combination [6]. Evolving FNN weights is the most common use of a SGA in conjunction with neural networks. Since genetic algorithms are excellent at searching a state-space, searching for neural network weights is an ideal application. The biggest trouble, when using genetic algorithms, is to specify the range of the weights. Since we generally do not know the range we have to estimate, we use a trail and error method to correct/optimize them. In this paper, a FNN control method with SGA is developed for positional control of a XY PAS tip. SGA is used in order to avoid local optimum of FNN, for FNN topology optimization and for FNN weights learning.

The paper is organized as follows. Section 2, describes the structure of XY PAS and the simulation model as derived for a better understanding of the control problem. Section 3 and section 4, describe FNN position control without and with SGA pre-learning. Section 5, shows the results of proposed position control techniques using the simulation model of XY PAS. Section 6, provides some conclusions.

2 DESCRIPTION OF XY PAS

The XY PAS is manufactured from a slice of photosensitive micro-structured glass with a thickness of 1 millimetre [7]. The photo structuring process with partial process steps UV-lithography, thermal treatment and etching, forms the basis for producing micro-structured glass components. The described process is based on different etching rates of exposed and non-exposed micro-structured glass. The slope angle of the etching walls is approximately 2.5 degrees and the structures have a repeatable precision of 5 micrometers. The developed XY PAS is very similar to a parallelogram in its mechanical construction. The working principle is shown by the ground plan view in Figure 1

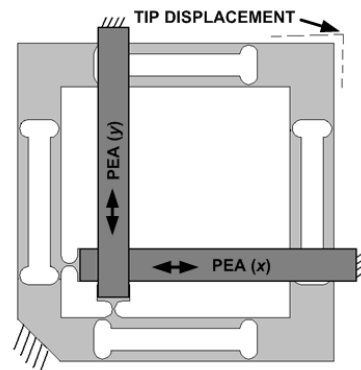


Figure 1 Schematic of XY PAS (ground-plan view).

Concerning the above figure, the displacement of PEAs is transmitted on the tip displacement of XY PAS. Two PEAs with dimensions 3 millimeters by 27 millimeters and with a thickness of 0.2 millimeters generate the desired micro-movement of XY PAS in two right-angled directions. The ground-plan size of XY PAS is approximately 40 millimeters by 40 millimeters. It is shown in Figure 2.

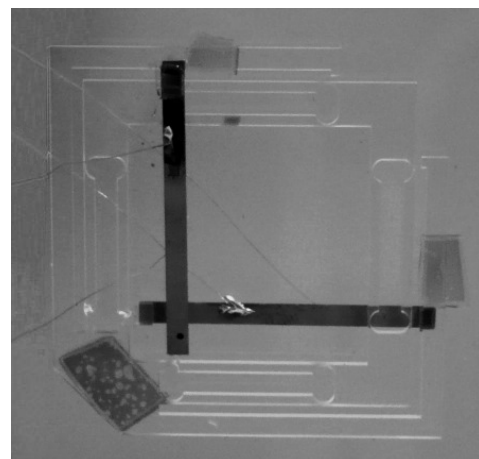


Figure 2 The photo of XY PAS.

The supply voltage value for the PEAs must be between the maximal voltage interval, i.e. the interval ± 100 volts. Any other supply voltage destroys the ceramic material of the PEAs. According to the maximum supply voltage, the displacement of unloaded PEAs is ± 3.3 micrometers. But the maximum displacement of the PEAs is not reached when they are joined to the XY PAS, because the XY PAS generates a reactive/opposite force similar to the force of the rotational spring.

Figure 3 shows a graph of displacement/force characteristic for XY PAS ($F_{XY\ PAS}$) and one PEA (F_{PEA}). When the maximum voltage of ± 100 volts is applied, the maximal displacement of PEA is ± 1.1 micrometers only.

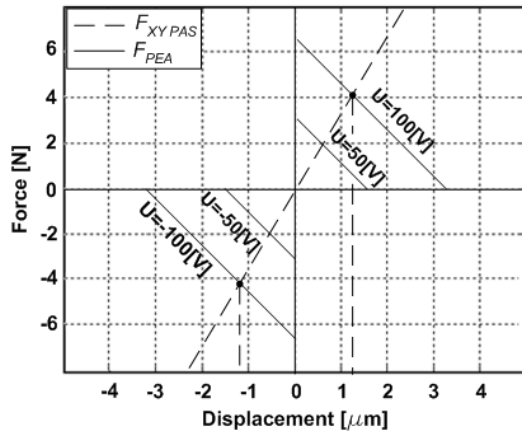


Figure 3 Displacement/Force characteristic of XY PAS and one PEA.

The XY PAS is designed in order to transmit the displacement of PEAs on the tip displacement of XY PAS. By the transmission rule, displacement of the PEAs is multiplied by a transmission ratio of $30/l$. The maximum tip displacement over one degree of freedom (DOF) is approximately ± 30 micrometres. Accordingly, the working area of XY PAS is square with 60 micrometre-long sides. The XY PAS model mostly depends on the hysteresis behaviour of the PEAs, which is very complex. For the purposes of controller-design, one of the most inconvenient aspects of the PEA's behaviour is the rate-dependent hysteresis exhibited between voltage and displacement, as well as between force and displacement. This type of behaviour can cause closed loop limited cycling, and possibly instability. A friction model with a hysteresis effect, called the *LuGre model* is, for 1-DOF, summarized as follows

$$\frac{d\bar{z}}{dt} = \dot{x} - \frac{|\dot{x}|}{h(\dot{x})} \bar{z}, \quad (1)$$

$$F_H = \sigma_0 \bar{z} + \sigma_1 \frac{d\bar{z}}{dt} + \sigma_2 \dot{x}, \quad (2)$$

where F_H denotes the hysteresis friction function, \bar{z} is interpreted as the contact force applied average bristle deflection, \dot{x} denotes the relative velocity between the two contact surfaces, σ_0 , σ_1 and σ_2 are positive constants that are typically unknown and difficult to identify and, in general, can be equivalently interpreted as bristle stiffness, bristle damping, and viscous damping-coefficient, respectively. Moreover, the function $h(\dot{x})$ denotes the *Stribeck effect curve*, given by

$$\sigma_0 h(\dot{x}) = f_c + (f_s - f_c) e^{-\frac{|\dot{x}|}{\dot{x}_s}}, \quad (3)$$

where f_c is the *Columb friction level*, f_s is the level of the stick force, \dot{x}_s is the *Stribeck velocity*. The hysteresis friction function can be further derived by using the following equation

$$F_H = \sigma_0 \bar{z} - \sigma_1 \frac{1}{h(\dot{x})} \bar{z} |\dot{x}| + (\sigma_1 + \sigma_2) \dot{x}, \quad (4)$$

Equation (5) is used to represent the overall dynamics of the XY PAS

$$m\ddot{x} + F_H + F_M + K_E U = 0, \quad (5)$$

where m denotes the equivalent mass of the XY PAS, x is the displacement of the PEA, \ddot{x} denotes the second-order derivative of the state x with respect to time, F_M is the reactive force of XY PAS, K_E denotes the voltage to force coefficient of PEAs and U denotes the applied voltage to PEA.

As mentioned previously, the reactive/opposite force is generated on PEA, when it is joined with a XY PAS. The XY PAS force value is described by

$$F_M = \frac{K_M \cdot \phi}{l} = \frac{K_M \cdot \arctan(x/l)}{l}, \quad (6)$$

where K_M is the rotational spring constant of the XY PAS, ϕ is the rotational angle of the spring, x is the displacement of the PEA and l is the torque arm. According to this, it is possible to include both disturbance forces (F_H and F_M) in Equation (5) to represent the overall dynamics of a XY PAS

$$\ddot{x} = \frac{K_E U}{m} - \frac{1}{m} \left[\begin{array}{c} \frac{K_M \cdot \arctan(x/l)}{l} + \sigma_0 \bar{z} - \\ -\sigma_1 \frac{1}{h(\dot{x})} \bar{z} |\dot{x}| + (\sigma_1 + \sigma_2) \dot{x} \end{array} \right]. \quad (7)$$

Two more equations are introduced due to the fact that this control method is designed for a tip displacement of XY PAS. By using Equation (8) and Equation (9), the displacement of PEA is multiplied by the transmission ratio to define the displacement of XY PAS tip, as follows

$$\ddot{x}_{ACT} = \ddot{x} \frac{L}{l}, \quad (8)$$

$$\ddot{y}_{ACT} = \ddot{y} \frac{L}{l}, \quad (9)$$

where \ddot{x}_{ACT} and \ddot{y}_{ACT} are accelerations of tip in two perpendicular directions and L/l is the transmission ratio of XY PAS. The final two equations for the simulation model of a XY PAS are, as follows

$$\ddot{x}_{ACT} = \frac{L}{l} \left[\frac{K_E U}{m} - \frac{1}{m} \left(\frac{K_M \cdot \arctan(x/l)}{l} + \sigma_0 \bar{z} - \sigma_1 \frac{1}{h(\dot{x})} \bar{z} |\dot{x}| + (\sigma_1 + \sigma_2) \dot{x} \right) \right], \quad (10)$$

$$\ddot{y}_{ACT} = \frac{L}{l} \left[\frac{K_E U}{m} - \frac{1}{m} \left(\frac{K_M \cdot \arctan(y/l)}{l} + \sigma_0 \bar{z} - \sigma_1 \frac{1}{h(\dot{y})} \bar{z} |\dot{y}| + (\sigma_1 + \sigma_2) \dot{y} \right) \right]. \quad (11)$$

The values of the designed parameters are defined as follows:

$$\begin{aligned} \sigma_0 &= 1 \cdot 10^6 \left[\frac{N}{m} \right], \quad \sigma_1 = \sqrt{1 \cdot 10^6} \left[\frac{Ns}{m} \right], \quad \sigma_2 = 0.2 \left[\frac{Ns}{m} \right], \\ F_c &= 1.2 [N], \quad F_s = 2 [N], \quad x_s = 0.001 \left[\frac{m}{s} \right], \quad m = 0.005 [kg], \\ K_E &= 0.064 \left[\frac{N}{V} \right], \quad K_M = 5.08 \left[\frac{Nm}{rad} \right], \quad l = 0.001 [m], \\ L &= 0.03 [m]. \end{aligned}$$

According to the derived equations, the XY PAS is a non-linear system due to the integrated hysteresis in PEAs and the dynamics of XY PAS. Figure 4 shows a graph of the tip displacement/supply voltage characteristic. Only the x_{ACT} displacement is shown for the sake of convenience.

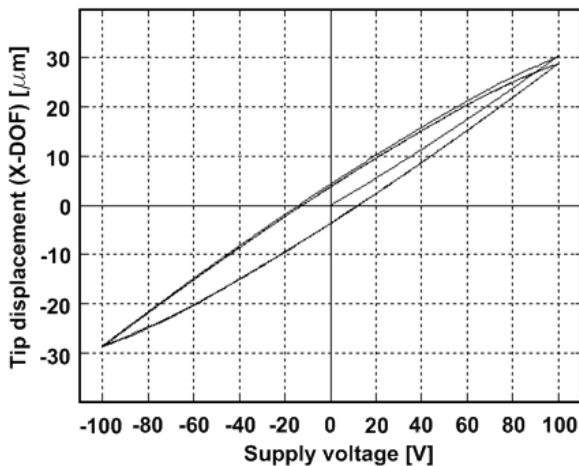


Figure 4 Tip displacement/Supply voltage graph (simulation result).

The supply voltage, which was used in the simulation, can be described by the equation

$$U_x(t) = 100 \sin(2t), \quad (12)$$

where t stands for simulation time.

3 DESCRIPTION OF FNN CONTRLLER

The key attribute of neural networks is their ability to serve as a general nonlinear model. It has been shown that any function of practicable interest can be arbitrarily approximated closely by a neural network having enough neurons, at least one hidden layer and an appropriate set of weights [8]. The high-speed of computation and general modeling capabilities of neural networks are very attractive properties for nonlinear compensation problems, such as XY PAS with non-linear hysteresis inherent in PEAs.

The basic of the proposed FNN controller is backpropagation (BPG) algorithm, which is designed to minimize the difference between the desired and the actual outputs from the FNN, called an "error". If an error is defined as the difference between the reference and the actual value of the XY PAS tip coordinates, the BPG algorithm will minimize that difference. Figure 5 shows a control scheme of proposed FNN position control of XY PAS.

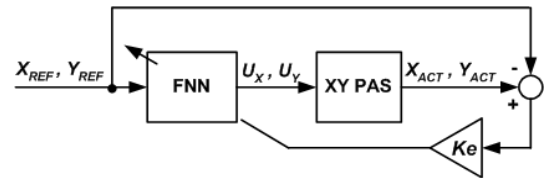


Figure 5 Block scheme of FNN controller.

The proposed FNN has three layers of neurons, where m is the number of neurons in the input layer, n is the number of neurons in the hidden layer and r is the number of neurons in the output layer. While the number of neurons in the input and output layers is determined to value four and two, the number of neurons in the hidden layer is able to change by achieving the optimal result of the controller. In the following equations, the character I is in accordance with the input layer of FNN, the character J is in accordance with the hidden layer of FNN and the character L is in accordance with the output layer of FNN. The input layer of FNN is defined

$$I_{IN} = \{X_{REF}, Y_{REF}\}^T, \quad (13)$$

where X_{REF} and Y_{REF} are reference coordinates of the XY PAS's tip. X_{ACT} and Y_{ACT} are actual coordinates of the XY PAS's tip. The transfer function of the hidden layer is a elementary sigmoid function

$$S_J(netJ) = \frac{1}{1 + e^{-netJ}}. \quad (14)$$

The transfer function of the output layer is the derivative of the elementary sigmoid function and is described as follows

$$S_L(\text{net}L) = -100 + \frac{200}{1 + e^{-4\text{net}L}}. \quad (15)$$

By Equation (15) the possible output value of FNN is in interval ± 100 . As it can be seen from the control scheme in Figure 5, the output value of FNN is, as a matter of fact, the supply voltage. As previously discussed, the maximal-allowed value of supply voltage for PEAs is in interval ± 100 volts.

The known feedforward method for calculating the output of FNN is described as follows

$$\begin{aligned} \text{net}_J(j) &= \sum_{i=1}^m (w_{Jij} \cdot \text{In}_i); \text{ for } j = 1 \dots n, \\ J_{OUT}(j) &= S_J(\text{net}_J(j)); \text{ for } j = 1 \dots n, \\ \text{net}_L(l) &= \sum_{j=1}^n (w_{Ljl} \cdot J_{OUT}(j)); \text{ for } l = 1 \dots r, \\ L_{OUT}(l) &= S_L(\text{net}_L(l)); \text{ for } l = 1 \dots r, \end{aligned} \quad (16)$$

where w_{Jij} and w_{Ljl} are weight values for the hidden and output layers of FNN.

The BPG algorithm is designed to minimize the difference between the desired and the actual output from the FNN. If the difference is defined as vector

$$e = K_e \left\{ (X_{REF} - X_{ACT}), (Y_{REF} - Y_{ACT}) \right\}^T, \quad (17)$$

where K_e is the error constant. The influence of an error constant on controller step response is similar to the influence of the proportional part, when considering the traditional PI controller. The BPG algorithm will minimize the defined error over the whole time of the control. The output from FNN is the desired supply voltage. The traditional BPG algorithm is defined as follows. The variation value of the output weights is calculated by Equation (18)

$$\Delta w_{Ljl}^p = \varepsilon_L \cdot e(l) \cdot \dot{S}_L(l) \cdot J_{OUT}(j), \quad j = 1 \dots n \text{ and } l = 1 \dots r \quad (18)$$

where ε_L is the learning rate constant of the output layer and $\dot{S}_L(l)$ is the derivative of $S_L(l)$. After calculating the weight's variations, the new values of weights in output layer are calculated as follows

$$w_{Ljl}^p = \Delta w_{Ljl}^p + w_{Ljl}^{p-1}, \quad (19)$$

where w_{Ljl}^p is the new calculated value of the weight and w_{Ljl}^{p-1} is the last calculated value of the weight in the output layer. After the new values of weights in the output layer are calculated, the variations of weights in the hidden layer are calculated by Equation (20)

$$\begin{aligned} \Delta w_{Jij}^p &= \varepsilon_J \cdot \dot{S}_J(j) \cdot \sum_{l=1}^r (e(l) \cdot \dot{S}_L(l) \cdot w_{Ljl}) \cdot I_{IN}(i), \\ &\text{for } i = 1 \dots m \text{ and } j = 1 \dots n, \end{aligned} \quad (20)$$

where ε_J is the learning rate for the hidden layer and $\dot{S}_J(j)$ is the derivative of $S_J(j)$. After calculating the weights variations, the new weights in the hidden layer are as follows

$$w_{Jij}^p = \Delta w_{Jij}^p + w_{Jij}^{p-1}, \quad (21)$$

where w_{Jij}^p is the newly calculated weight and w_{Jij}^{p-1} is the last calculated weight from the hidden layer.

4 DESCRIPTION OF FNN CONTRLLER WITH SGA

Although the neural networks are easy to implement, we often have a learning problem with neural networks weights in order to avoid the local optimums during the learning process. To solve this problem, we used additional SGA together with FNN for position control of XY PAS.

The basic principle of SGA is to define the chromosome as a hierarchical structure. Activation and performance of low level genes is therefore lead by those nodes that are on higher level. All those inactivated genes provide the additional information, which enables the SGA reaction to a changing environment.

SGA has been developed and improved as a structural optimizer. In our case only one type of optimizer for control applications is especially important, i.e. the FNN topology optimiser.

The SGA gives us the possibility to solve the solution structure and solution parameter problems at the same time by means of genetic algorithm [9]. Figure 6 shows how a structural genetic algorithm is used for neural network optimisation.

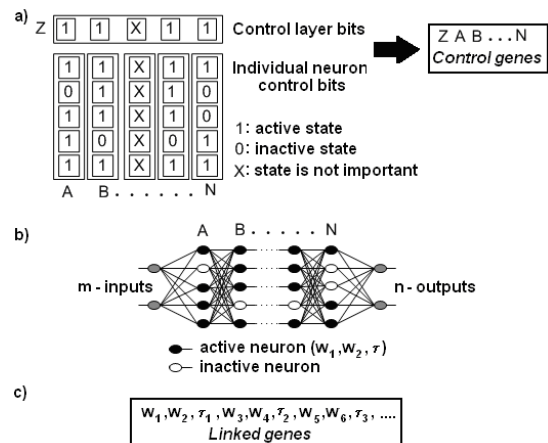


Figure 6 SGA for FNN optimization: a-Control genes, b-FNN topology with regard to control genes, c-Linked genes.

The important advantage of genetic algorithms is their possibility of solving optimization problems, which can be described with the chromosome encoding. Encoding chromosomes with genes, which are binary digits, i.e. bits 0 or 1, is the most expanded presentation of a chromosome, because it is simple and traceable. In our case we presented each chromosome as a binary set, which is 30 bits long.

As it is seen from Figure 6, chromosome is divided into control genes and linked genes. Control genes are further divided into control layer bits and individual neuron control bits in the FNN layer [10].

When an individual neuron control bit has logic 1, then the neural network layer or a matching neuron exists in the layer, and vice versa for a control bit set to logic 0. Value X means that the value (logical 0 or 1) is unimportant. Linked genes represent individual neuron weight values and thresholds, which connect this neuron to the previous layer. The genetic algorithm of the optimisation over genes, structured as we mentioned above, is classical. Some disadvantages appear, when using SGA in real-time control applications. Firstly, we are always limited because of the random solutions and achieved convergence, and secondly, the computation speed of SGA is very low. Therefore, it is unreasonable to use genetic algorithms for on-line control applications in real time systems without testing them on a simulation model.

Accordingly, the results obtained by SGA from offline learning process can be used in on-line control as an initial structure of FNN. As we mentioned previously, we used SGA to reach the optimal topology of FNN and for weights initialization. The basic working procedure of developed SGA starts with initially randomly generated weights. The choosed starting population is equal 10 and remains unchanged during the whole procedure.

All populations evolve in accurately 300 iterations through selection of parent solutions and then reproduction (crossover and mutation). In each iteration, one half of the whole population is eliminated, which gave us then worst results compared to the given fitness function. The fitness function is therefore calculated by Equation (22)

$$ff = e_1 \times (1 - M_o) + e_2 \times (1 - T_r) + e_3 \times (1 - E_{ss}), \quad (22)$$

where e_1 , e_2 and e_3 are constants which are equal 1/3, T_r is the rising time, M_o is the overshoot value (in percentage) and E_{ss} is the static error value.

5 SIMULATION RESULTS

The proposed neural network based control method has been tested in Matlab/Simulink with the developed SGA, and by using simulation model of XY PAS. Tests were made without and with SGA for different values of error constant, learning rate values and the number of neurons. It was discovered, that the best response is reached when using the values of FNN parameters as follows: $K_e = 20$,

$m = 16$, $\varepsilon_J = 0.04$ and $\varepsilon_L = 0.04$. Secondly, we made a few tests by including our SGA, where the fitness function has been calculated by Equation (22). We can insert into the fitness function all 3 desired parameters (T_r , M_o and E_{ss}). The task of the SGA is to reach those objectives by learning and optimizing the topology of the FNN. Our aim was to scientifically improve the supply voltage response and the position control of the XY PAS.

Figure 7 shows the step response of the proposed FNN controller without (X_{ACT} without SGA) and with SGA (X_{ACT} with SGA). After the SGA completed its task, we optimized the topology of the proposed FNN by disabling the links between the neurons in hidden layer and both FNN outputs. This was reached by eliminating those links with absolute weights value less than 0.030. For the X-DOF we could reduce 9 links (between the neurons in hidden layer and first FNN output) and for Y-DOF we could reduce 11 links (between the neurons in hidden layer and second FNN output).

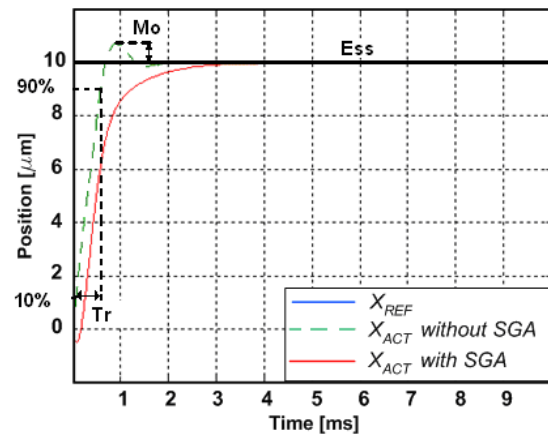


Figure 7 Position control of XY PAS (reference value, actual value without and with usage of SGA).

We managed to assure here that all 3 parameters (T_r , M_o and E_{ss}) are within desired values. For the sake of convenience, only the reference position (X_{REF}) and actual/controlled positions of X-DOF are shown. The reference value is changed to 10 micrometers and the error is minimized in less than 4 milliseconds.

As we can see from Figure 8, the first test with included SGA shows the improved voltage response. We used only one hidden layer with 30 neurons and the number of FNN inputs and outputs is the same as before. The goal of experiment was to assure the step response rising time less than 1 millisecond, without overshoot and eliminated static error. Previously discussed, FNN outputs are equal to the driving voltages of PEAs. For the sake of convenience, only the X-DOF driving voltage of PEA is shown. The second output of FNN presents the Y-DOF driving voltage of the XY-PAS.

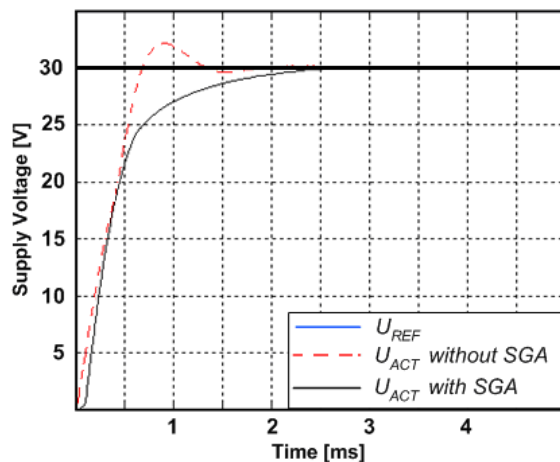


Figure 8 Position control of XY PAS (Supply voltage I).

Next experiment with SGA was also successfully completed (Figure 9). The desired rising time of step response was less than 2 milliseconds, with overshoot 5 % and without static error. We used 2 hidden layers with 15 neurons in each. It turned out that such suggested architecture is useless since we could eliminate only 5 links between the second hidden layer and output of FNN.

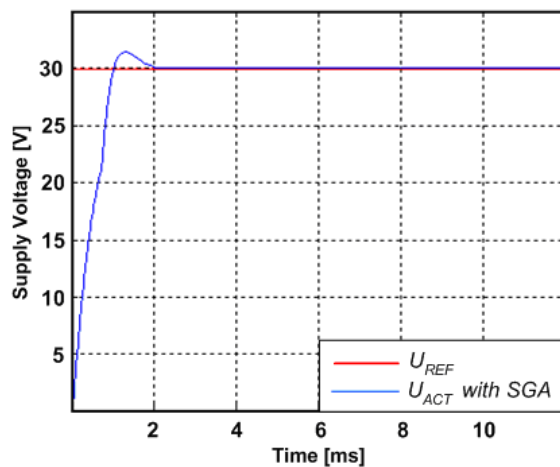


Figure 9 Position control of XY PAS (Supply voltage II).

6 CONCLUSION

As can be seen from the simulation results, the proposed FNN adaptive controller is appropriate for positional control of XY PAS. FNN presents the inverse function of the XY PAS for every reference position, and it is computed by the BPG algorithm. We used SGA in order to repair the random initialization of FNN topology and neuron connections. As a result, we achieved the reduced computing time of inverse function for every reference position and as consequence more accurate position control of XY PAS.

Due to the fact that SGA is very slow, it is not appropriate for on-line controls in real time systems. However, results obtained in off-line mode can be used for neural network topology optimization and for initialization of learning process in on-line mode. Those two things are the main reasons to consider the development of SGA. In the future the proposed control technique will be used in real control application.

REFERENCES

- [1] Goldfarb M. and Celanovic N., Modeling Piezoelectric Stack Actuators for Control of Micromanipulation. *IEEE Control Systems Magazine*, Vol. 17, No. 3, pp. 69-79, 1997.
- [2] Adriaens H.J.M.T.A., de Koning W.L. and Banning R., Modeling Piezoelectric Actuators. *IEEE/ASME Transactions on Mechatronics*, Vol. 5, No. 4, pp. 331-341, 2000.
- [3] de Wit C.C., Olsson H., Astrom K. J. and Lischinsky P., A New Model for Control of Systems with Friction, *IEEE Transactions on Automatic Control*, Vol. 40, No. 3, pp. 419-425, 1995.
- [4] Lin F.-J., Shieh H.-J., Huang P.-K. and Teng L.-T., Adaptive Control with Hysteresis Estimation and Compensation Using RFNN for Piezo Actuator. *IEEE Transactions on Ultrasonic, Ferroelectrics and Frequency Control*, Vol. 53, No. 9, pp. 1649-1661, 2006.
- [5] Yu S., Shirinzadeh B., Alici G. and Smith J., Sliding Mode Control of a Piezoelectric Actuator with Neural Network Compensating Rate-Dependent Hysteresis. *Proceedings of the 2005 IEEE International Conference on Robotics and Automation*, Barcelona-Spain, pp. 3641-3645, 2005.
- [6] Bai R. and Li H., Genetic Algorithm Neural Network Model Based on Coke Oven Gas Collector Pressure System. *Proceedings of the 7th World Congress on Intelligent Control and Automation*, Chongqing-China, pp. 1992-1995, 2008.
- [7] Kerschkerjan R., Qiao F. and Wurmus H., Piezoelectric X-Y-Micropositioner Made of Photosensitive Glass to Form One Micro-handling Unit. *Actuator 2000*, Bremen-Germany, pp. 296-299, 2000.
- [8] Hornik K., Stinchcombe M. and White H. Multilayer Feedforward Networks are Universal Approximator. *Neural Networks*, Vol. 2, pp. 359-366, 1989.
- [9] Davis L., *Handbook of Genetic Algorithms*. 1st edition, Van Nostrand Reinhold Company, 1991.
- [10] Tang K.S., Chan C.Y., Man and Kwong S., Genetic Structure for NN Topology and Weights Optimization. *1st International Conference on Genetic Algorithms in Engineering Systems: Innovations and Applications*, Sheffield-UK, pp. 250-255, 1995.

DYNAMIC ANALYSIS OF THE I.CA.RO. PARALLEL MANIPULATOR

Massimo Callegari Luca Carbonari Matteo-Claudio Palpacelli

Department of Mechanics, Polytechnic University of Marche, Italy

ABSTRACT

The present article is taken from a paper presented at the 18th RAAD International Workshop and discusses the dynamic model of the I.Ca.Ro. Cartesian Parallel Manipulator, a research parallel kinematics machine (PKM) with 3-CPU architecture which is capable of motions of pure translation: the modelling of robot's dynamics has been performed by means of the principle of virtual works and several computer simulations allowed a thorough study of its dynamic behaviour. The first experimental tests have shown the effectiveness of the model even if further investigations have to be undertaken to account for friction and joint deflections.

Keywords: Robot, Parallel kinematics machine, Dynamics model, Multibody system

1 INTRODUCTION

A parallel robot based on the 3-CPU concept, named I.Ca.Ro. (Innovative CARTesian RObot), has been designed and prototyped by Callegari and Palpacelli [1]. Its kinematic and static properties are very good, mainly due to the "Cartesian" arrangement of the structure, that grants a decoupling of the velocity mapping: the convex workspace is wide and free of singularities and the constancy of the Jacobian matrix yields a constant stiffness and accuracy of positioning in every point.

The simple kinematics of the machine suggests that model-based control schemes should be pursued in order to exploit its dynamics capabilities, especially in case task-space controllers are implemented. To this aim, robot's dynamics has been studied and a closed-loop dynamic model of the machine has been eventually worked out, as described in the present paper.

Many approaches have been experimented in recent years by robotics researchers to yield efficient dynamic models: in fact, especially in case inverse dynamics models are used for real-time control, the efficiency of the computation is of paramount importance; on the other hand, modelling of parallel manipulators usually presents an inherent complexity, mainly due to system closed-loop structure and kinematic constraints.

The traditional Newton-Euler formulation has been widely used in robot mechanics since many years [2-3] but it is still presently used by some researchers [4-5]. The Lagrange equations are maybe the most popular approach for modelling manipulator chains and many researchers have experimented them in past years [6-8]. As a matter of fact, all main classical mechanics principles have been experimented in past years, including Kane's equations [9], a generalized momentum approach [10], Hamilton's principle [11] and the principle of virtual work [12]. In parallel, many mathematic methods such as screw theory [13], Lie algebra [14], natural orthogonal complement [15-16] have also been adopted to the dynamics of parallel manipulators.

In 1993 Zhang and Song proposed the use of the d'Alembert's principle of virtual work for the inverse dynamic modelling of open-loop manipulators [12], then in 1998 Wang and Gosselin [17] first applied the method to parallel kinematics machines: since then, many researchers used it, especially for the modelling of closed-loop kinematic chains [18-20], due to its computational efficiency.

In fact, even if all methods lead to equivalent dynamic equations, these equations present different levels of complexity and associated computational loads; minimize the number of operations involved in the computation of the manipulator dynamic model has been the main goal of recently proposed techniques [21]: since by the use of the virtual work principle constraint forces and moments do not need to be computed, this approach leads to faster computational algorithms, which is a very important advantage for the purpose of robot control.

Contact author: Massimo Callegari¹

¹ E-mail: m.callegari@univpm.it

URL: <http://www.dipmec.univpm.it/meccanica/>

2 DESCRIPTION OF THE PROTOTYPE

The 3-CPU translating parallel manipulator is made up of three legs with a serial CPU kinematics, namely Cylindrical, Prismatic and Revolute joints, that connect the fixed base to the moving platform as shown in figure 1. Robot's kinematics has been fully investigated [1] and its dynamic behaviour has been studied by means of multibody simulations in a virtual prototyping environment. The research hereby presented aims at characterising robot's dynamics also in view of the following design of robot's controller. Robot's kinematics is here shortly recalled together with the definition of the main reference systems that have been used for the development of the dynamic model.

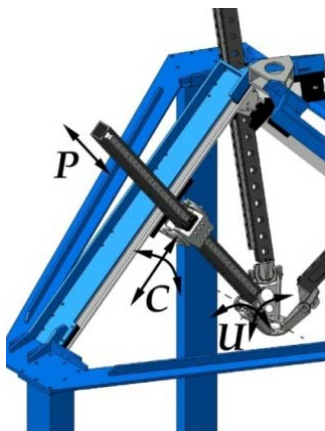


Figure 1 Leg's kinematics of the 3-CPU translating parallel manipulator

Figure 2 shows the sketch of i^{th} leg (represented upside down with respect to the actual configuration of the prototype) where $O(x,y,z)$ represents the global Cartesian frame and $P(u,v,w)$ the frame located on the moving platform: such two frames maintain the same orientation during machine's motion.

A local frame D_i for each leg can also be defined after a couple of rotations, starting from the global frame, a translation and a further rotation: the first around the z axis by a clockwise angle φ_i , with $\varphi_1 = 0^\circ$, $\varphi_2 = 120^\circ$ and $\varphi_3 = 240^\circ$ for the three kinematic chains, the second one around the current y axis by the counterclockwise rotation α , then a translation a_i along the current x axis and eventually the last rotation around the local x axis by the clockwise angle θ_i . The mentioned z and y rotations are constant and define the directions of the orthogonal sliding axes of the cylindrical pairs, whose unit vectors are indicated with \hat{a}_i for $i=1,2,3$, while the last angle refers to the rotation of the generic leg with respect to the mentioned sliding axis. The direction of the middle prismatic pair of each leg is represented by the unit vector \hat{d}_i that has been chosen passing through the leg's center of mass; to this aim a constant vector s_i ,

orthogonal to both \hat{a}_i and \hat{d}_i , has been considered to shift the vectors \hat{d}_i . In figure 2 the parameter c represents the distance of the center of mass from the end of the leg where the universal joint connects the leg itself with the moving platform; even in this case a constant shift, this time in the opposite direction with respect to s_i , is required to reach the point where the universal joint is physically placed. A constant vector t_i parallel to \hat{a}_i , but in the opposite direction, brings to the origin of the reference system $P(u,v,w)$ in common with the three kinematic chains.

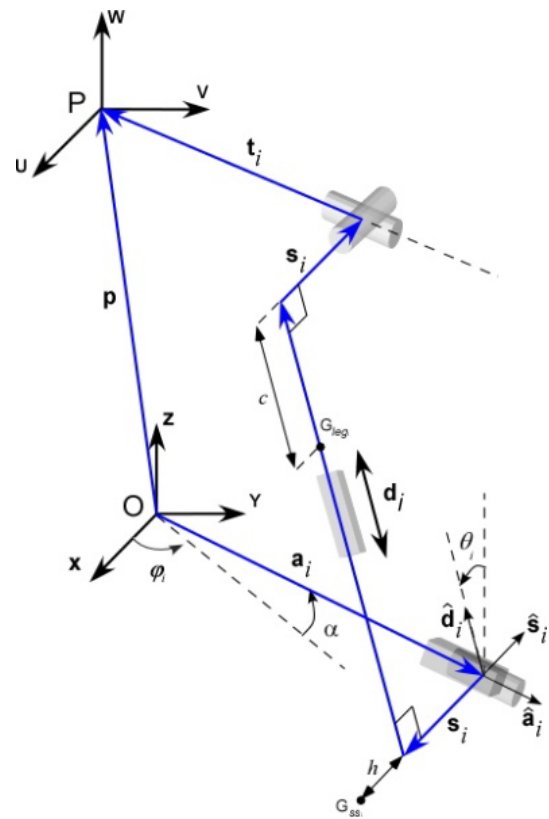


Figure 2 Sketch of the i^{th} leg of the I.Ca.Ro. robot.

2.1 DIRECT AND INVERSE KINEMATICS

A loop closure equation can be defined for each i^{th} leg in the global Cartesian frame as follows:

$$p = a_i + d_i + t_i \tag{1}$$

where p represents the position of the moving platform, namely the origin of the frame $P(u,v,w)$.

Gathering together the equations (1) for $i=1,2,3$, and collecting the magnitudes a_i , namely the slidings of the carriages of the ball bearing guides at the base, as a function of the moving platform position $p = (p_x, p_y, p_z)$, the solution of the *inverse kinematics problem* is easily worked out:

$$a_i = c\varphi_i c\alpha \cdot p_x + s\varphi_i c\alpha \cdot p_y + s\alpha \cdot p_z + t_i \quad (2)$$

The inversion of (2) provides the solution of the *direct kinematics problem*; its time derivative, written three times for $i=1,2,3$, provides the velocity kinematics mapping between task space and joint space; it can be expressed in the usual compact form:

$$\dot{\mathbf{a}} = \mathbf{J}_p \dot{\mathbf{p}} \quad (3)$$

where \mathbf{J}_p is the 3x3 constant *Jacobian matrix of the robot*:

$$\mathbf{J}_p = \begin{bmatrix} \hat{\mathbf{a}}_1^T \\ \hat{\mathbf{a}}_2^T \\ \hat{\mathbf{a}}_3^T \end{bmatrix} = \begin{bmatrix} c\varphi_1 c\alpha & s\varphi_1 c\alpha & s\alpha \\ c\varphi_2 c\alpha & s\varphi_2 c\alpha & s\alpha \\ c\varphi_3 c\alpha & s\varphi_3 c\alpha & s\alpha \end{bmatrix} \quad (4)$$

2.2 KINEMATIC PROPERTIES

The I.Ca.Ro. robot presents a wide convex workspace of 0.275 m^3 : its shape is given by a cube, placed within the fixed frame, as shown in figure 3. The sides of the cube have a length of 0.65 m provided by the strokes of the cylindrical joints, namely by the sliding of the carriage of the linear modules.

Robot kinematics is very simple, yielding an isotropic workspace; moreover the constancy of the Jacobian matrix makes the robot's workspace free from singularities.



Figure 3 Cubic workspace of the I.Ca.Ro. robot.

2.3 JACOBIAN MATRICES OF THE LIMBS

System (3) shows the relation between the velocity of the actuated joints and the moving platform: similarly the velocities of the limbs can be expressed as a function of $\dot{\mathbf{p}}$ by means of the corresponding Jacobian matrices.

To this aim the legs have to be divided into three members: the main part of the leg, made up of a metal hollow bar provided with the rail of the prismatic joint and, at its upper end, the hinge of the U-joint, the swinging support, given by a small part that spins around the axis of the cylindrical pair together with the slide of the prismatic joint, and the carriage, that takes into account all the masses rigidly connected with the slide of the linear modules.

The velocities of the three mentioned members can be easily obtained by deriving the position vectors of their centers of mass:

$$\begin{aligned} \mathbf{r}_{leg_i} &= a_i \hat{\mathbf{a}}_i - s \hat{\mathbf{s}}_i + (d_i - c) \hat{\mathbf{d}}_i \\ \mathbf{r}_{ss_i} &= a_i \hat{\mathbf{a}}_i - (s + h) \hat{\mathbf{s}}_i \\ \mathbf{r}_{car_i} &= a_i \hat{\mathbf{a}}_i + m \hat{\mathbf{s}}_i + n \hat{\mathbf{d}}_i \end{aligned} \quad (5)$$

therefore obtaining:

$$\begin{aligned} \mathbf{v}_{leg_i} &= \dot{a}_i \hat{\mathbf{a}}_i - s \boldsymbol{\omega}_i \times \hat{\mathbf{s}}_i + \dot{d}_i \hat{\mathbf{d}}_i + (d_i - c) \boldsymbol{\omega}_i \times \hat{\mathbf{d}}_i \\ \mathbf{v}_{ss_i} &= \dot{a}_i \hat{\mathbf{a}}_i - (s + h) \boldsymbol{\omega}_i \times \hat{\mathbf{s}}_i \\ \mathbf{v}_{car_i} &= \dot{a}_i \hat{\mathbf{a}}_i \end{aligned} \quad (6)$$

The term $(s + h)$ locates the center of mass of the swinging support with respect to the sliding axis of the carriage, as shown in figure 2, while m and n define the position of the center of mass of the carriage; the last terms will not affect robot's dynamic because the slides only translate along the direction given by $\hat{\mathbf{a}}_i$.

By expressing the velocities (6) in the local frame \mathbf{D}_i as a function of $\dot{\mathbf{p}}$, the Jacobian matrices of the limbs are readily defined:

$$\mathbf{D}_i \mathbf{v}_{leg_i} = \begin{bmatrix} \hat{\mathbf{a}}_i^T \\ \left(\frac{d_i - c}{d_i} \right) \hat{\mathbf{s}}_i^T \\ \frac{s}{d_i} \hat{\mathbf{s}}_i^T + \hat{\mathbf{d}}_i^T \end{bmatrix} \dot{\mathbf{p}} \quad (7)$$

$$\mathbf{D}_i \mathbf{v}_{ss_i} = \begin{bmatrix} \hat{\mathbf{a}}_i^T \\ \mathbf{0}^T \\ \left(\frac{s + h}{d_i} \right) \hat{\mathbf{s}}_i^T \end{bmatrix} \dot{\mathbf{p}} \quad (8)$$

$$\mathbf{D}_i \mathbf{v}_{car_i} = \begin{bmatrix} \hat{\mathbf{a}}_i^T \\ \mathbf{0}^T \\ \mathbf{0}^T \end{bmatrix} \dot{\mathbf{p}} \quad (9)$$

2.4 ACCELERATION ANALYSIS

In order to provide all the kinematic relations necessary to the definition of the analytical dynamics model of the robot, the linear accelerations of the moving platform, together with the linear and angular acceleration of the legs are needed.

A time derivative of (3) provides the linear acceleration $\ddot{\mathbf{p}}$ of the moving platform:

$$\ddot{\mathbf{a}} = \mathbf{J}_p \ddot{\mathbf{p}} \quad (10)$$

Finally the acceleration of the generic leg, swinging support and carriage can be worked out by deriving their velocity expressions (6), providing:

$$\begin{aligned} \dot{\mathbf{v}}_{leg_i} &= \ddot{a}_i \hat{\mathbf{a}}_i + 2\dot{d}_i (\boldsymbol{\omega}_i \times \hat{\mathbf{d}}_i) + \ddot{d}_i \hat{\mathbf{d}}_i + (d_i - c) \dot{\boldsymbol{\omega}}_i \times \hat{\mathbf{d}}_i + \\ &\quad + (d_i - c) \boldsymbol{\omega}_i \times (\boldsymbol{\omega}_i \times \hat{\mathbf{d}}_i) - s [\dot{\boldsymbol{\omega}}_i \times \hat{\mathbf{s}}_i + \boldsymbol{\omega}_i \times (\boldsymbol{\omega}_i \times \hat{\mathbf{s}}_i)] \\ \dot{\mathbf{v}}_{ss_i} &= \ddot{a}_i \hat{\mathbf{a}}_i - (s + h) [\dot{\boldsymbol{\omega}}_i \times \hat{\mathbf{s}}_i + \boldsymbol{\omega}_i \times (\boldsymbol{\omega}_i \times \hat{\mathbf{s}}_i)] \\ \dot{\mathbf{v}}_{car_i} &= \ddot{a}_i \hat{\mathbf{a}}_i \end{aligned} \quad (11)$$

3 DYNAMICS MODEL

The knowledge of the analytical relation between the torques of the actuated joints and the manipulator's law of motion is of noteworthy importance both for the feasibility verification of a given trajectory and for the definition of control algorithms able to compensate the non-linearities that intrinsically characterise mechanical systems.

In the present study the direct dynamics problem has been dealt with the help of simulation tools: a virtual model of the robot has been built inside the multibody software Virtual.Lab (by LMS) and several tests have been performed by interfacing it with Simulink/Matlab (by Mathworks). By means of these software packages robot's dynamic equations have been integrated, by using different numerical techniques for Ordinary Differential and Differential Algebraic Equations.

As for inverse dynamics, the approach based on the principle of virtual works and the concept of link Jacobian matrices has led to a simple and compact form of the equations and to efficient computer algorithms for their evaluation.

3.1 INVERSE DYNAMICS MODEL OF I.CA.RO.

According to the principle of virtual works, the following equation has to be satisfied for the translating robot:

$$\delta(\mathbf{a})^T \boldsymbol{\tau} + \delta(\mathbf{p})^T \mathbf{f} + \sum_{i=1}^3 \left(\sum_{j=1}^3 \left(\delta(\xi_{ji})^T \mathbf{F}_{ji} \right) \right) = 0 \quad (12)$$

The components of the vector $\boldsymbol{\tau}$ are the actuation forces acting on the slides of the linear modules along the $\hat{\mathbf{a}}_i$ direction; the vector \mathbf{f} represents the total force acting on the moving platform given by the sum of its weight $m_p \mathbf{g}$, its inertia force $\mathbf{I} m_p \ddot{\mathbf{p}}$ and an external force \mathbf{f}_e , if an interaction with the environment occurs, applied at its center of mass (the applied torques are completely born by robot's frame). The terms \mathbf{F}_{ji} are the wrenches of the j^{th} member, namely the resultants of the applied and inertia forces on the corresponding centers of mass, with $j = leg, ss, car$ respectively for the main part of the leg, the

swinging support and the carriage of each i^{th} kinematic chain. $\delta(\mathbf{a})$, $\delta(\mathbf{p})$ and $\delta(\xi_{ji})$ are the virtual displacements associated with the relative force vector as stated in (12): the first and the last vectors are connected to the second one by means of the Jacobian matrices provided by (4) and (15-17); equation (12) can be easily re-written as:

$$\delta(\mathbf{p})^T \left[\mathbf{J}_p^T \boldsymbol{\tau} + \mathbf{f} + \sum_{i=1}^3 \left(\sum_j \left(\mathbf{J}_{ji}^T \mathbf{F}_{ji} \right) \right) \right] = 0 \quad (13)$$

where the term inside the square brackets has to be null because equation (13) is valid for any virtual displacement of the moving platform. Finally the inverse dynamics model of the robot follows:

$$\boldsymbol{\tau} = -\mathbf{J}_p^{-T} \left(\mathbf{f} + \sum_{i=1}^3 \left(\sum_j \left(\mathbf{J}_{ji}^T \mathbf{F}_{ji} \right) \right) \right) \quad (14)$$

Equation (14) can be rewritten as:

$$\boldsymbol{\tau} = -\mathbf{J}_p^{-T} \left[\mathbf{f} + \sum_{i=1}^3 \left({}^{D_i} \mathbf{J}_{leg_i}^T {}^{D_i} \mathbf{F}_{leg_i} + {}^{D_i} \mathbf{J}_{ss_i}^T {}^{D_i} \mathbf{F}_{ss_i} + {}^{D_i} \mathbf{J}_{car_i}^T {}^{D_i} \mathbf{F}_{car_i} \right) \right] \quad (15)$$

A premultiplication of (15) by the transposed Jacobian matrix (4) provides the robot's inverse dynamics in the task space canonical form:

$$\boldsymbol{\tau}_x = \mathbf{J}_p^T \boldsymbol{\tau} = \mathbf{M}_x \ddot{\mathbf{p}} + \mathbf{C}_x + \mathbf{G}_x - \mathbf{f}_e \quad (16)$$

In the joint space, the following model holds:

$$\boldsymbol{\tau} = \mathbf{M} \ddot{\mathbf{a}} + \mathbf{C} + \mathbf{G} - \mathbf{J}_p^{-T} \mathbf{f}_e \quad (17)$$

4 DYNAMIC ANALYSIS

4.1 DIRECT DYNAMICS

Once obtained the analytical equations (17) of robot's inverse dynamics in a closed-form, the direct dynamics model can be derived by expressing the linear acceleration of the moving platform (or of the slides of the linear modules) as a function of the active forces' vector.

Such model has been implemented and integrated in Matlab and the outcoming results have been compared with those provided by the robot's multibody simulations performed in Virtual.Lab motion environment.

The mathematical model of the direct dynamics has been rearranged in order to include the inertia of the ball bearing guides and of the motors' rotors.

Several tests have demonstrated the correctness of the mathematical model because of the agreement in terms of position trajectories, velocity and acceleration profiles corresponding to the same input torque vector; in order to compare the dynamic equations of the mathematical and virtual models, the integration of the dynamic equations has been performed only by means of Matlab solvers,.

Figure 4 shows for instance a comparison between the multibody and the analytical models: the errors on carriages' displacement are represented for a given constant torque vector $\tau = [-0.60, -0.55, -0.45] \text{ Nm}$: the results are very close for the two sets of simulations.

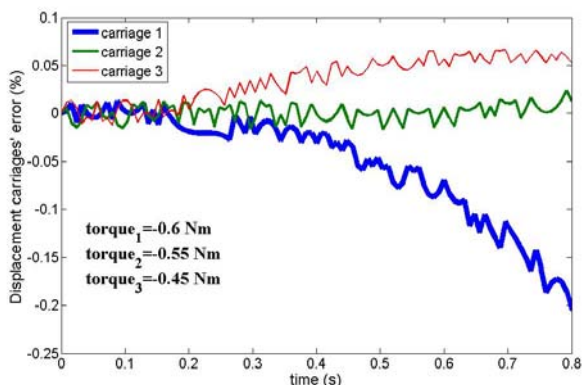


Figure 4 Comparison between the joint displacements obtained in Matlab and Virtual.Lab.

4.2 MASS MATRIX ANALYSIS

A common method to compare the relative influence of mass matrices' terms is to plot their values sweeping several horizontal plane of the robot's workspace: figure 5 plots the value of all the terms of the matrix for each position (x,y) of the moving platform on the plane $z = 0.5 \text{ m}$.

The six elements of M_x show a smooth behaviour, in fact they are almost constant in the plots of Fig. 5, where they are computed for end-effector's positions lying on given planes; moreover, the off-diagonal terms have an almost null value even if it tends to increase close to the boundaries.

Provided that the boundary surfaces of the workspace are not considered, the mass matrix can be eventually taken as a diagonal, almost constant matrix.

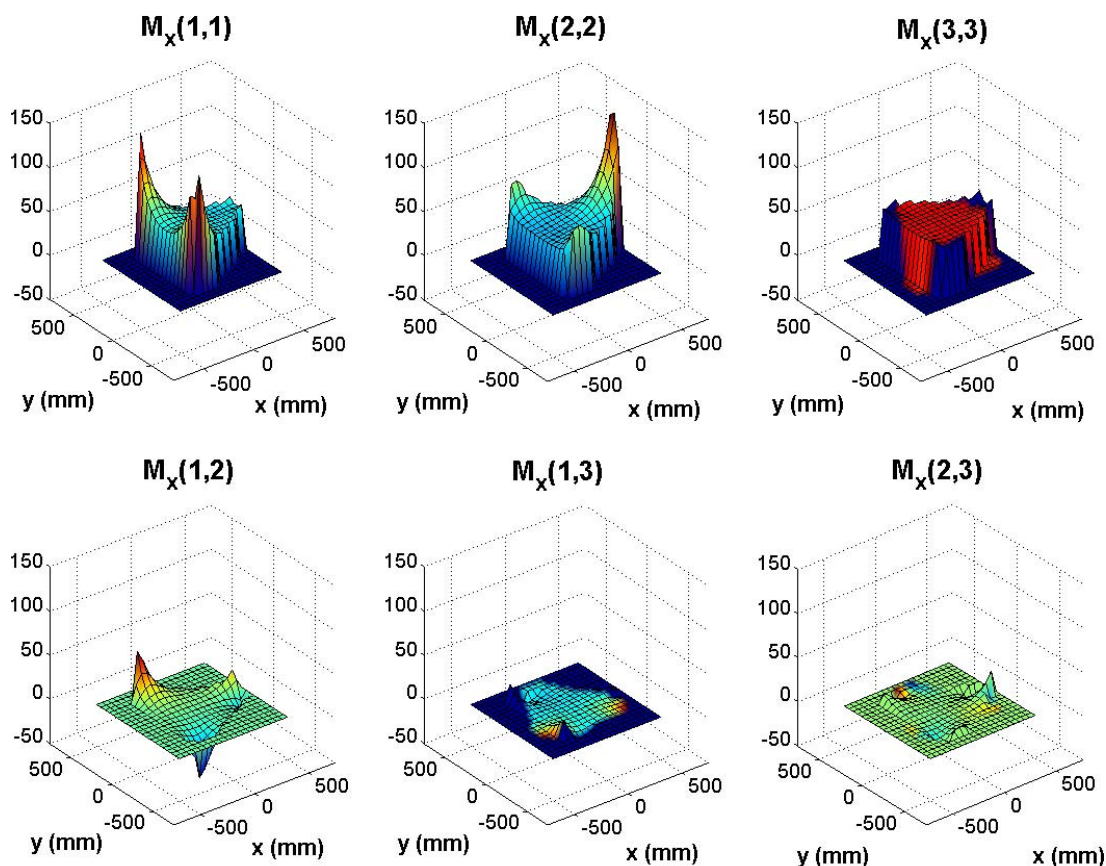


Figure 5 Values of the elements of the M_x matrix [$kg \cdot m^2$] when the end-effector lies on the horizontal plane $z=0.5 \text{ m}$.

4.3 CORIOLIS-CENTRIFUGAL VECTOR ANALYSIS

The Coriolis and Centrifugal vectors can heavily affect robot's dynamics, especially at high velocities. The possibility to reduce the complexity of the dynamic model

leads to an investigation of the weight of the terms of the dynamic equation with respect to the actual total torque provided by the motors.

Unfortunately many tests have shown that the physical parts of the I.Ca.Ro. robot, namely the legs and the moving

platform, have a comparable importance, in fact considering or less for example the Centrifugal and Coriolis terms, there is a considerable change of trajectory for a given torque vector in a common range of work values, as shown in figure 6.

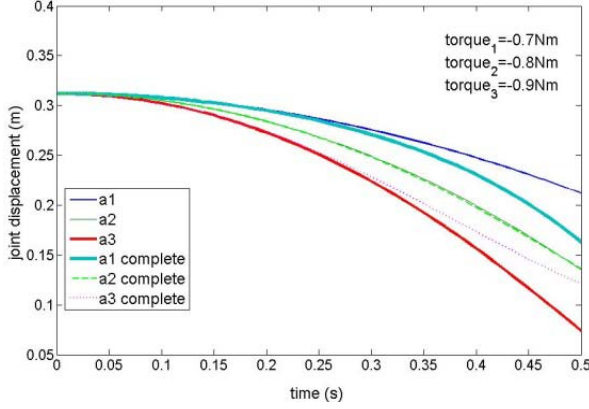


Figure 6 Comparison between the joint displacements obtained for the complete model and without Coriolis and Centrifugal terms

4.4 GRAVITY VECTOR

In order to appreciate how much the gravity vector affects the motors' torque, the weights of the mechanical parts of the robot are collected in table 1. It is noted that the weight of the legs is around 10 kg each one, while the moving platform only weighs about 1.5 kg; however, even if the platform is lighter than the legs, in certain positions of the space its torque contribution at the base has a meaningful value. In fact when the legs are completely stretched out, the required torques to statically compensate the gravitational effects are comparable with the torque necessary to hold the legs.

A way to evaluate the relative contribution of the terms summed up in equation (16), is given by the following procedure: once defined a linear trajectory inside the robot's workspace with a sinusoidal motion at frequency f between its extremes, the actuation torques of the motors are determined for frequencies more and more high according to the three following conditions: complete actual torque vector given by all the cited terms, torque vector without Coriolis and Centrifugal rate, torque vector given by only gravitational term, according to the following expressions:

$$\begin{aligned} \boldsymbol{\tau}_1 &= \mathbf{J}_p^{-T} \mathbf{M}_x \ddot{\mathbf{p}} + \mathbf{J}_p^{-T} \mathbf{C}_x + \mathbf{J}_p^{-T} \mathbf{G}_x \\ \boldsymbol{\tau}_2 &= \mathbf{J}_p^{-T} \mathbf{M}_x \ddot{\mathbf{p}} + \mathbf{J}_p^{-T} \mathbf{G}_x \\ \boldsymbol{\tau}_3 &= \mathbf{J}_p^{-T} \mathbf{G}_x \end{aligned} \quad (18)$$

The motion laws imposed to the moving platform have been imposed for different trajectories along the x , y and z directions, individually studied, given by the sinusoids of equations:

$$\begin{aligned} x &= X \cdot \sin(\Omega \cdot t) \\ y &= Y \cdot \sin(\Omega \cdot t) \\ z &= Z \cdot \sin(\Omega \cdot t) \end{aligned} \quad (19)$$

where $\Omega = 2\pi f$ and the amplitudes X, Y, Z have been chosen in a way that all the workspace could be swept (about 0.5-0.6 m)

When the frequency is 0.1 Hz, for example, the terms provided by the mass matrix can be neglected while the Coriolis and Centrifugal terms have a weight of 20% with respect to the total torque, see figure 7; increasing the frequency up to 0.2 and 0.3 Hz, the centrifugal and Coriolis terms become even more predominant with respect to the others (over 50% of the total torque). Such result can be justified by the fact that the derivatives of (19) provide for the velocity a linear dependency by Ω while for the acceleration by Ω^2 , and values of pulsation Ω less than 1 rad/s entails an increase faster for the velocity than for the acceleration. Frequencies higher than 0.3 Hz are not allowed because of the limit imposed by the maximum torque of the motors (6.6 Nm) and their maximum velocity (2300 rpm).

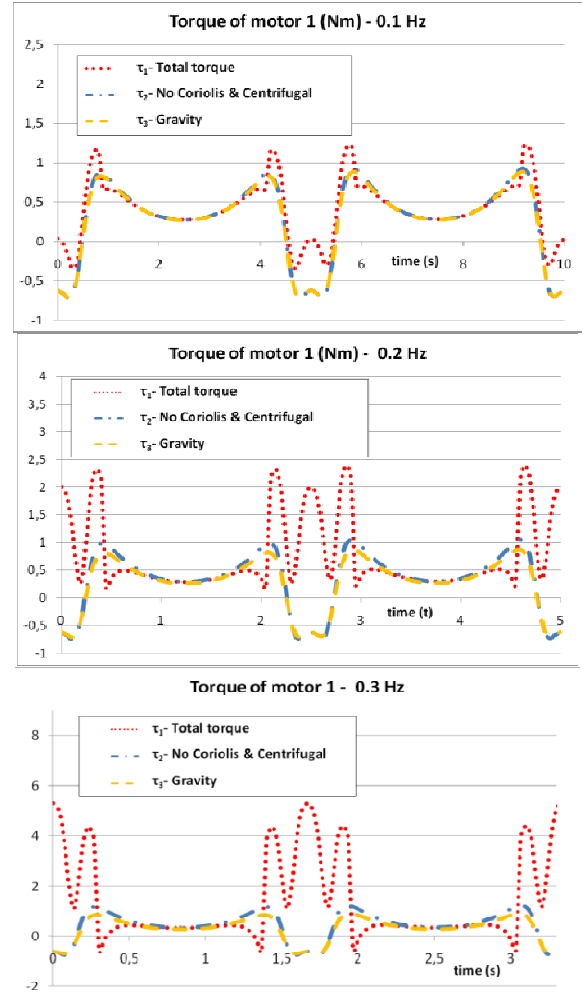


Figure 7 Torque of motor 1 for y displacements at 0.1, 0.2 and 0.3 Hz

5 CONCLUSIONS

The dynamic model of a Cartesian parallel manipulator for motion of pure translation has been worked out and several tests have been performed in order to characterise its behaviour, also by investigating the relative influence of the mass matrix, the Coriolis and Centrifugal vectors together with the gravity vector.

The simulations made on the analytical model have highlighted some important aspects: the Coriolis and Centrifugal terms that come out from the dynamic formulation have an important role in the dynamics of the robot, while the term related to the mass matrix and to the linear accelerations of the end-effector does not affect it significantly, even if the mass matrix can be taken as a diagonal, almost constant matrix. Besides the motors' torque required for the mechanical parts of the manipulator cannot be neglected too, in fact as mentioned in the paper the legs have a meaningful weight and the moving platform in several positions cannot be ignored.

Another important result is that at low frequencies the term of the dynamic equation that is mostly relevant for the actuation torques is the gravity vector, in such case all the other terms of the model can be neglected, while, increasing the frequency, the Coriolis and Centrifugal effects become predominant.

Some refinements of the model however have to be introduced, for example friction and compliances in the joints mostly affected by deflections, and some tests with external forces still have to be performed.

REFERENCES

- [1] Callegari M. and M.-C. Palpacelli. Prototype design of a translating parallel robot, *Meccanica*, Vol. 43(2), pp.133-151. 2008.
- [2] Do W. and D. Yang. Inverse dynamic analysis and simulation of a platform type of robot. *J Robotic Systems*, Vol. 5, pp.209-227. 1988.
- [3] Dasgupta B. and T. Mruthunjaya. A Newton–Euler formulation for the inverse dynamics of the Stewart platform manipulator. *Mechanisms & Machine Theory*, Vol. 34, pp.711-725. 1998.
- [4] Guo H. and H. Li. Dynamic analysis and simulation of a six degree of freedom Stewart platform manipulator. *Proc Inst Mech Eng Part C J Mech Eng Sci*, Vol. 220, pp.61-72. 2006.
- [5] Khalil W. and O. Ibrahim. General solution for the dynamic modelling of parallel robots. *J Intelligent Robotic Systems*, Vol. 49, pp.19-37. 2007.
- [6] Nguyen C. and F. Pooran. Dynamic analysis of a 6 DOF CKCM robot end-effector for dual-arm telerobot systems. *Robot Autonomous Systems*, Vol. 5, pp.377-394. 1989.
- [7] Caccavale F., B. Siciliano and L. Villani. The Tricept robot: dynamics and impedance control. *IEEE/ASME Trans. Mechatronics*, Vol. 8, pp.263-268. 2003.
- [8] Di Gregorio R. and V. Parenti-Castelli. Dynamics of a class of parallel wrists. *ASME J. Mechanical Design*, Vol. 126, pp.436-441. 2004.
- [9] Liu M.J., C.X. Li, C.N. Li. Dynamics analysis of the Gough–Stewart platform manipulator. *IEEE Trans. Robotics Automation*; Vol. 16(1):94-98. 2000.
- [10] Lopes, A.M. Dynamic modeling of a Stewart platform using the generalized momentum approach, *Commun Nonlinear Sci Numer Simulat*, Vol. 14, pp.3389-3401. 2009.
- [11] Miller K. Optimal design and modeling of spatial parallel manipulators. *Int J Robotics Research*, Vol. 23, pp.127-140. 2004.
- [12] Zhang C.D. and S.M. Song. An Efficient Method for Inverse Dynamics of Manipulators Based on the Virtual Work Principle. *J. Robotic Systems*, Vol. 10(5), pp. 605-627. 1993.
- [13] Gallardo J., J. Rico, A. Frisoli, D. Checcacci and M. Bergamasco. Dynamics of parallel manipulators by means of screw theory. *Mechanisms & Machine Theory*, Vol. 38, pp.1113-1131. 2003.
- [14] Muller A and P. Maiber. A Lie-group formulation of kinematics and dynamics of constrained MBS and its application to analytical mechanics. *Multibody Systems Dynamics*, Vol. 9(4), pp.311-352. 2003.
- [15] Angeles, J. and S. Lee. The Formulation of Dynamical Equations of Holonomic Mechanical Systems Using a Natural Orthogonal Complement, *ASME J. Applied Mechanics*, Vol. 55, pp.243-244. 1988.
- [16] Callegari M., A. Cammarata, A. Gabrielli, M. Ruggiu and R. Sinatra. Analysis and Design of a 3-CRU Spherical Micromechanism with Flexure Hinges. *ASME J. Mechanical Design*, Vol. 131. 2009.
- [17] Wang J. and C.M. Gosselin. A New Approach for the Dynamic Analysis of Parallel Manipulators. *Multibody Systems Dynamics*, Vol. 2, pp.317-334. 1998.
- [18] Tsai LW. Solving the Inverse Dynamics of a Stewart-Gough Manipulator by the Principle of Virtual Work. *ASME J. Mechanical Design*, Vol. 122(1), pp.3-9. 2000.
- [19] Callegari M., M.C. Palpacelli and M. Principi. Dynamics Modelling and Control of the 3-RCC Translational Platform”, *Mechatronics*, Vol. 16(10), pp. 589-605. 2006.
- [20] Zhao Y. and F. Gao. Inverse dynamics of the 6-dof out-parallel manipulator by means of the principle of virtual work, *Robotica*, Volume 27, Issue 02, pp 259-268. 2009.
- [21] Abdellatif H. and B. Heimann. Computational efficient inverse dynamics of 6-DOF fully parallel manipulators by using the Lagrangian formalism. *Mechanism and Machine Theory*, Vol. 44, pp.192-207. 2009.

LASER AND VISION BASED OBJECT DETECTION FOR MOBILE ROBOTS

L. Tamas

Gh. Lazea

M. Popa

I. Szoke

A. Majdik

Automation Department, Technical University of Cluj-Napoca, Romania

ABSTRACT

This paper presents a multi-sensor architecture to detect moving persons based on the information of the laser and vision systems. The detection of the objects are performed relative to the estimated robot position. In the laser space the Gaussian Mixture Model (GMM) classifier and for the vision the AdaBoost classifier is used, from which the outputs are combined with the Bayesian rule.

Keywords: Kalman filter, AdaBoost and GMM classifiers, Bayesian systems

1 INTRODUCTION

The perception capabilities of the mobile robots can be improved if multiple sensory information is fused in order to gain more relevant information as a result of the combination of several different sensors. This paper presents a multi-sensor architecture for processing the mobile robot's surrounding environment information for detecting moving obstacles in order to avoid collision in an indoor environment. Examples of such moving object may be people or other mobile robots [1].

In the proposed architecture two different object classifiers, based on different sensors, are combined in order to gain a higher level of inference and meaningful information to achieve robustness in the classification process. A cooperative strategy was adopted in order to establish the coordinate correspondence between the lidar and the monocular vision camera to reduce the field in which the object detection is performed. The robot position estimation was based on traditional dead-reckoning sensors and the Kalman filtering algorithm [2].

The architecture of the system is composed from three subsystems: the robot position estimator, the lidar based object observer, the vision based classifier and together with the coordinate transformation system the global classification subsystems.

Based on the relative position information of the robot, the people relative to the robot is detected by the vision based system in the field of view of the camera and the coordinates of the moving object are estimated [3]. These coordinates are transformed and used in the lidar based system to measure the distance of the object relative to the robot [4]. Finally, the trajectory of the robot is modified in order to avoid a possible collision with the object [5].

The position information from the *AdaBoost* classifier [6] based on *Haar-like* features is used to restrict the field of view (FOV) of the lidar in which the Gaussian Mixture Model classifier [7] will extract the depth information of the detected person combining and in the mean time the classifiers results are combined based on a Bayesian sum decision rule as this can be seen on the Figure 1

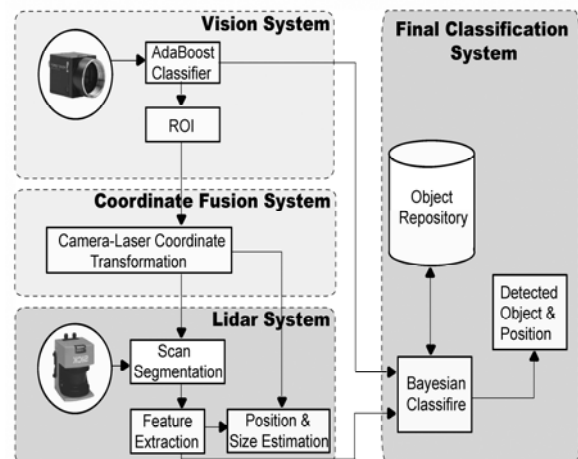


Figure 1 System architecture.

Contact author: L. Tamas¹

¹ Technical University of Cluj-Napoca, Romania
E-mail: levente.tamas@aut.utcluj.ro

2 RELATED WORK

The robot localization problem represents a key aspect in making a robot a real autonomous one. The position of the robot has to be estimated accurately based on the information from the sensors about the surrounding world [8].

The current trend in this field [9] is to fuse together relative and absolute measurements. The aim of this is to provide a better position estimation of the robot location based on the differing nature of the data from different kind of sensors. In order to fuse the information from different sources one of the widely applied methods is Kalman filtering [10]. This approach formulates the localization problem as a state-estimation one, will be used in this paper also.

Detecting different objects on a moving platform using Lidar and vision, or both sensors at the same time, for collision avoidance, mapping, or SLAM is well reported subject [11].

Several research works have been performed using laser-scanners in object classification and moving object tracking including application to localization and navigation, warning systems and others [3]. For the object classification the main directives in this domain are based either on heuristic methods, voting schemes, multi-hypotheses tracking [12] or even boosting approaches [13]. While the first two approaches lack the mathematical description framework and thus are not consistent, they still offer reasonable performance.

The vision based systems are commonly used for object detection and classification with or without lidar [14]. In certain light/ambient conditions the performance of the vision system may degraded, and the range information if it is available is not appropriate. In such cases the use of additional sensors in cooperation like the laser range finders is highly motivated.

Most of the object detection systems apply a simple segmentation as background subtraction or temporal differences between frames to detect objects. But these methods fail in the case when the camera is in motion.

Papageorgiu [15] introduced a trainable object detection architecture based on the wavelet templates that defines the shape of an object by considering a subset of the wavelet coefficients of the image. Based on this type of architecture the presented machine learning approach for object detection is able to process images at high speed and with high detecting rates. The image representation for learning is based on the AdaBoost algorithm. This method combines classifiers using Haar-like features and background separation algorithms which allow the background regions of the images to be discarded quickly focusing on the promising image parts [16].

The object detection with the monocular vision presented in this paper is based on the this type of object classifier.

3 ROBOT POSITION ESTIMATION

In this chapter it is presented the position estimation module for the moving platform based on the Kalman filter.

3.1 KALMAN FILTERS

A large number of mobile robots use position estimation based on the Kalman filters. Originally the theoretical backgrounds were formulated by Rudolf Kalman in 1960 and later there several extensions were developed for this algorithm successfully used in applications [8]. The Kalman filter can be shortly described as an optimal recursive data processing algorithm for systems corrupted by noise.

The Extended Kalman filter [17] assumes that the process model can be described by discrete-time state transition.

The filtering algorithm can be described in two steps: prediction and update.

The *prediction step* is done at time instant $k - 1$, before the information from the measurement is available and it is based on the previous state estimate \mathbf{x}_{k-1}^+ :

$$\mathbf{x}_k^- = \mathbf{F}\mathbf{x}_{k-1}^+ + \mathbf{B}\mathbf{u}_k \quad (1)$$

$$\mathbf{P}_k^- = \mathbf{F}\mathbf{P}_{k-1}^+ + \mathbf{Q} \quad (2)$$

The *update step* is performed after the measurement from the time step k is available, and includes this information as correction for the predicted state. This step can be summarized with the following equations:

$$\mathbf{x}_k^+ = \mathbf{x}_k^- + \mathbf{K}_k(\mathbf{z}_k - \mathbf{H}_k\mathbf{x}_k^-) \quad (3)$$

$$\mathbf{P}_k^+ = (\mathbf{I} - \mathbf{K}_k\mathbf{H}_k)\mathbf{P}_k^- \quad (4)$$

$$\mathbf{K}_k = \mathbf{P}_k^-\mathbf{H}_k^T(\mathbf{H}_k\mathbf{P}_k^-\mathbf{H}_k^T + \mathbf{R})^{-1} \quad (5)$$

The term with the bracket in (5) is called the innovation or residual and represents the difference between the prior estimated state and the measured one, the innovation sequence being an uncorrelated, white sequence [9].

3.2 DISCRETE TIME VEHICLE MODEL

The discrete time model adapted is the one which describes a steer-skid vehicle [18] and is given by the following state space equations:

$$\begin{aligned} x(k+1) &= x(k) + \delta TV(k) \cos(\varphi(k)) \\ y(k+1) &= y(k) + \delta TV(k) \sin(\varphi(k)) \\ \varphi(k+1) &= \varphi(k) + \nabla T \omega(k) \end{aligned} \quad (6)$$

with the $\mathbf{x}(k) = [x(k), y(k), \varphi(k)]^T$ state vector and $\mathbf{u}(k) = [V(k), \omega(k)]$ control vector with the ahead driving and steering command and ∇T is the sampling time. The nominal state transition can be described as $\mathbf{x}(k+1) = f(\mathbf{x}(k), \mathbf{u}(k))$.

Two kind of errors affect the vehicle driving forward command and steer angle, which makes the position estimation a difficult problem [19]. These errors can be

modeled as a combination of additive disturbance and multiplicative slip error.

The variances of the process noise were determined experimentally; in such a way that it reflects the true noise variance in the system. The details related to error propagation can be found in [9].

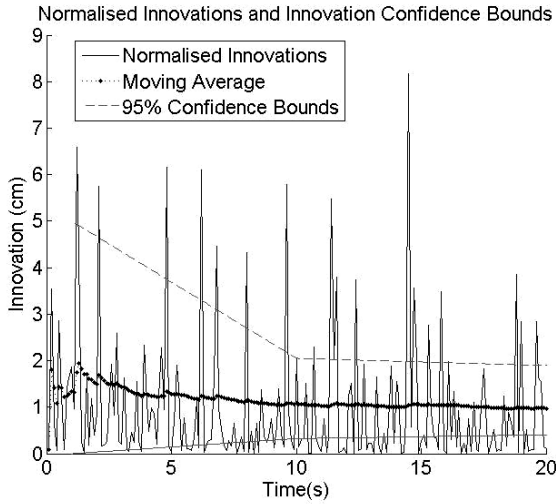


Figure 2 Innovation sequence of the position.

For the skid-steered vehicle the normalized innovation sequence at transverse displacement and the confidence bounds are shown in the Figure 2. As it can be seen on this figure, there is no sign of oscillator frequencies in the innovation and the normalized innovation falls in 90 % within the confidence bounds. These ensure that the filter was correctly tuned, and the estimate will be convergent.

4. LIDAR BASED CLASSIFICATION

In this section the lidar based system overview is presented with the segmentation, feature extraction and classification components.

4.1 SCAN SEGMENTATION

The scan segmentation belongs to the primary modules of the lidar architecture among with the data acquisition and pre-filtering modules. The segmentation is the process of splitting a scan into several coherent clusters, i.e. point clouds. The choice of segmentation method is rather arbitrary and will be dependent on other design choices as the alignment and covariance estimation strategies [20]. The current strategy is the one based on the assumption of distances between segments adopted from [13].

It is assumed that the laser range scan information is of the form $Z = \{b_1, \dots, b_L\}$ which is a set of beam. Each element of this set b_j is a pair of (θ_j, ρ_j) , where θ_j is the angle of the beam relative to the robot and ρ_j is the distance from the reflected surface.

The scan Z can be split into subsets according to the distance condition computed for the segment, which in case that the distance between two segments is greater than a

preset threshold, than a new segment is considered. Even if there are more sophisticated segmentation algorithms like the one presented by Premebida in [7], in the current problem setup we found appropriate this approach.

The output of the splitting procedure is an angle ordered sequence $P = \{S_1, \dots, S_M\}$ of segments in such a way that $\bigcup S_i = Z$. The elements of each segment S contain pairs of Cartesian coordinates $\mathbf{x} = (x, y)$ which can be converted to polar coordinates with $x = \rho \cos(\theta)$ and $y = \rho \sin(\theta)$.

4.2 FEATURE EXTRACTION

This module uses the segmented data in order to extract relevant information from the segmented data in order to ensure robustness in the algorithm. The extracted information is used later on in the classifier module and can be used also for visualization purposes too. The feature vector components may be chosen upon the required information [13]. The basic set of data which was used in the experiments contained the following entries:

- f1 object centroid;
- f2 normalized Cartesian dimensions given by:

$$f_2 = \sqrt{\Delta X^2 + \Delta Y^2}$$
- f3: the standard deviation of the point from the centroid:

$$f_3 = \sqrt{\frac{1}{n-1} \sum \|r_n - \bar{x}\|^2}$$

These components are essential to the classifier.

4.3 GMM OBJECT DESCRIPTION

A Gaussian mixture model (GMM) is a weighted combination of Gaussian probability density functions. These densities capture the particularities of an object.

In a GMM model the probability distribution of a x random variable is defined as a sum of M weighted Gaussian probability density functions:

$$p(x | \Theta) = \sum_{m=1}^M \alpha_m p(x | \theta_m) \quad (7)$$

where $\theta_1, \dots, \theta_M$ are the Gaussian distributions parameter and $\alpha_1, \dots, \alpha_M$ are the weighted vector such that

$$\sum_{m=1}^M \alpha_m = 1. \text{ A set of parameters for a mixture model is}$$

given by $\Theta = (\alpha; \theta_1, \dots, \theta_M)$ where each parameter $\theta_m = (\mu_m, \Sigma_m)$ represents the mean and the covariance of

the model. The likelihood for a feature vector Ω of each class is given by the linear combination of the Gaussian mixture probability density functions:

$$p(\Omega | q_i, \Theta^i) = \sum_{m=1}^M \alpha p(\Omega | \theta_m^i) \quad (8)$$

in which case each Gaussian density function for the two dimensional case is:

$$p(\Omega | q_i, \Theta^i) = \frac{1}{\sqrt{(2\pi)^2 |\Sigma_m^i|}} \exp\left[-\frac{1}{2}(\Omega - \mu_m^i)^T (\Sigma_m^i)^{-1} (\Omega - \mu_m^i)\right] \quad (9)$$

The Gaussian mixture parameters for each object of interest was determined using the expectation-maximization (EM) algorithm. In this way for each set of feature vectors ($\Omega^N = \Omega_1, \dots, \Omega_N$) the EM algorithm computes M Gaussian parameter vectors that maximizes the joint likelihood among the Gaussian density functions:

$$p(\Omega^N | q_i, \Theta^i) = \prod_{j=1}^M p(\Omega_j | q_i, \Theta_m^i) \quad (10)$$

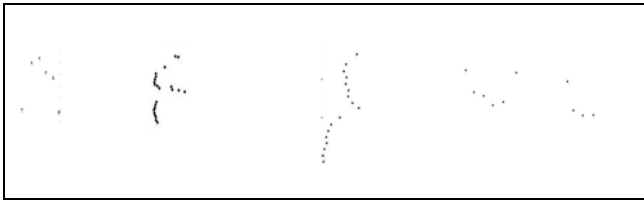


Figure 3 Possible leg forms.

4.4 BAYESIAN CLASSIFIER

After Gaussian mixture pdf is available for each object class, in order to classify which category (q_i) modeled by Θ^i fits the current observation feature-vector Ω_k a Bayesian decision framework based on the log-likelihood and on the log-prior probability is used.

Computing the log-likelihood has the advantage of computational effort by avoiding the computation of the exponentials in the pdf (8) and by turning the products into of (10) sums. Furthermore, as the log-likelihood is a monotonically growing function allows it to be used the former directly to classify the objects.

By considering the features equip probable, the logarithm of the posterior probability $\log(P(\Theta^i | \Omega))$ for all categories is proportional to the sum of the log-likelihood with the prior probability logarithm:

$$\log(P(\Theta^i | \Omega)) \approx \log(p(\Omega | \Theta^i)) + \log(P(\Theta^i)) \quad (11)$$

It is more convenient using Bayes' law to estimate the posterior probability as it uses only the likelihoods and the prior probability. The former is computed at each scan, which will become in the next scan the last estimated

posterior. In this way the prior probability is updated dynamically as:

$$P(\Theta_k^i) = P(\Theta^i | \Omega_{k-1}) \quad (12)$$

By knowing the initial prior probability for each class, the classification algorithm computes the maximum posterior probability for each segment. In order to decide which is the most likely class of object q_i for the segment S_j a decision rule of the following form was adopted:

$$\log(P(\Theta^i | \Omega_k)) = \max(\log(P(\Theta^u | \Omega_k))) \quad (13)$$

where u spans from 1 to the number of classes.

5 VISION BASED CLASSIFICATION

The vision-based system is used in this paper to estimate the positions of the people. In this scope, a people detection procedure is applied, which searches for people regions in image frames. A special attention is paid on the reduction of computing time with respect for a good detection rate, therefore the detection algorithm can work in a dynamic environment in real time. The detection procedure uses the gradient based segmentation algorithm for the reduction of the interest regions in images, and also the AdaBoost classification algorithm [21] for finding those regions which contain people.

5.1 GRADIENT BASED SEGMENTATION

The gradient segmentation used in this paper is based on clustering horizontal gradients [22]. The structures of people appearances in images denote that these gradients can be useful for the reduction of searching area for people detection. Applying the horizontal gradients on an image, vertical edges are highlighted while the horizontal ones are masked, so that vertical structures can be clustered. The regions of interest from the images are considered those regions which accommodate the vertical structures with respect to a ratio between the region's height and width.

5.2 ADABOOST CLASSIFIER

Viola and Jones have proposed a multilevel classification procedure [23], using Haar features, which reduces the processing time but which has the same accuracy as the classification procedures on one level. The purpose of using Haar-like features for classification, instead of image pixel values, is to reduce the variability inside the pixel's classes and to increase it outside of them, making the classification easier. Usually, Haar-like features codify domain dataset, which are difficult to extract from a finite input with other methods. The learning capacity increases with the use of an extended and general Haar-like feature dataset. Moreover, these features can be computed in constant time, regardless of their position or dimension, using the Integral Image concept, described in [23].

The classification procedure proposed by Viola and Jones is based on pattern recognition approach, recognizing a person through the detection of a constellation of his body

parts forms. Using Haar-like features and also a training image set, some less discriminating classifiers, named weak classifiers $h'(P)$ are computed. These classifiers maintain details of human body shape.

Moreover, this paper proposes, for a better detection rate, that each feature should be computed on multiple training image sets and then combine the optimal obtained thresholds, to form a probability distribution on the domain of the current feature:

$$\sum_{i=1}^{m-1} p_i(a_c) = 1 \quad (14)$$

where $p_i(a_c)$ is the probability of the computed feature value a_c for feature a , to be in the $[\mu_i, \mu_{i+1}]$ interval, and m is the number of the training image sets.

The strong classifier is then obtained like a linear combination of probabilities values for each feature from the n -th features set:

$$f(P) = \sum_{j=1}^n p_j(a_c) \quad (15)$$

6 COMBINED OBJECT CLASSIFIERS

The basic idea of the combined object classifiers is presented on architecture Figure 1. The information from the laser and camera is used as input to two different kinds of classifiers in order to enhance the robustness of the moving person detection. First of all the information is structured in segments and than it is introduced to the classifier, as it was aforementioned.

6.1 CALIBRATION

The lidar and camera calibration is important to perform in order to transform the point coordinates from the camera $\{C\}$ frame to the laser reference $\{L\}$. For avoiding overwhelming computations, the camera and the laser are aligned "ideally" in the same plane parallel to the robot displacement plane.

In order to get the transformation matrix between the two coordinate systems, a special measurement set was considered, and the geometric transformation matrix was obtained by least squares error minimization technique.

The camera intrinsic and extrinsic parameters were approximated based on the online camera calibration toolbox [24], and in this way it can be easily achieved the transformation between the image and the camera frame.

6.2 COORDINATE TRANSFORMATION

After the region of interest (ROI) is detected by the camera, this information is given to the lidar module, which will transform the coordinates from the camera frame to its own frame, and will search only in the ROI for possible targets. With the combination of the two sensors and by assuming that the vehicle moves at a flat surface the bottom limit of

the detected object can be easily found out, while the height it may be estimated from the size on the image.

6.3 CLASSIFIER COMBINATION

Based on the idea of [25] the practical sum rule was used for the information fusion from the classifiers. The decision rule is based on the Bayesian framework to decide the detection of people from the output of the two different classifiers.

This framework works for arbitrary number of classifier outputs. In the general case, the number of classifiers can be denoted by NC and the feature vector used by the i^{th} classifier denoted by Ω_i . Further on it is assumed that

each class q_i is represented by a class conditional pdf $p(\Omega_i | q_i)$ and its prior probability of detection $P(q_i)$.

Based on the pdf and the apriori probability the object classification rule can be stated for the object assignment q_i as:

$$P(q_j | \Omega_1, \dots, \Omega_{NC}) = \max(P(q_k | \Omega_1, \dots, \Omega_{NC})) \quad (16)$$

It is fair to assume that the feature vectors are conditionally independent, and that the posterior probability of each classifier do not change drastically from the prior probability, based on the theoretical investigations in [25] the Bayesian combination decision rule for the q_i object assignment can be summarized as:

$$(1 - NC)P(q_j) + \sum_{i=1}^{NC} P(q_j | \Omega_i) = \max_k [(1 - NC)P(q_k) + \sum_{i=1}^{NC} P(q_k | \Omega_i)] \quad (17)$$

This practical sum rule uses the prior probability of occurrence of each class q_i and the posterior probabilities given by the classifiers.

7 EXPERIMENTAL RESULTS

The experiment setup contained a P3 skid-steered mobile robot equipped with a LMS200 laser range finder and a camera connected to a PIV laptop.

Before performing the main experiments in the indoor some preliminary test were done. The position estimation of the robot was observed to be more reliable at low turning speed as the accelerations were not explicitly introduced in the process model. The camera was also tested in different light/background conditions and the best hit rate was achieved with the images containing high contrast parts especially about the people (like striped colorful clothes).

The people detection was performed using data sequences in different positions and lighting conditions. The detection was done by applying the gradient segmentation to reduce the interest area from images and then labeling regions

from this area, which contain people, with a strong classifier obtained from AdaBoost algorithm.

The strong classifier is trained on a 6000 images set, 3000 of them as positive examples (containing people), with the resolution of 30x30 pixels.

A typical measurement output from the camera is shown on the . The high contrast background enables the detection of the full body in the test case.



Figure 4 The selected region classified as people.

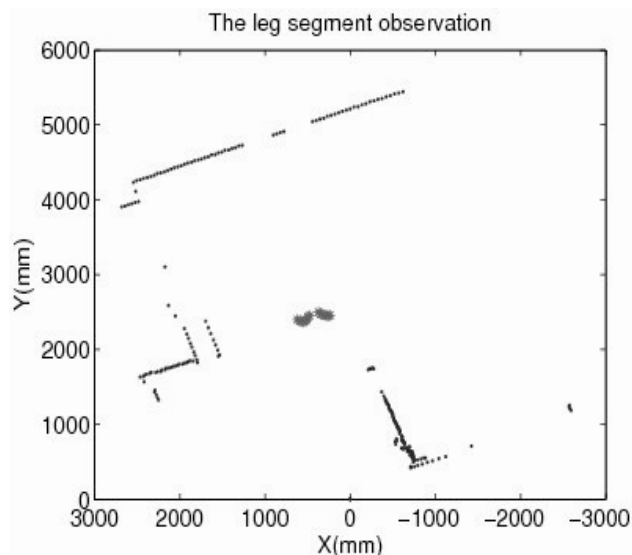


Figure 5 The selected segment classified as people leg.

The same observation from the laser scanner is shown on the Figure 5. Although there are similar regions on the laser scan to human legs which may give false alarms, the narrowed ROI by the camera enables to classify the correct segment as a human leg

In the most of the cases the vision based classifier achieved better results than the GMM classifier in terms of the hit rate, but this situation changes drastically in case of reduced camera visibility cases.

8 CONCLUSIONS

A multi-sensor object classifier was presented in this paper together with path planning technique for a mobile robot system. A cooperative technique was adopted to combine the information from the lidar and the visual systems. Details regarding the classification algorithms were presented for the both approaches. The computed coordinates of the moving human objects were used together with the position estimation for the path planning. In the further it is intended to test and validate against other classification algorithms the presented ones, and to extend the object detection to object tracking. As an alternative information source, the stereo-vision camera system is proposed to be introduced.

REFERENCES

- [1] Multi-target detection and tracking with laser range finder. Mendes, A, Bento, L C and Nunes, U. 2004. IEEE Intelligent Vehicles Symposium.
- [2] UMB mark: A Benchmark Test for Measuring odometry Errors in Mobile Robots. Borenstien, J. and Feng, L. 2001, SPIE, pp. 213-218.
- [3] Fusing range and intensity images for mobile robot localization. Neira, J, et al. 1999. IEEE Trans. Robotics and Automation. p. 761-784.
- [4] Moving target classification and tracking from real-time video. Lipton, A. J, Fugiyoshi, H and Patil, R. S. 1998. IEEE Image Understanding. p. 129-136.
- [5] Fast obstacle detection for urban traffic situations. Franke, U and Heinrich, S. 2002. IEEE Trans. Intell. Transport. Syst. p. 173-181.
- [6] Vision-based pedestrian detection using Haar-like features. Monteiro, G, Peixoto, P and Nunes, U. 2006. Proc. 6th National Festival of Robotics.
- [7] A multi-target tracking and GMM-classifier for intelligent vehicles. Premebida, C and Nunes, U. 2006. 9th International IEEE Conference on Intelligent Transportation Systems.
- [8] Mobile robot positioning sensors and techniques. Borenstein, J., et al. 1997, J. Robot. Syst, Vol. 14, pp. 231-249.
- [9] Durrant-Whyte, H. Multi Sensor Data Fusion. s.l.: Australian Center for Field Robotics, 2006.
- [10] Bar-Shalom, Y. and Li, X. Estimation and Tracking-Principles, Techniques and Software. s.l.: Artech House, 1993.
- [11] Simultaneous localization and map building using natural features in outdoor environments. Guivant, J, Nebot, E and Durrant-Whyte, H. F. 2000. Intelligent Autonomous Systems VI. p. 581-588.
- [12] Object tracking and classification using a multiple hypothesis approach. Streller, D and Dietmayer, K. 2004. IEEE Intelligent Vehicles Symposium.
- [13] Using boosted features for detection of people in 2D range scans. Mozos, O, Arras, K and Burgard, W. 2007.

- [14] Pedestrian localization and tracking system with Kalman filtering. Bertozzi, M and Broggi, A. 2004. IEEE Intelligent Vehicles Symposium 2004.
- [15] Pedestrian detection using wavelet templates. Oren, M, Papageorgiou, C and Sinha, P. 1997. Proc. IEEE CVPR 1997.
- [16] Rapid object detection using a boosted cascade of simple features. Viola, P. and Jones, M. 2001. IEEE Computer Society Conference on Computer Vision and Pattern Recognition (CVPR). pp. 511-518.
- [17] Maybeck, P.S. Stochastic Models, Estimation and Control. s.l. : Academic Press, 1979. Vol. 1.
- [18] A dead-reckoning scheme for skid-steered vehicles in outdoor environments. Kyriakopoulos, K.J. and Anousaki, G.C. 2004, Proc. Int. Conf. Automation, pp. 580-585.
- [19] Economou, J.T. Modelling and Control of Skid Steer Vehicles. s.l. : Ph.D. thesis, Royal Military College of Science, Cranfield University, 1999.
- [20] Line extraction in 2D range images for mobile robotics. Borges, G. A and Aldon, M. J. 2004, Journal of Intelligent \& Robotic Systems, Vol. 40, pp. 267-297.
- [21] Experiments with a new boosting algorithm. Freund, Y. and Schapire, R. 1996. Proceedings of the International Conference on Machine Learning(ICML). pp. 148-156.
- [22] Jaap, Wiegersma Aalzen. Real-time pedestrian detection in FIR and grayscale images. s.l. : Ruhr University, Bochum, 2006, pp. 39-45.
- [23] Robust real time face detection. Viola, P. and Jones, M. 2004. International Journal of Computer Vision. pp. 137-154.
- [24] www.vision.caltech.edu/bouguetj/. Toolbox, Camera Calibration. 2005.
- [25] On combining classifiers. Kittler, J, et al. 1998. Vol. 20, p. 226-239.

TEMPLATE FOR PREPARING PAPERS FOR PUBLISHING IN INTERNATIONAL JOURNAL OF MECHANICS AND CONTROL

Author1* Author2**

* affiliation Author1

** affiliation Author2

ABSTRACT

This is a brief guide to prepare papers in a better style for publishing in International Journal of Mechanics and Control (JoMaC). It gives details of the preferred style in a template format to ease paper presentation. The abstract must be able to indicate the principal authors' contribution to the argument containing the chosen method and the obtained results. (max 200 words)

Keywords: keywords list (max 5 words)

1 TITLE OF SECTION (E.G. INTRODUCTION)

This sample article is to show you how to prepare papers in a standard style for publishing in International Journal of Mechanics and Control.

It offers you a template for paper layout, and describes points you should notice before you submit your papers.

2 PREPARATION OF PAPERS

2.1 SUBMISSION OF PAPERS

The papers should be submitted in the form of an electronic document, either in Microsoft Word format (Word'97 version or earlier).

In addition to the electronic version a hardcopy of the complete paper including diagrams with annotations must be supplied. The final format of the papers will be A4 page size with a two column layout. The text will be Times New Roman font size 10.

2.2 DETAILS OF PAPER LAYOUT

2.2.1 Style of Writing

The language is English and with UK/European spelling. The papers should be written in the third person. Related work conducted elsewhere may be criticised but not the individuals conducting the work. The paper should be comprehensible both to specialists in the appropriate field and to those with a general understanding of the subject.

Company names or advertising, direct or indirect, is not permitted and product names will only be included at the discretion of the editor. Abbreviations should be spelt out in full the first time they appear and their abbreviated form included in brackets immediately after. Words used in a special context should appear in inverted single quotation mark the first time they appear. Papers are accepted also on the basis that they may be edited for style and language.

2.2.2 Paper length

Paper length is free, but should normally not exceed 10000 words and twenty illustrations.

2.2.3 Diagrams and figures

Figures and Tables will either be entered in one column or two columns and should be 80 mm or 160 mm wide respectively. A minimum line width of 1 point is required at actual size. Captions and annotations should be in 10 point with the first letter only capitalised *at actual size* (see Figure 1 and Table VII).

Contact author: author1¹, author2²

¹Address of author1.

²Address of author2 if different from author1's address.

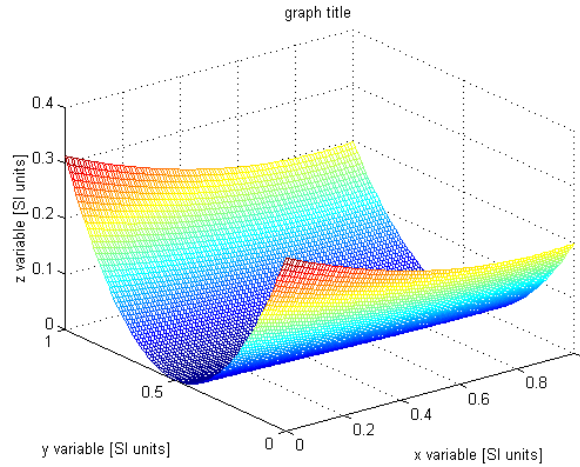


Figure 1 Simple chart.

Table VII - Experimental values

Robot Arm Velocity (rad/s)	Motor Torque (Nm)
0.123	10.123
1.456	20.234
2.789	30.345
3.012	40.456

2.2.4 Photographs and illustrations

Authors could wish to publish in full colour photographs and illustrations. Photographs and illustrations should be included in the electronic document and a copy of their original sent. Illustrations in full colour ...

2.2.5 Equations

Each equation should occur on a new line with uniform spacing from adjacent text as indicated in this template. The equations, where they are referred to in the text, should be numbered sequentially and their identifier enclosed in parenthesis, right justified. The symbols, where referred to in the text, should be italicised.

- point 1
 - point 2
 - point 3
- 1. numbered point 1
- 2. numbered point 2
- 3. numbered point 3

$$W(d) = G(A_0, \sigma, d) = \frac{1}{T} \int_0^{+\infty} A_0 \cdot e^{-\frac{d^2}{2\sigma^2}} dt \quad (1)$$

3 COPYRIGHT

Authors will be asked to sign a copyright transfer form prior to JoMaC publishing of their paper. Reproduction of any part of the publication is not allowed elsewhere without permission from JoMaC whose prior publication must be cited. The understanding is that they have been neither previously published nor submitted concurrently to any other publisher.

4 PEER REVIEW

Papers for publication in JoMaC will first undergo review by anonymous, impartial specialists in the appropriate field. Based on the comments of the referees the Editor will decide on acceptance, revision or rejection. The authors will be provided with copies of the reviewers' remarks to aid in revision and improvement where appropriate.

5 REFERENCES (DESCRIPTION)

The papers in the reference list must be cited in the text. In the text the citation should appear in square brackets [], as in, for example, "the red fox has been shown to jump the black cat [3] but not when...". In the Reference list the font should be Times New Roman with 10 point size. Author's first names should be terminated by a 'full stop'. The reference number should be enclosed in brackets.

The book titles should be in *italics*, followed by a 'full stop'. Proceedings or journal titles should be in *italics*. For instance:

REFERENCES (EXAMPLE)

- [1] Smith J., Jones A.B. and Brown J., *The title of the book*. 1st edition, Publisher, 2001.
- [2] Smith J., Jones A.B. and Brown J., The title of the paper. *Proc. of Conference Name*, where it took place, Vol. 1, paper number, pp. 1-11, 2001.
- [3] Smith J., Jones A.B. and Brown J., The title of the paper. *Journal Name*, Vol. 1, No. 1, pp. 1-11, 2001.
- [4] Smith J., Jones A.B. and Brown J., *Patent title*, U.S. Patent number, 2001.

International Journal of Mechanics and Control – JoMaC
Published by Levrotto&Bella
TRANSFER OF COPYRIGHT AGREEMENT

<p>NOTE: Authors/copyright holders are asked to complete this form signing section A, B or C and mail it to the editor office with the manuscript or as soon afterwards as possible.</p>	<p><i>Editor's office address:</i> Andrea Manuello Bertetto Elvio Bonisoli <i>Dept. of Mechanics</i> <i>Technical University – Politecnico di Torino</i> <i>C.so Duca degli Abruzzi, 24 – 10129 Torino – Italy</i> <i>e_mail: jomac@polito.it</i> <i>fax n.: +39.011.564.6999</i></p>
--	---

The article title:

By: _____

To be Published in *International Journal of Mechanics and Control JoMaC*
Official legal Turin court registration Number 5320 (5 May 2000) - reg. Tribunale di Torino N. 5390 del 5 maggio 2000

- A Copyright to the above article is hereby transferred to the JoMaC, effective upon acceptance for publication. However the following rights are reserved by the author(s)/copyright holder(s):
1. All proprietary rights other than copyright, such as patent rights;
 2. The right to use, free or charge, all or part of this article in future works of their own, such as books and lectures;
 3. The right to reproduce the article for their own purposes provided the copies are not offered for sale.
- To be signed below by all authors or, if signed by only one author on behalf of all co-authors, the statement A2 below must be signed.*

A1. All authors:

SIGNATURE _____ DATE _____ SIGNATURE _____ DATE _____

PRINTED NAME _____ PRINTED NAME _____

SIGNATURE _____ DATE _____ SIGNATURE _____ DATE _____

PRINTED NAME _____ PRINTED NAME _____

A2. One author on behalf of all co-authors:

"I represent and warrant that I am authorised to execute this transfer of copyright on behalf of all the authors of the article referred to above"

PRINTED NAME _____

SIGNATURE _____ TITLE _____ DATE _____

B. The above article was written as part of duties as an employee or otherwise as a work made for hire. As an authorised representative of the employer or other proprietor. I hereby transfer copyright to the above article to *International Journal of Mechanics and Control* effective upon publication. However, the following rights are reserved:

1. All proprietary rights other than copyright, such as patent rights;
2. The right to use, free or charge, all or part of this article in future works of their own, such as books and lectures;
3. The right to reproduce the article for their own purposes provided the copies are not offered for sale.

PRINTED NAME _____

SIGNATURE _____ TITLE _____ DATE _____

C. I certify that the above article has been written in the course of employment by the United States Government so that no copyright exists, or by the United Kingdom Government (Crown Copyright), thus there is no transfer of copyright.

PRINTED NAME _____

SIGNATURE _____ TITLE _____ DATE _____

CONTENTS

- 3 Comparative Analysis of Isotropy Indices in RR and RRp Arms**
N.P. Belfiore, M. Verotti, L. Consorti
- 13 The Open-Control Concept for Holonic Manufacturing**
S. Raileanu, T. Berger, Y. Sallez, T. Borangiu, D. Trentesaux
- 21 A 3D-Laser Scanner for Autonomous Mobile Robots**
G. Reina, N.I. Giannoccaro, A. Messina, A. Gentile
- 29 MR Compatible Device for Active and Passive Foot Movements**
G. Belforte, G. Eula, G. Quaglia, S. Appendino, F. Cauda, K. Sacco
- 39 Calibration of Robot-Mounted Laser Scanning Probe Based on a Tool Transformation**
T. Borangiu, A. Dogar, A. Dumitrache
- 45 A Lunar Rover Leg: Optimal Design of a Decoupling Joint**
R. Ambu, C. Falchi, A. Manuello Bertetto
- 51 Design and Operation Issues for Parallel Robotic Devices in the Rehabilitation of Stroke Patients**
M. Ceccarelli, D. Pîslă, F. Graur, E. Ottaviano, C. Vaida, R. Ungur, S. Grande, M. Pop
- 59 Experimental Mobile Robotic Platform**
P. Čepón, R. Kamnik, J. Kuželički, T. Bajd, M. Munič
- 67 High Resolution Plane Angular Measurement System: Realisation and Error Evaluation**
A. Manuello Bertetto, R. Ricciu
- 73 Position Control of XY Piezo Actuated Stage with Neural Network Using Structural Genetic Algorithm**
J. Čas, D. Kusić
- 81 Dynamic Analysis of the I.Ca.Ro. Parallel Manipulator**
M. Callegari, L. Carbonari, M.C. Palpacelli
- 89 Laser and Vision Based Object Detection for Mobile Robots**
L. Tamas, G. Lazea, M. Popa, I. Szoke, A. Majdik